Winter 2006

Development and applications of inkjet printed conducting polymer micro-rings

Rajneek K. Khillan
Louisiana Tech University

DEVELOPMENT AND APPLICATIONS OF INKJET PRINTED CONDUCTING POLYMER MICRO-RINGS

By

Rajneek K. Khillan, B. E.

A Dissertation Presented in Partial Fulfillment of the
Requirement for the Degree of
Doctor of Philosophy in Engineering

COLLEGE OF ENGINEERING AND SCIENCE
LOUISIANA TECH UNIVERSITY

February 2006

LOUISIANA TECH UNIVERSITY

THE GRADUATE SCHOOL

Nov. 17th 2005
Date

We hereby recommend that the dissertation prepared under our supervision by RAJNEEK KUMAR KHILLAN entitled DEVELOPMENT AND APPLICATIONS OF INKJET PRINTED CONDUCTING POLYMER MICRO-RINGS be accepted in partial fulfillment of the requirements for the Degree of PhD IN ENGINEERING

Yi Su
Supervisor of Dissertation Research

Ray Hedin
Head of Department

Electrical Engineering
Department

Recommendation concurred in:

Yufei Luo

Advisory Committee

Approved:
Director of Graduate Studies

Approved:
Dean of the Graduate School

Dean of the College

GS Form 13
(5/03)

APPROVAL FOR SCHOLARLY DISSEMINATION

The author grants to the Prescott Memorial Library of Louisiana Tech University the right to reproduce, by appropriate methods, upon request, any or all portions of this Dissertation. It is understood that "proper request" consists of the agreement, on the part of the requesting party, that said reproduction is for his personal use and that subsequent reproduction will not occur without written approval of the author of this Dissertation. Further, any portions of the Dissertation used in books, papers, and other works must be appropriately referenced to this Dissertation.

Finally, the author of this Dissertation reserves the right to publish freely, in the literature, at any time, any or all portions of this Dissertation.

Author Rajneek K Khillan

Date 11/28/2005

GS Form 14
(5/03)

ABSTRACT

A drying sessile drop moves the solute particles to the periphery where they get deposited in the form of a ring. This phenomenon is prevalent even with micro drops falling at high velocity from a piezo-actuator based inkjet printer. In polymer microelectronic field, this phenomenon is a major challenge for fabricating devices using inkjet printing. We exploited this problem and applied it for various novel applications in the field of polymer microelectronics.

Various dispensing techniques and temperature variations for micro-drop printing were used for modifying the micro-drops in such a way that the periphery of the micro-ring holds most of the solute as compared to inner base layer. Reactive ion etching (RIE) was used for removing the inner base layer in order to make the micro-rings completely hollow from the center. These micro-rings were applied in the fabrication of polymer light emitting diode, humidity sensor and vertical channel field effect transistor.

High resolution polymer light emitting diode array (> 200 pixels/inch) was fabricated by inkjet printing of micro-ring and each micro-ring acts as a single pixel. These micro-rings were applied as a platform for layer-by-layer (LbL) nano-assembly of poly-3,4-ethylenedioxythiophene:poly-styrenesulfonate (PEDOT:PSS) for the fabrication of humidity sensor. Enhanced sensitivity of the humidity sensor was obtained when the inkjet printed micro-rings are combined with LbL assembled PEDOT:PSS films. During the fabrication of vertical channel field effect transistors, inkjet printed PEDOT:PSS

micro-rings were used as source and the inner spacers between the adjacent micro-rings were used to make channel.

These micro-rings can also find other applications in the field of biological sciences. These micro-rings can be used as cell culture plates and as scaffolds for cell and/or tissue growth.

TABLE OF CONTENTS

LIST OF TABLES

LIST OF FIGURES

ACKNOWLEDGEMENTS

I would like to express my sincere thanks to Dr. Kody Varahramyan for providing me the opportunity to work under his able guidance. Dr. Varahramyan has been a constant source of inspiration to me throughout my four years of study at Louisiana Tech University. I would like to thank my advisor, Dr. Yi Su, for his technical advice and moral support which was indispensable for the successful completion of this dissertation. I want to thank Dr. Yuri Lvov for giving me a chance to work with his research group where I gained insight of the beauty of nanotechnology. Dr. Lvov is one of the pioneers of Layer-by-layer nano self-assembly technique. I consider myself to be very fortunate to have worked under the supervision of these professors. I would also like to thank Dr. Alfred Gunasekaran and Dr. Chester Wilson for their valuable comments and suggestions which helped improving the quality of this dissertation.

I would like to thank the staff members, Dee Tatum, Dr. Karen Xue, Jeanette Futrell, Sandy Wilson, Marry Bennett, John McDonald, Scott Williams and Deborah Wood for their supportive and friendly nature.

I would like to thank my research group members, Rohit Dikshit, Razat Nohria, Dr. Fengliang Xue, Dr. Zhengchun Liu, J. Liu, Neha Goel and Ganga for their useful discussions and opinions during my research work.

I want to thank Dr. Mangilal Agarwal, Rajendra Aithal, Dr. Rohit Ghan, Ravi Dasaka, Dr. Tatsiana Shutava, Shirish and Mr. Abdul Khaliq for the valuable technical

discussions at various stages of my research. I would also like to thank my friends Priyank Sukul, Tribal Narki, Krithi Shetty, Raju Gottumukkala, Deepti Terala and Sreelakshmi Yenamandra for their support and encouragement during my studies at Louisiana Tech Univeristy.

I would like to thank some special people who have made major contribution in development of my career, Vishal Bhasin, Venus Bhasin, Gurjeet Singh Dhothar, Mukesh Sharma, Jitender Bhandal, Atul Sharma, D. Amarnath and Kourie Henry.

I would like to thank my father Mr. Nirmal Kumar Khillan and my mother Mrs. Santosh Nagrath for their blessings, endless love, moral support and encouragement throughout my life.

Finally, I would thank God for giving me courage, patience and determination to face the obstacles in life.

CHAPTER 1

INTRODUCTION AND DISSERTATION OVERVIEW

1.1 Introduction

Conventional insulating polymers are widely used as substitutes for traditional materials like wood and metal, due to their high strength, light weight, ease of chemical modification, and processability at low temperature. Since 1950s, the study of semiconducting organic materials focused on small organic molecules in crystalline state. Molecular crystals like naphthalene and anthracene were found to display the semiconducting properties [1]. But they were considered not very efficient due to their poor semiconducting characteristics.

Semiconducting polymers have been synthesized by building the chromophores into the polymer as side groups or in the main chain [2]. In 1977, the first highly conducting chemically doped organic polymer polyacetylene was reported. These doped polymers were firstly brittle, unstable in air and difficult to process. But now these materials are stable and easily processable. The electric conductivities now range from 10^{-10} to more than 10^{4} S/cm. This covers the whole range of materials from insulators to semiconductors such as silicon to conductors such as copper [3]. At the end of 1980s undoped organic semiconductors, both polymers and small molecules revived an interest as a result demonstration of high-performance electroluminescent devices made of

multilayers of vacuum deposited dye films at Kodak [4], the report of field effect transistors made from polythiophene [5,6] and the discovery of electroluminescence from conjugated polymer based diodes at Cambridge University [7]. Conjugated polymers have an intrinsic advantage over small organic molecules due to their better mechanical properties, easy fabrication techniques, flexibility and cost effectiveness. Many companies such as Philips, CDT, Uniax, Seiko, Samsung, Motorola, and Epson are exploring for the applications of these conjugated polymers.

The ability of organic materials to transport holes and electrons due to the π-orbital overlap of neighboring molecules provides their semiconducting and conducting properties. The self-assembling or ordering of these organic and hybrid materials enhances the π-orbital overlap and is the key for improvements in carrier mobility. The recombination of the charge carriers under applied field can lead to the formation of an exciton. This exciton when falls from the excited state to the ground state emits light. Besides the electronic and optical properties, these materials possess good mechanical properties such as, flexibility, toughness and can be processed at lower temperatures. Various techniques used for the deposition of these polymers are vacuum evaporation, spin coating, stamping and inkjet printing [8].

Among all these polymer deposition techniques inkjet printing is potentially a low-cost and high throughput approach [9]. Advances in high resolution inkjet printing potentially allows the extension of this direct-write approach to the fabrication of medium to low resolution conductor lines for use in polymer light emitting diodes, polymer transistors, polymer solar cells, microelectronic packaging and electronic circuits such as, printed circuit boards. Present inkjet printers are capable of producing less than 20 μm lines which is much better than that obtained by screen printing method (~ 100 μm) [10].

Narrower conducting lines enable higher density and more compact circuits. Photolithography, which allows much finer resolution than that of inkjet printing has a disadvantage of high cost. Narrower conducting lines enable higher density and more compact circuits. Photolithography, which allows much finer resolution than that of inkjet printing has a disadvantage of high cost.

Inkjet printing requires solutions with low viscosity [11]. A drying droplet usually deposits its solute as a ring stain. This stain marks the perimeter of the droplet before drying. This phenomenon is known as the "coffee drop effect" is attributed to enhanced evaporation rate at the droplet edge and contact line pinning due to surface irregularities and solute deposition [12-14]. The rate of evaporation at the outer edge is more than the inner part. In order to compensate the evaporation loses the solute from the inner part moves outward to the edges. Thus the ring tends to become thicker at the edges than at the center. This ring formation is considered to be a serious problem in the advancement of inkjet printing technique for the microfabrication of electronic devices. Figure 1.1 shows recent advancements in eliminating the ring and making the drop smoother. Varying concentration of solvent are used to improve the homogeneity of the deposits [15].

In the course of experimentation with inkjet printing, we also encountered the same so-called coffee drop effect problem. Besides eliminating this problem for the fabrication of uniform thin films, we also exploited this effect in such a way so that the rings are hollow from the center and thicker at the periphery. The substrate temperature, surface properties and drop dispensing techniques were also modified in order to get perfect ring shapes for varying height and diameter of the rings. Oxygen plasma reactive ion etching (RIE) parameters were optimized to etch inner base layers of the micro-rings.

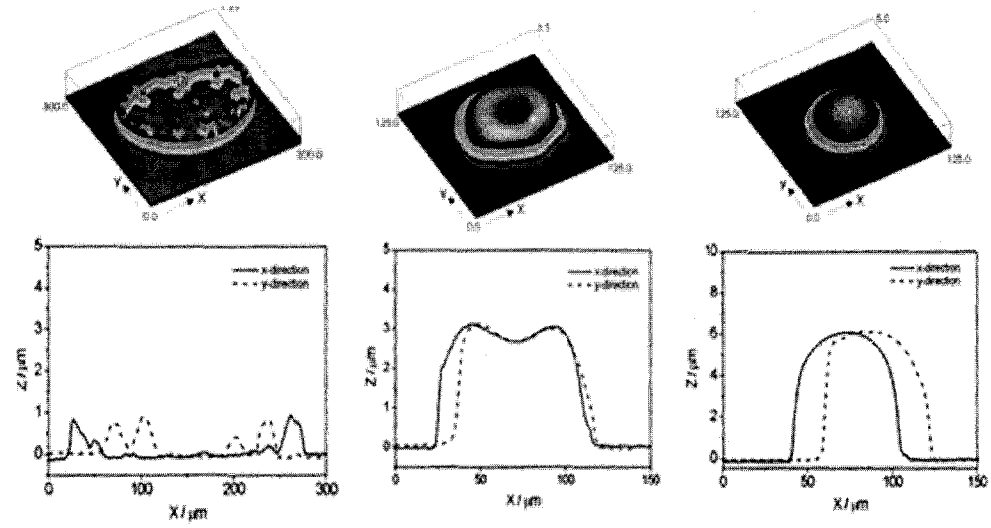

Figure 1.1 Varying the concentration of solvent to eliminate coffee drop effect [15]

Figure 1.2 shows the image of hollow micro-rings of varying diameter, fabricated by inkjet printing and oxygen plasma etching.

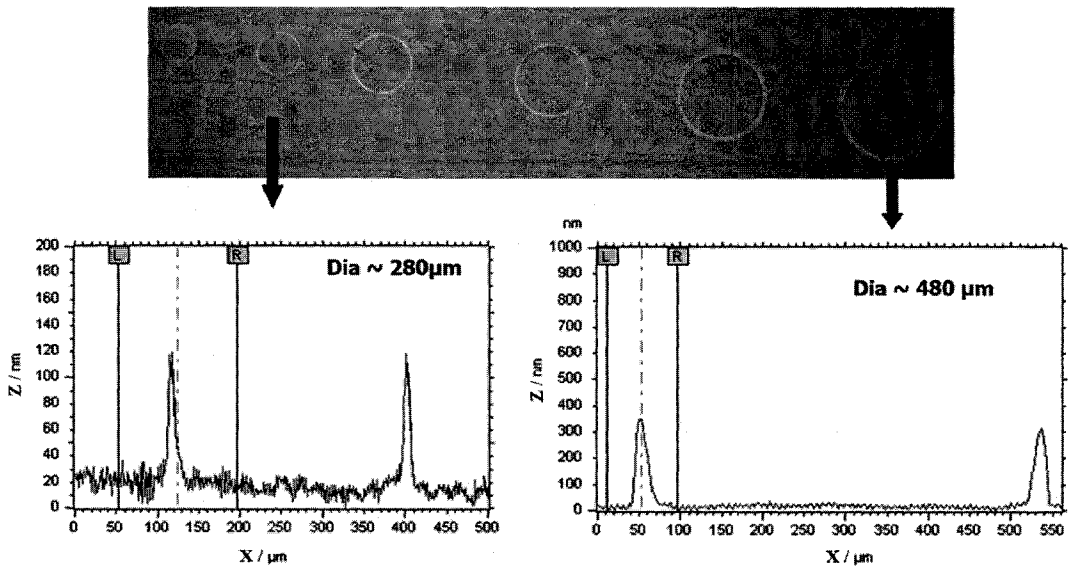

Figure 1.2 Exploitation of coffee drop effect to make completely hollow rings of varying diameters

This novel technique of inkjet printed hollow micro-rings found potential application in the fabrication of polymeric vertical field effect transistors, humidity

sensors with enhanced sensitivity and polymer light emitting diodes with higher resolution (> 200 pixels/inch). Polymers such as, PEDOT:PSS and PPy were used as conducting polymers, and MEH-PPV was used as semiconducting electroluminescent polymer for the fabrication of above mentioned devices.

Initially, the layer-by-layer nanoassembly technique for self-assembly of conducting polymers was used. Enhanced conductivities of the self-assembled films were obtained. These self-assembled films of conducting polymers were incorporated in the fabrication of humidity sensors.

1.2 Dissertation Overview

The second chapter discusses the fundamentals of conduction mechanism of conjugated polymers. This chapter also focuses on the inkjet printing technique and layer-by-layer self assembly technique for fabricating conducting polymeric thin films.

The third chapter discusses about the factors affecting the drop before and after drying. A flow chart has been formed for the techniques to be used for the fabrication of micro-rings of varying diameter and height. Empirical analysis of two dispensing techniques, "instant dispensing" and "dispense and dry" was done for varying diameter and height of micro-rings with respect to number of drops dispensed.

The fourth chapter demonstrates the initial design and experimentation for self-assembly of conducting polymer layers. Annealing step was introduced in the layer-by-layer assembly, which shifted the layer deposition from super-assembly to linear assembly and also enhanced the conductivity of the films. These self-assembled films are used in fabrication of polymer field effect transistor and effect of self-assembled layers on device characteristics is studied.

The fifth chapter discusses the design and fabrication of micro-rings using inkjet printing technique. Substrate temperature and drop dispensing techniques were optimized for the fabrication of micro-rings with varying height and diameter. These micro-rings are applied for the fabrication of vertical field effect transistors, humidity sensors with enhanced sensitivity and polymer light emitting diodes with higher resolutions.

Finally, the sixth chapter presents a summary of the results and suggestions for future work.

CHAPTER 2

LITERATURE REVIEW

2.1 Conjugated Polymers

2.1.1 Charge Conduction Mechanism

The discovery by Heeger, MacDiarmid, Shirakawa and co-workers that the conductivity of polyacetylene (Figure 2.1 a) could be increased by more than seven orders of magnitude upon doping with iodine or arsenic pentafluoride (AsF_5) [16] led to great interest in this and similar materials (and to the award of the 2000 Nobel Prize for Chemistry to these three researchers). The chemical formulae of some of the other important organic conducting polymers (before doping) are shown in Figure 2.1 b.

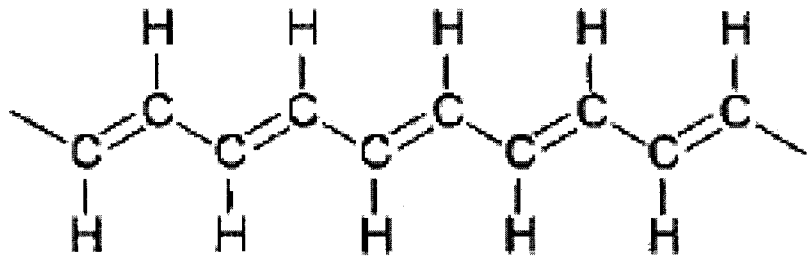

Figure 2.1 a) Chemical formula of polyacetylene – first conducting polymer discovered by Heeger, MacDiarmid, Shirakawa [16]

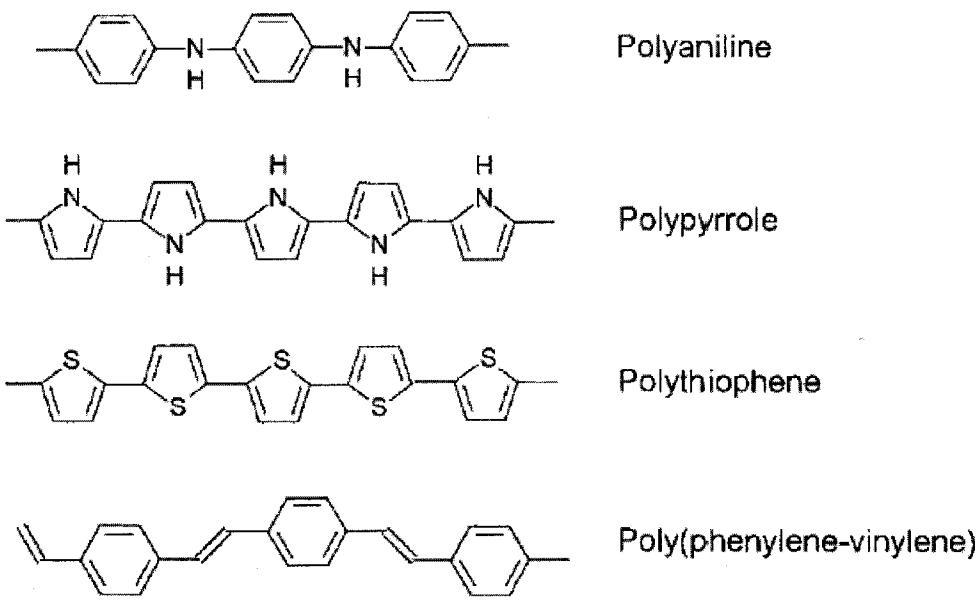

Figure 2.1 b) Chemical formulae of some of the important organic conducting polymers [16]

It can be seen that a common feature in these polymers is the occurrence of double bonds alternating with single bonds along the polymer chain (conjugated bonds). The reason that polymers with conjugated bonds form the basis of the organic conducting polymers can be understood as follows. In these polymers, three of the four electrons in the outer shell of carbon occupy hybridized states formed from one s and two p states (sp^2 hybridization). These electrons form three strong 'σ bonds' that play the key role in forming the polymer structure. For example, in polyacetylene each carbon atom forms these σ bonds with one hydrogen and the two neighbouring carbons. That leaves one valence electron left over (the π electron), which occupies a p orbital. The π electron wavefunctions from adjacent carbon atoms overlap to form a π band. With each delocalized orbital having only one electron, this band would be half-filled and might therefore be expected to be metallic because there would be a finite density of states at

the Fermi level, and hence many states available for metallic conduction, as shown in Figure 2.2.

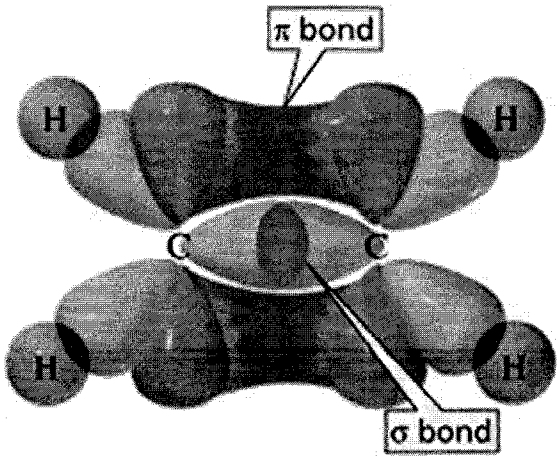

Figure 2.2 sp^2 hybridization depicting σ and π bond [16]

However, the energy of the system is lowered if the π electron density is increased between every alternate pair of carbon atoms to form a π bond in addition to the σ bond, i.e. if conjugated bonds are formed, as shown in Figure 2.1a. An energy gap then appears in the middle of the π electron band between filled bonding states (the π and) and empty antibonding states (the π^* band), lowering the energy of the filled states. For polyacetylene this band gap is proximately 1.7 eV, so pristine polyacetylene shows no metallic conductivity, but only a very small semiconductor-like conductivity [16]. The extra π bond causes the pair of atoms with double bond to move slightly closer together. This dimerization and the associated band gap reflect the fact that a 1D metal is unstable in the presence of interactions such as, the electron–lattice coupling (the Peierls instability). In fact, *ab initio* calculations indicate that the dominant cause of the dimerization in polyacetylene is electron–electron interactions, particularly atomic correlations [17].

The presence of conjugated bonds indicates the presence of relatively weakly bound π electrons, with the possibility of metallic behavior if there exists a mechanism to eliminate the band gap between the filled and empty states. As Chiang et, al., [16] showed, this can be achieved by doping with an electron acceptor such as iodine, which leads to the formation of additional states in the $\pi - \pi^*$ band gap: electrons are transferred from the polymer chain to the dopant, and mobile charged excitations become possible. Note that the doping to produce this conductivity differs from doping in semiconductors in that the ratio of dopant molecules to carbon atoms is typically several percent, orders of magnitude greater than typical doping concentrations for semiconductors.

2.1.2 Hopping in Polymeric Semiconductors

In the hopping mechanism, charge carriers tunnel between localized states in the energy band gap [18-22]. Charge carriers travel through repeated hopping. The external energy boost required for the charge carriers to travel through the sample, exists in materials at non-zero temperatures in the form of phonons. In cases where the hopping mechanism applies, the conductivity at zero temperature is zero. However, at finite temperatures, electrons can get energy from phonons. Thus, by absorbing phonons, electrons can hop from one localized state to another. Phonons are in this case a source of electrical conductivity, and hopping conductivity increases with temperature because of more available phonons. The probability of a hopping event depends on the physical distance to another site/chain and the difference in energy between the sites. Hence, the extent of hopping and the hopping range are limited by the available energy in form of phonons. As the temperature increases more phonons of higher energy becomes available

and the electrons can hop to states further and further away or higher in energy [23]. Figure 2.3 represents variable range hopping in a simple way.

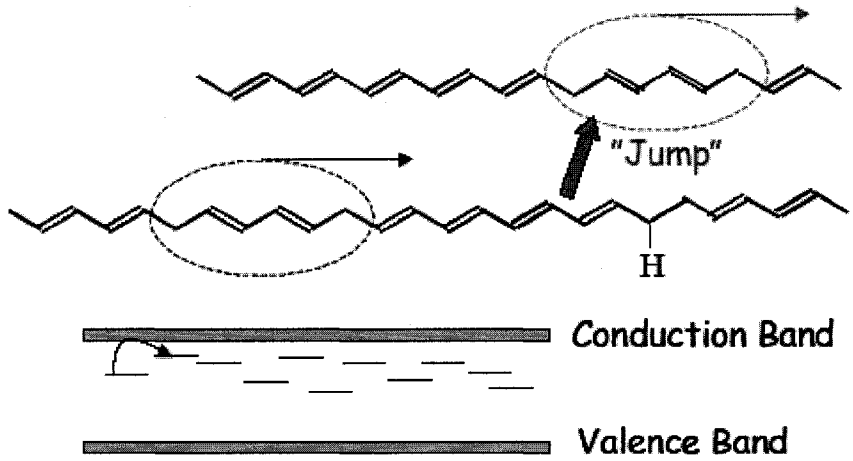

Figure 2.3 The principle of the variable range hopping mechanism [23]

2.1.3. Conduction in Heterogeneous Polymers

Crystallinity in polymers typically differs from that in low-molecular-weight compounds in that it is only partial: the polymer chains are not aligned with each other over their whole length, but only in small crystallite regions of typical dimensions 10–50 nm [24-26]. Particular polymer chains may extend through a number of crystallite regions, or they may be folded back on themselves within the crystalline regions; in either case the ordered crystallites are interconnected by amorphous regions, as illustrated in Figure 2.4.

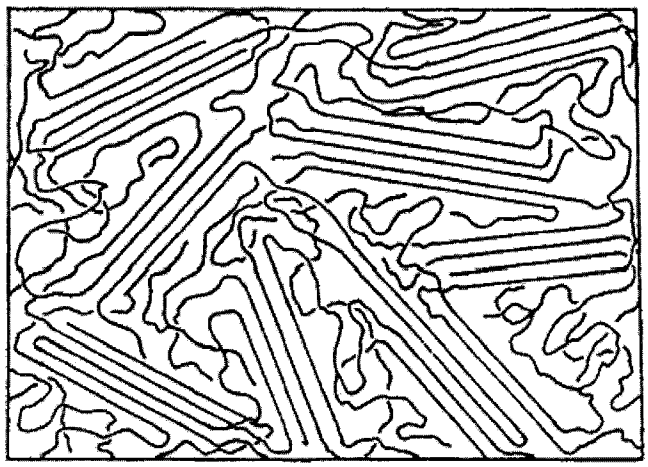

Figure 2.4 The fringed crystallite model for the crystalline–amorphous structure of polymers [24]

In general, it might be expected that a similar heterogeneity in conducting polymers plays a significant role in the conduction mechanism. If the conductivity of ordered crystalline regions is high, the total resistance of the conducting polymer will be dominated by the disordered regions through which the current must pass. X-ray studies show that organic conducting polymers are only partially crystalline in nature [27]. The only exception appears to be polydiacetylene [28], which can be made from a crystalline precursor material, but this polymer has only a relatively low conductivity. The morphology proposed for fibrillar highly conducting polyacetylene [29] is shown in Figure 2.5.

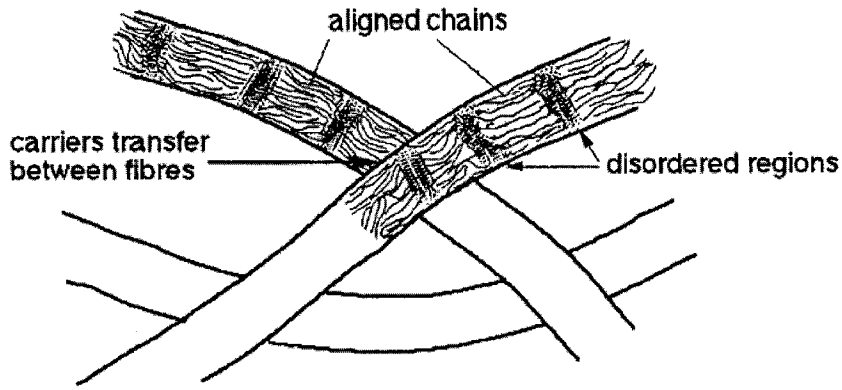

Figure 2.5 A sketch of structure of highly doped fibrillar polyacetylene [24]

2.1.4. Solitons, Polarons, and Bipolarons

The elementary excitations for the single polyacetylene chain are solitons rather than electron–hole pairs as in three-dimensional metals. Solitons represent discontinuities in the pattern of alternating single and double bonds that arise when one carbon atom has single bonds to both of its neighbouring carbons [30-31]. Additional electronic states are created at the centre of the semiconductor-like band gap in polyacetylene, as shown by optical absorption measurements at low doping levels. Motion of a simple soliton discontinuity along a polymer chain does not lead to charge transport, but an inter-chain soliton hopping mechanism could contribute to conduction with conductivity varying as a high power of temperature [32]. However, the agreement of a vast amount of conducting polymer data with the hopping laws over a wide temperature range suggests that once localized states are formed in the gap by whatever mechanism, conduction takes place predominantly by the usual variable range-hopping processes for lightly or moderately doped samples [33]. In heavily doped samples, the overlap of wavefunctions means that a metallic picture is likely to be more appropriate, at least in the ordered regions.

For conducting polymers other than polyacetylene, different solitonic states have different energies, so solitonic conduction mechanisms are not expected. However, states appear in the band gap [34] owing to the formation of polarons (electrons localized in an electric potential minimum formed by lattice deformations). Polarons have both charge and spin, and their motion can contribute to charge transport. Polarons of opposite spin often pair up to form bipolarons with zero spin, which can lead to charge transport without spin transport.

a. Example of PPy depicting role of solitons, polarons, and bipolarons

The polymer may store charge in two ways. In an oxidation process it could either lose an electron from one of the bands or it could localize the charge over a small section of the chain. Localizing the charge causes a local distortion due to a change in geometry, which costs the polymer some energy. However, the generation of this local geometry decreases the ionization energy of the polymer chain and increases its electron affinity making it more able to readily accommodate the newly formed charges. This method increases the energy of the polymer less than it would if the charge was delocalized and, hence, takes place in preference of charge delocalization. This is consistent with an increase in disorder detected after doping by Raman spectroscopy. A similar scenario occurs for a reductive process [35].

For a very heavily doped polymer, it is conceivable that the upper and the lower bipolaron bands will merge with the conduction and the valence bands, respectively, to produce partially filled bands and metallic like conductivity as shown in Figure 2.6.

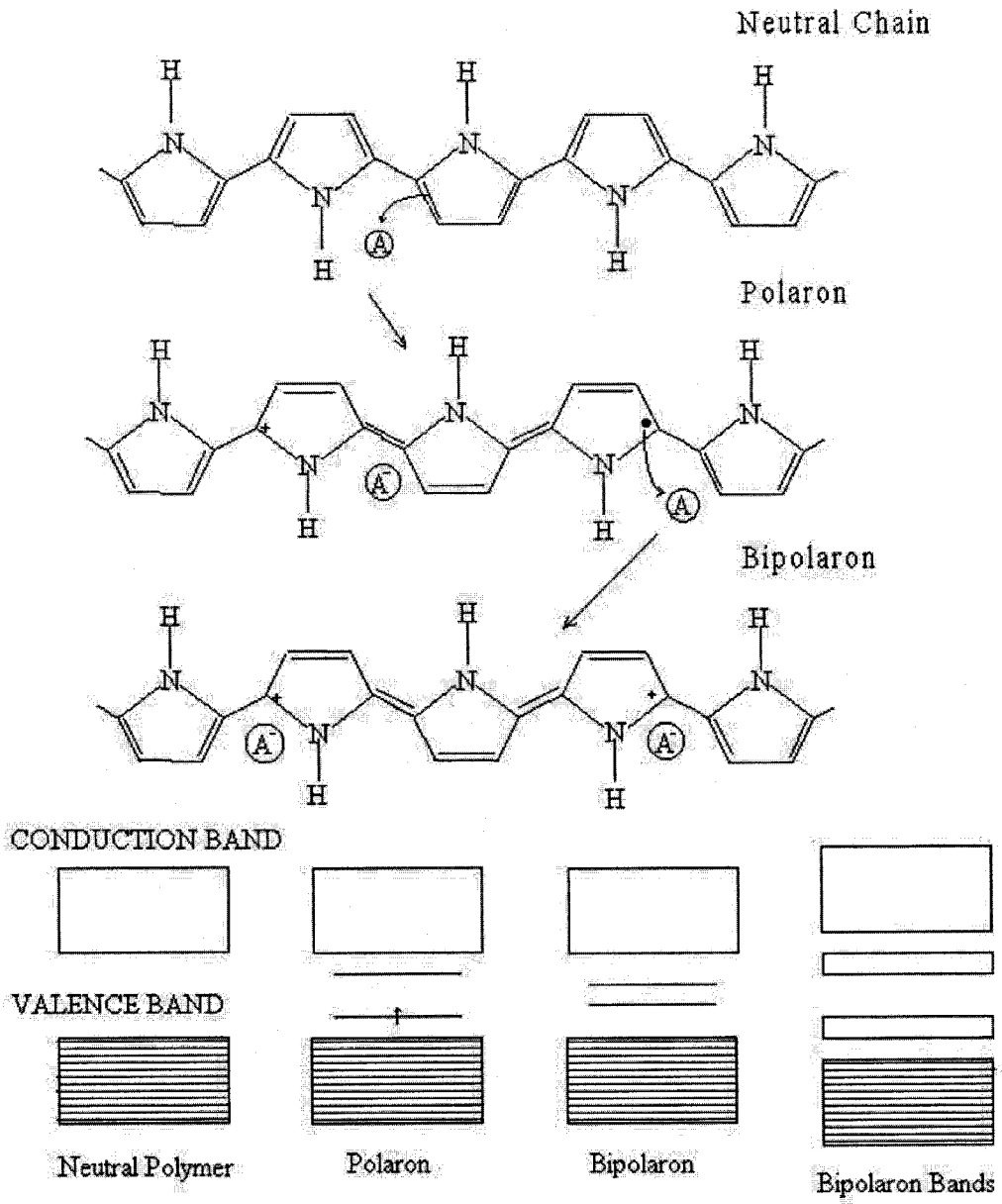

Figure 2.6 Formation of polarons and bipolarons [35]

Conjugated polymers with a degenerate ground state have a slightly different mechanism. As with polypyrrole, polarons and bipolarons are produced upon oxidation. However, because the ground state structure of such polymers are twofold degenerate, the charged cations are not bound to each other by a higher energy bonding configuration and can freely separate along the chain. The effect of this is that the charged defects are

independent of one another and can form domain walls that separate two phases of opposite orientation and identical energy. These are called solitons (shown in Figure 2.7) and can sometimes be neutral.

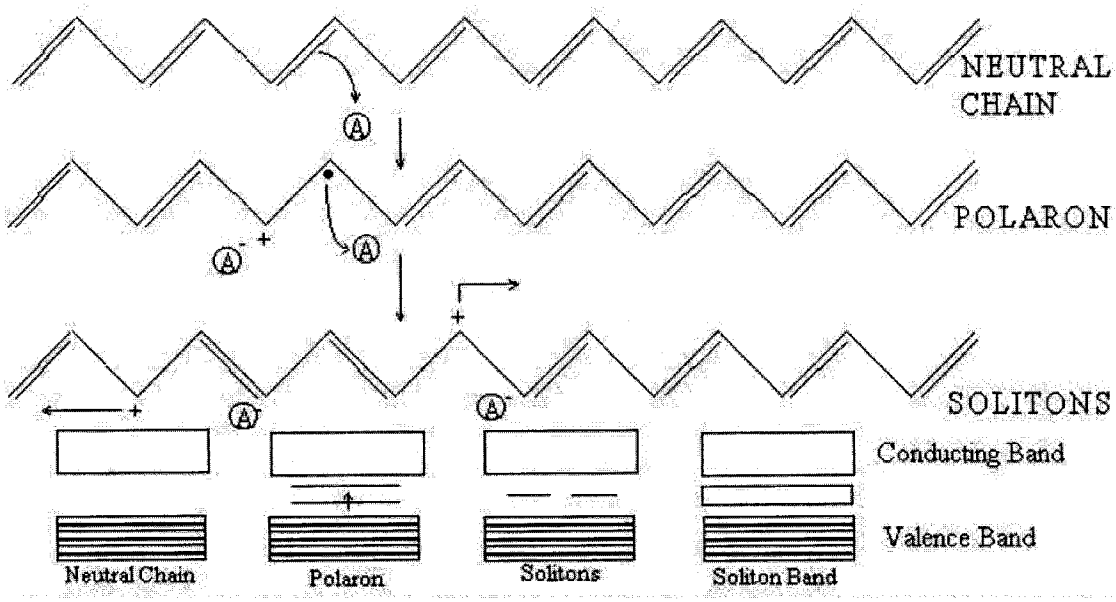

Figure 2.7 Solitons in conjugated chains [35]

Solitons produced in polyacetylene are believed to be delocalized over about 12 CH units with the maximum charge density next to the dopant counterion. The bonds closer to the defect show less amount of bond alternation than the bonds away from the center. Soliton formation results in the creation of new localized electronic states that appear in the middle of the energy gap. At high doping levels, the charged solitons interact with each other to form a soliton band which will eventually merge with the band edges to create true metallic conductivity.

2.2. Specific Materials

2.2.1 Poly(3,4-ethylenedioxy thiophene):poly(styrene -sulfonate)(PEDOT:PSS)

Scientists at the Bayer AG research lab in Germany developed a new polythiophene derivative, poly(3,4-ethylenedioxythiophene) (PEDOT), in 1980s. The structure of PEDOT:PSS is shown in Figure 2.8. This polymer was initially developed to give a soluble conducting polymer that lacked the presence of undesired couplings within the polymer bone. It was an insoluble polymer with very high conductivity, transparent in thin oxidized films and high stability in the oxidized state.

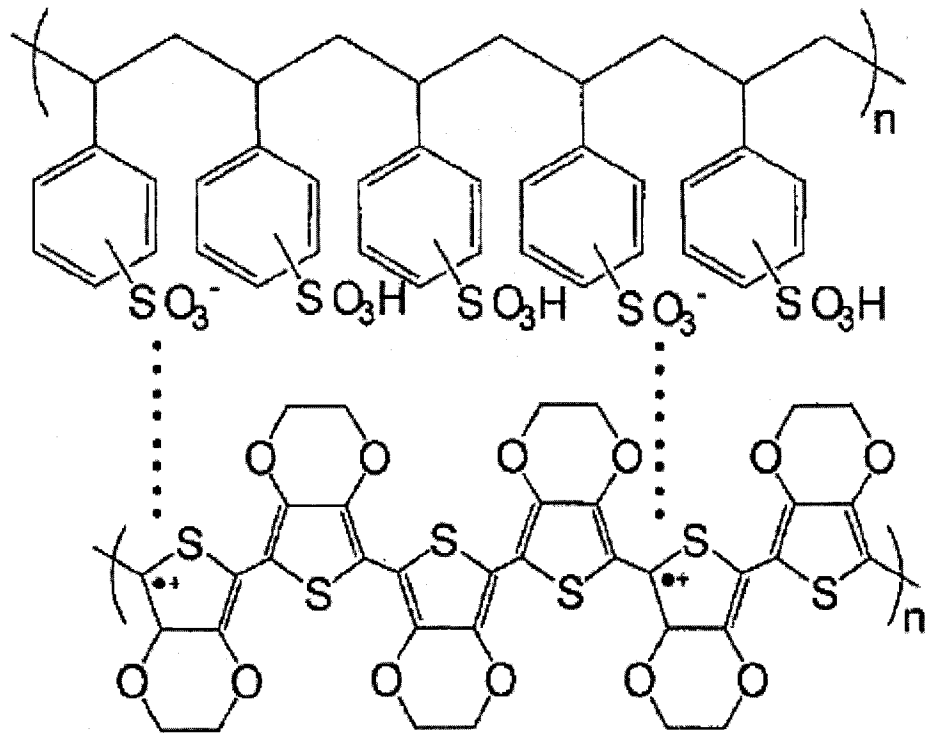

Figure 2.8 Molecular structure of PEDOT: PSS [36]

The conductivity of poly(3,4-ethylene dioxythiophene): poly(styrene sulfonate) film can be enhanced by over 100-fold with the addition of dimethyl sulfoxide (DMSO),

N,N-dimethylformamide (DMF), glycerol, or sorbitol to the aqueous solution of PEDOT:PSS. [36-39]. High quality films can easily be formed on various substrates by various processing techniques thus rendering them with high thermal stability and high transparency in visible range. The PEDOT:PSS is extensively used in various electronic devices such as, flexible electrodes, hole transport material in polymer light emitting diodes, electrochromic displays, supercapacitors and polymer transistors [40-44]. Still the conductivity of PEDOT:PSS is lower than that of many conducting polymers by few orders of magnitude which affects some of the applications [45-49].

Good adhesion and scratch resistance of PEDOT:PSS coatings on glass are achieved by addition of silanes. The PEDOT:PSS is also used in the electrostatic coating of non-conducting surfaces such as plastic, wood and glass. It is used for antistatic finishing of plastic or glass surface. e.g. packaging films in the electronic sector.

2.2.2 Polypyrrole (PPy)

PPy is an electronically conductive polymer which has received considerable attention due to its high electrical conductivity, facile synthesis and relatively good stability of the oxidized state of the polymer. It is an inherently conductive polymer due to inter-chain hopping of electrons. It incorporates an anionic dopant to compensate for the cationic charge carried by its backbone [50]. PPy is easily prepared by either an oxidative chemical polymerization, or using electrochemical oxidation in aqueous or organic solutions by applying a positive potential to a monomer solution containing an appropriate supporting electrolyte. The electrochemical oxidation of pyrrole, which involves the formation of radical cations and subsequent polymerization, is shown in Figure 2.9 [51]. In its oxidized state, it has been found that polypyrrole contains one

positive charge per three of four pyrrole rings, while the polymer is neutral in its reduced state [52]. During the polymerization, anions in the electrolyte solution are incorporated into the polymer film to maintain the charge balance. The presence of these dopants greatly alter the properties of the polymer, and by using different counter ions during the polymerization it is possible to create polymers for many different applications [53-55].

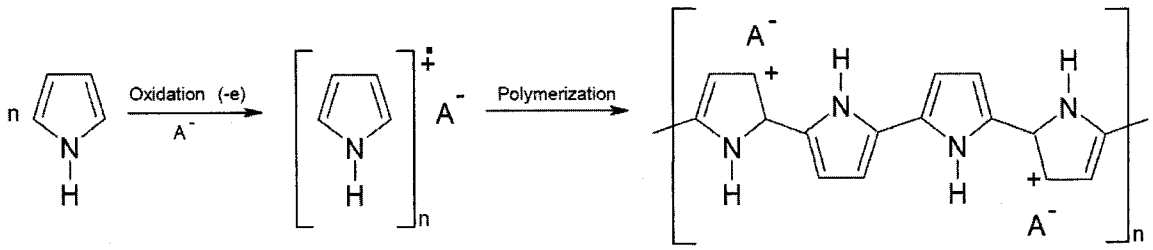

Figure 2.9 Polymerization reaction of pyrrole to yield polypyrrole [51]

2.2.3 Poly [2-methoxy-5-(2-ethyl hexoxy)-1, 4-phenylene vinylene] (MEH-PPV)

The chemical structure of MEH-PPV is shown in Figure 2.10.

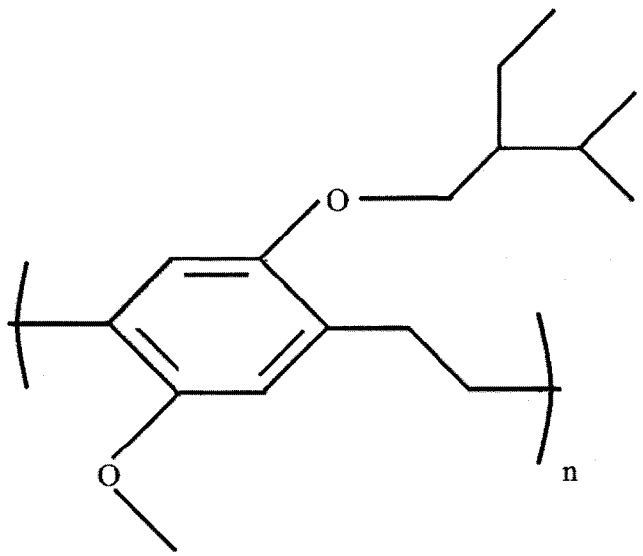

Figure 2.10 Molecular structure of MEH-PPV

Organic electroluminescent conjugated polymers such as MEH-PPV are technologically important materials for display applications because of the ease of processing and flexibility in synthesis. Fundamentally, they represent a new class of materials in which charge carrier transport occurs between closely packed electronically active chromophores, deserving further understanding.

Poly *p*-phenylene vinylene (PPV) and its soluble derivatives have excellent luminescent properties [56–59]. Extensive studies on the morphology and photophysics of the films have been documented in the literature, however, with less work on the charge transport studies. The relationship between the charge transport and morphology [60,61] is important in the design of light-emitting diodes, lasers [62], and transitors [63]. The change in photophysical properties depending on the processing conditions results in the change in the efficiency of the LED's [64–67].

2.3 Fabrication Techniques

2.3.1 Inkjet Printing

In recent years, much effort has been invested in turning inkjet printing into a versatile tool for depositing exact quantities of materials especially in the field of organic transistors, polymer light emitting displays, cereamics and biopolymer arrays [68-70]. In the electronic industry, lithographic etching and controlled vapor deposition are some of the techniques used to deposit semiconductors. These techniques are very expensive and are very time consuming. Thus application of inkjet printing of polymeric semiconductors is very good solution to reduce costs [71]. However, the application of inkjet printing for the deposition of polymer from solution results in various challenges

such as print head design, ink formulation, substrate choice, control of solvent evaporation, etc., [72].

2.3.1.1 Fundamentals of inkjet Printing

Inkjet deposition is a method in which the polymer solution takes the place of the toner in the printer. In this method the polymer pattern can be directly printed onto the substrate. The technique relies on the steering of material containing droplets discharged from the nozzle and their contained impact and solidification on the substrate. With this technique high-resolution patterns can be printed on the substrate. The advantages provided by the inkjet printing include exact control of dispensed volume and data driven *in situ* processing. Two approaches are typically used for inkjet printing of materials for manufacturing applications; continuous inkjet printing (CIJ) and drop-on-demand inkjet printing. CIJ printing is a method in which an ink stream continuously runs under pressure, and a sinusoidal agitation of the fluid allows the fluid to break up into a train of droplets. A schematic of CIJ is shown in Figure 2.11. A piezo crystal in contact with the fluid is typically used to provide this sinusoidal agitation. As the stream breaks into droplets, these droplets pass through what is called a charge tunnel made of conductive material and connected to a quanitzer [73]. Each droplet is given an individual charge as it passes through the charge tunnel. Once through the charge tunnel the droplets enter a constant electrostatic field and deflect from their flight path at an angle proportional to how much charge was induced upon them in the charge tunnel. This electrostatic field is produced by what are called deflection plates that are connected to a high-voltage DC power source. Droplets not to be deflected are given a negligible charge and therefore experience negligible deflection.

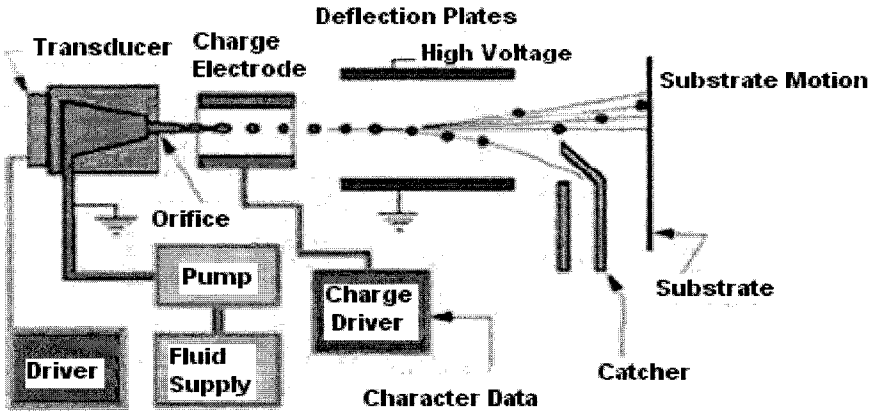

Figure 2.11 Continuous inkjet printing technology [73]

A more widely used and a simpler approach for smaller drop (80-100 μm) diameter, lower frequency (up to 20KHz) printing applications is the Drop-on-Demand (DOD) technology as shown in Figure 2.12. In DOD, a drop is only ejected from the device orifice when a voltage pulse is applied to a transducer. Since the fluid at ambient pressure in the device is coupled to the transducer, the acoustic waves generated by application of an electrical pulse eject a drop from the device orifice. The DOD device produces drops approximately equal to the orifice diameter of the droplet generator.

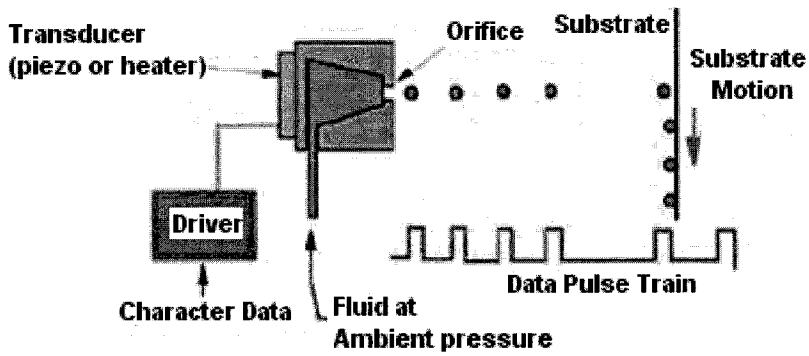

Figure 2.12 Drop on demand inkjet printing technology [73]

2.3.1.2 AutoDrop inkjet printer

In this work the Autodrop system is used for printing the polymers because of several disadvantages that are associated with commercial inkjet printing system such as (1) low resolution, (2) poor repeatability, (3) use of only flexible substrates, (4) problems in alignment and (5) heating of substrate. Therefore printing system with high spatial resolution and positioning system is used. Autodrop platform from Microdrop used for drop-on-demand inkjet printing of micro-rings is shown in Figure 2.13.

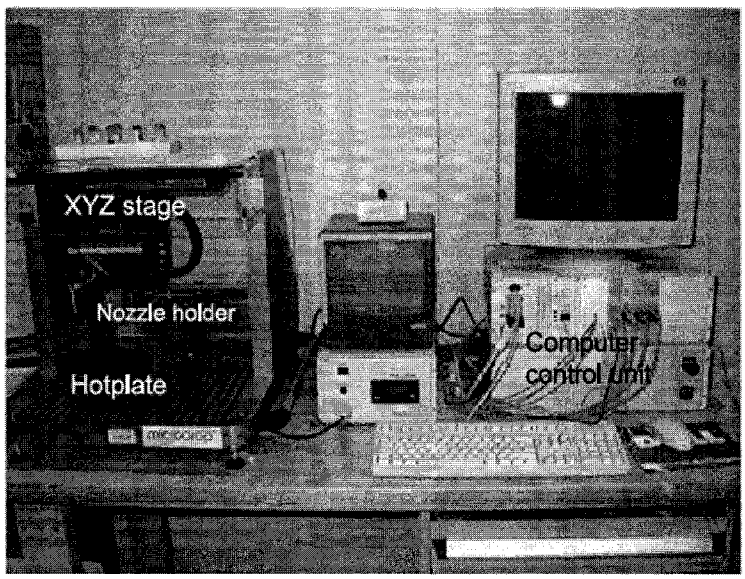

Figure 2.13 Microdrop dispensing system

A dispenser head together with a 4 ml ink reservoir is installed on the dispensing racket, which is capable of accommodating four nozzles simultaneously [74]. The nozzle is activated by a voltage pulse, of which the voltage amplitude, pulse width, and frequency are adjustable through the computer software. A positioning system controls the movement of the nozzle in a XYZ station. The positioning accuracy is ±10 μm and repetition accuracy is ±2 μm. The maximum speed of the head movement is 12.5cm/sec. The minimum step width is 0.5 μm in the X and Y direction and is 1 μm in Z direction.

The substrate stage is a hotplate controlled by a proportional, integral and derivative regulator so that the substrate can be heated up to 150°C.

2.3.1.3 Dispenser heads

Microdrop dispenser heads are designed for dispensing small amounts of liquid. Dispenser heads are available with or without heating element. Dispensers without heating are designed for liquids with viscosity of upto 10 mPas and dispensers with heating are capable of dispensing liquid with viscosities between 10 and 10,000 mPas (Figure 2.14). The temperature can be varied from room temperature to 160°C [74].

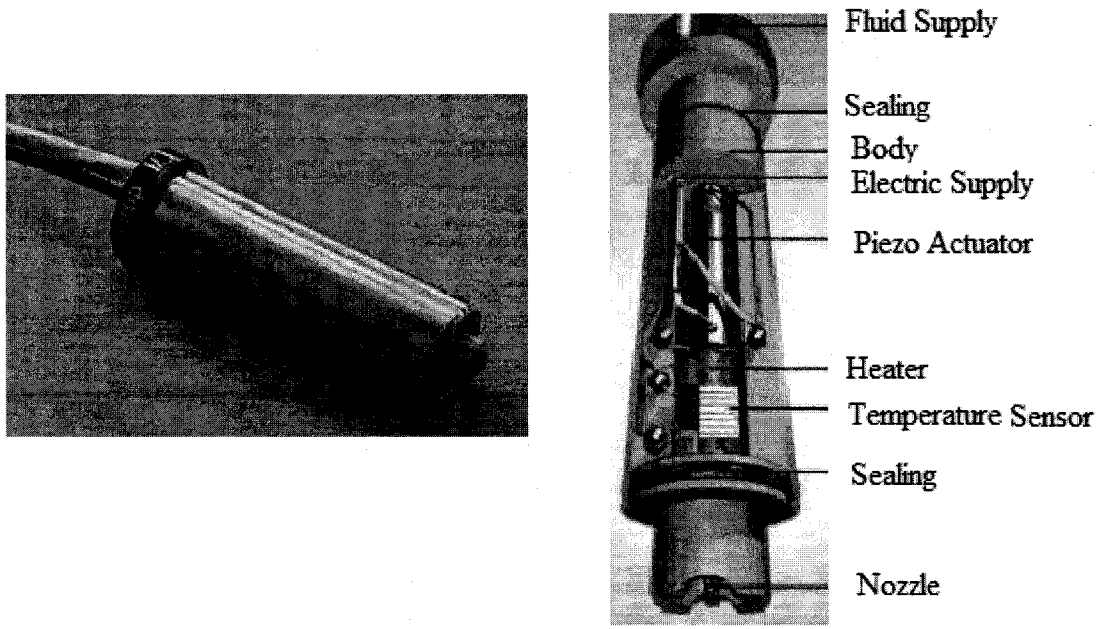

Figure 2.14 Dispenser head with and without capping [74]

Microdrop dispenser systems are based on the principle of inkjet printers. A capillary system filled with liquid is put under pressure by piezo actuator. The piezo actuator is supplied with short electrical pulses transferred into short pressure pulses. These pulses are propagated through the liquid and are transformed into a motion of

liquid in the nozzle. Here the liquid is accelerated and reaches the velocity of several meter/second which allows the formation of liquid jet to emerge from the nozzle. After a very short period of time, the liquid is decelerated due to the pressure loss through the nozzle and expansion of the actuator. Due to the inertial forces and supported by surface tension, a small volume of liquid breaks off and forms a droplet which flies freely through the air with a velocity of typically 2-3 m/s.

2.3.1.4 Software description

All functions of the Autodrop Dispenser system are controlled by a control software written in C++ and running under Windows. Driver parameters such as, pulse voltage and pulse duration, automatic filling, cleaning and emptying, drop detection, positioning and dispensing of various patterns can be performed. A macro programming allows the composition of complex procedures to be executed automatically. Figure 2.15 shows the main menu for control of upto four dispenser units. All dispensing and positioning procedures are executed from the main menu [75].

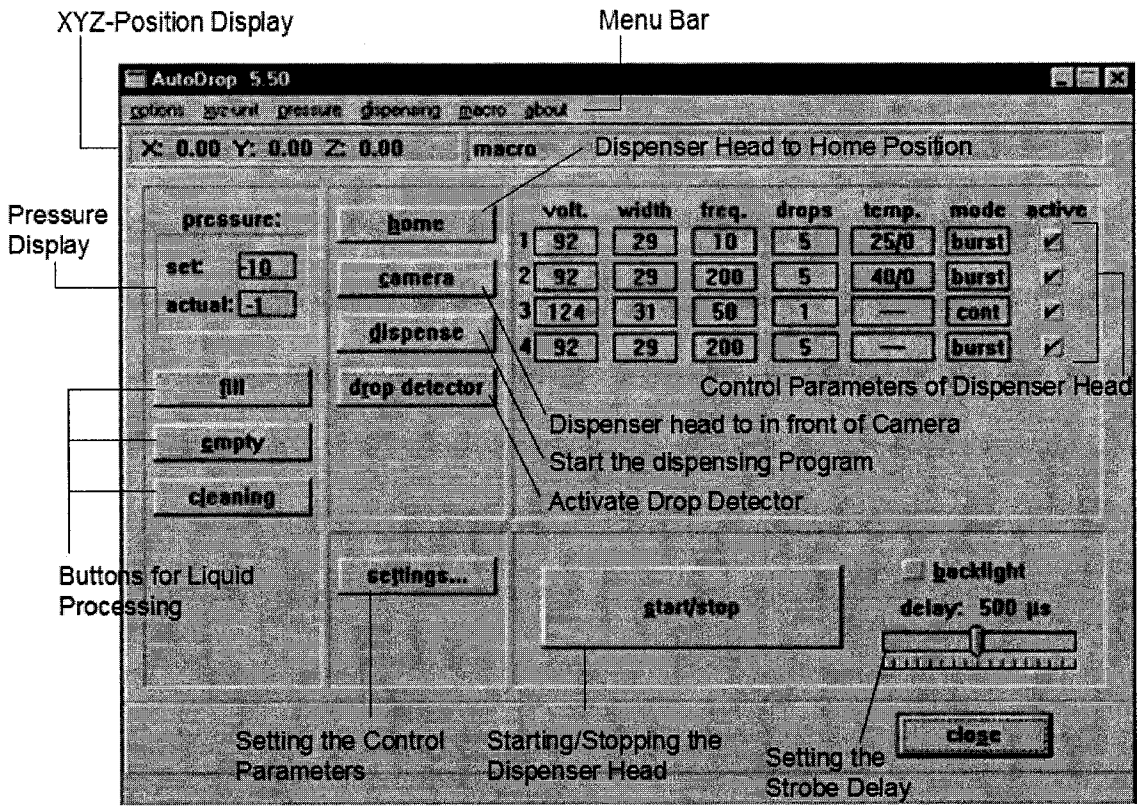

Figure 2.15 Main menu for controlling up to 4 dispensing units [75]

The menu "Dispensing" only offers the menu command "Setting of Dispensing." After activation, the following window (Figure 2.16) appears. Here we can set the type of dispensing patterns, mention the spacing between two drops, change the matrix size of the dispensed drops and specify the displacement in adjacent lines. Another main parameter that can be selected is "dispense in-flight" by controlling the move parameters.

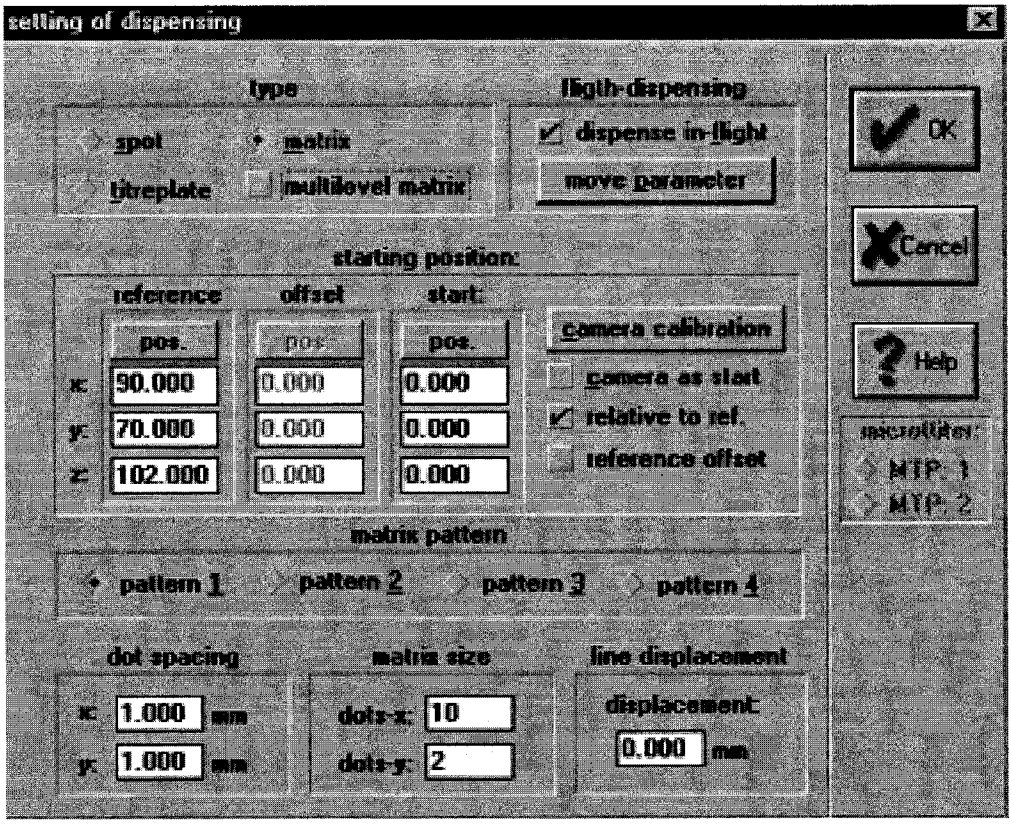

Figure 2.16 Setting of dispensing parameters [75]

Activating the setting button with the number of the dispenser head, opens the following menu (Figure 2.17).

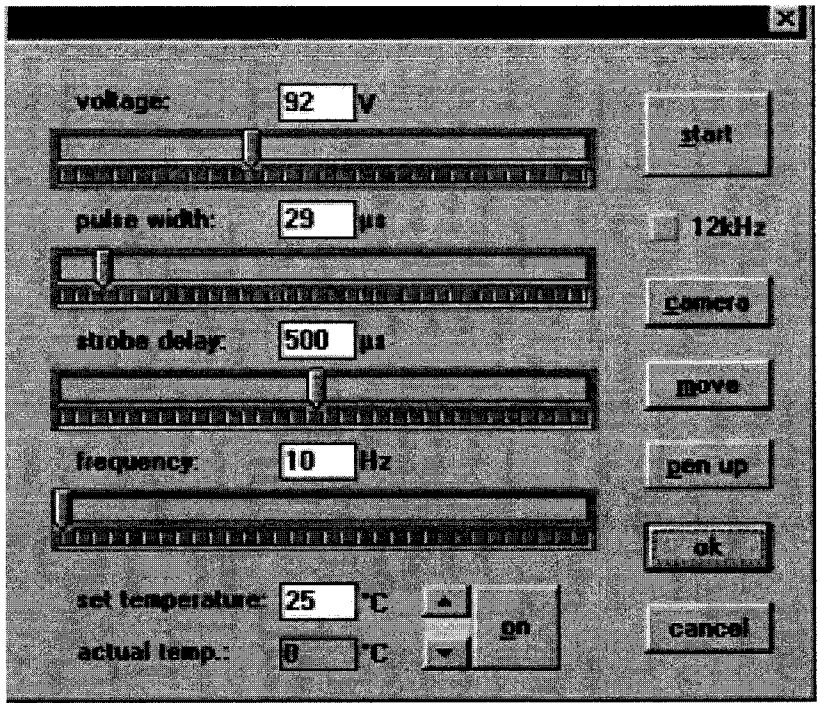

Figure 2.17 Drive parameter setting [74]

The adjustable inputs in the drive parameter setting window serve the following purposes [75].

- Drive Voltage: The adjustable drive voltage range is from 30V – 330V. A higher voltage causes larger amplitude in the piezo actuator, which leads to a higher pressure difference in the liquid. The drop is thus accelerated more strongly and reaches a much higher flow speed.
- Pulse Width: The pulse width can be set to between 10 to 255 µs. The drop form is changed by varying the settings of the pulse width.
- Strobe Delay: The strobe delay period lights the drops with the same frequency at which the drops have been created so that still drop image can be observed.
- Drop Frequency: The drop frequency value ranges from 1 to 2048 drops/sec. The time span between the individual drops is set by drop frequency.

2.3.1.5 Coffee drop effect and its exploitation

It is a well know fact that a coffee drop leaves a stain with most of the particles accumulated at the periphery of the drop. As shown in Figure 2.18, the coffee stain at the outer edges is more prominent in the form of a ring.

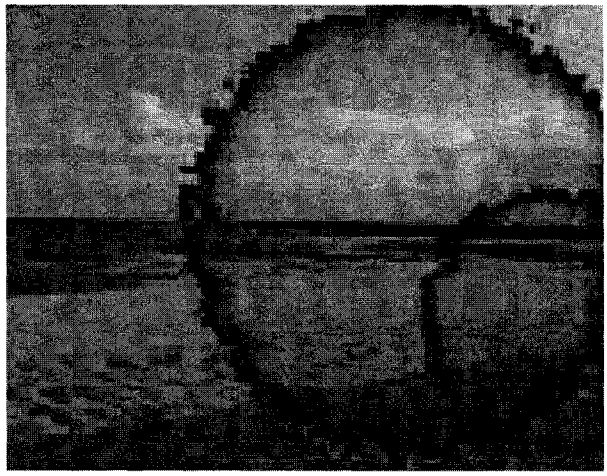

Figure 2.18 Coffee drop stain in the form of ring

This effect is considered as a major drawback and needs to be eliminated for the uniform deposition of polymeric thin films by inkjet printing. During the study of inkjet printing of conducting polymers in our lab, we also encounter this drop effect. This effect was observed under Atomic Force Microscope (AFM). The AFM images of the drops dispensed with most of the polymer deposited on the outer edge and fewer particles in the center of the drop are shown in Figure 2.19.

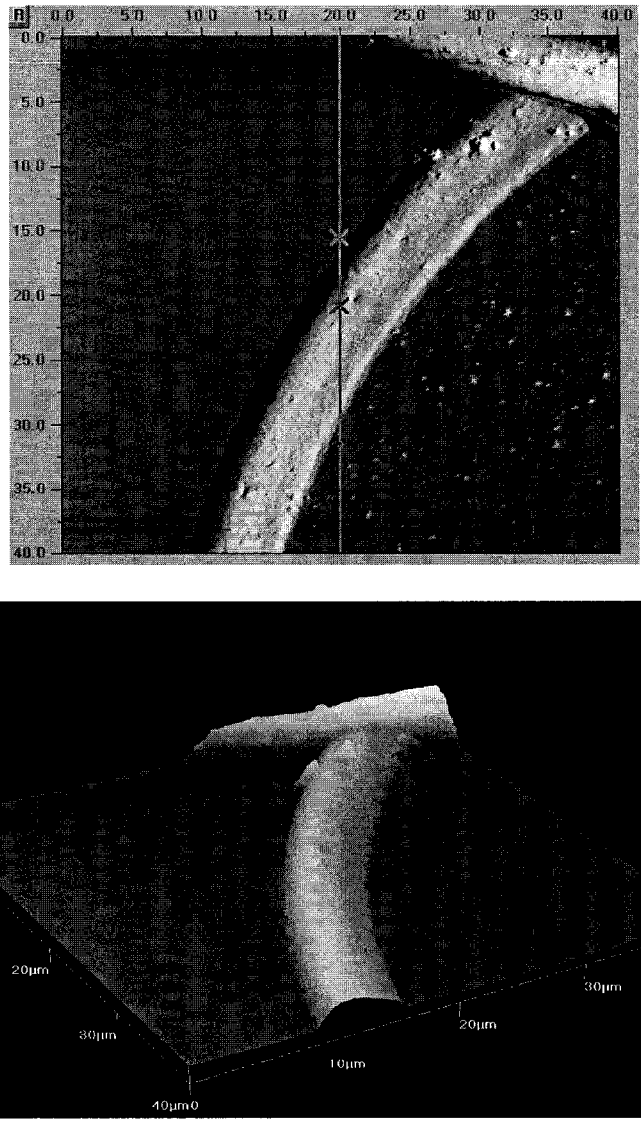

Figure 2.19 Atomic force microscope images of the thicker ridge of drop

This phenomenon is attributed to the following points [12-14]:

1. Surface roughness: surface roughness fixes the edge of the drop so that it does not shrink as the drop evaporates.
2. Rate of evaporation: The evaporation at the edge is faster than the evaporation in the middle. So in order to compensate the evaporation loss, the liquid from the middle moves outwards, thus carrying the solute particles to the edge.

3. Size of the solute: Small solute particles move outwards faster than the large particles. Thus smaller particles make rings with thicker edges as compared to large solute particles.

Instead of eliminating this effect by making the drop more and more uniform, we exploited this effect and made the micro-rings thicker at the edges and thinner at the center. Further the inner thin polymer layer was etched using micro – RIE rendering the micro-rings the shape of 'Torus'.

2.3.2 Layer-by-Layer Nanoassembly

2.3.2.1 Basic principle of layer-by-layer nanoassembly

LbL self-assembly is a unique method for the deposition of composite films with nanometer precision and has rekindled widespread interest in the field of nanotechnology. The attractive feature of this approach is its ability to assemble complex structures from modular components and integrate them into self-assembling constructions for a wide range of applications [76-78]. In "self-assembled" systems, basic construction units spontaneously associate to form a particular structure, the architecture of which is solely determined by the bonding properties and "shapes" of the individual components. These systems proceed towards a state of lower free energy and greater structural stability. Another feature of self-assembly is hierarchy, where primary building blocks associate into more complex secondary structures that are integrated into the next size-level in the hierarchy. These hierarchical constructions may exhibit unique properties that are not found in the individual components [79-84]. In this technique, a charged substrate is exposed alternately to dilute aqueous solutions of oppositely charges polycations and

polyanions that enables electrostatically driven deposition of these polyelectrolytes as thin films of controlled thickness and composition.

2.3.2.2 Nanoassembly of conducting polymers

Rubner and co-workers developed this technique for controlled deposition of doped conducting polymers [85-90]. Self-assembly of polypyrrole in its neutral and conducting form has been done in alternation with suitable polyion for the formation of ultrathin multilayers for a wide range of applications [91-93]. Self-assembly of PEDOT-PSS with non-conducting polycationic species such as, poly(hexyl viologen) (PXV), poly(allylamine) hydrochloride (PAH), and poly(ethylene imine) (PEI) has been reported for microelectronic devices as well as electrochromic devices [94-99].

Langmuir-Blodgett (LB) technique has also been applied to conducting polymers for constructing molecular structures. Various electrical and optical devices such as, light emitting diodes, memory devices, sensors and field effect transistors have been fabricated using LB technique. The challenge of fabricating devices by LB technique is to transfer films with vertical deposition without deteriorating their good electrical properties. This is due to the impurities and cavities which are harmful to electrical properties. Thus, the structures of the polymers have to be modified to render them amphiphilic [100]. PEDOT-PSS, PPy and Polyaniline (PAni) are often used in polymer based TFTs and LEDs using spin coating technique. The disadvantage of spin coating is that it is difficult to achieve thin films with nanometer thickness. This factor could be a major criterion for fabricating extremely transparent polymer light emitting diodes and high performance TFTs. Spin coated PEDOT-PSS has been mostly used as a hole transport layer for polymer light emitting diodes and semiconducting layer in the fabrication of polymer

TFTs [101,102]. In PLEDs, the hole transport layer (HTL) tends to control the carrier injection, and increase electron-hole recombination, and as a result the HTL improves the lifetime and efficiency of the device. Self-assembled anionic PEDOT-PSS complex with the non-conducting cationic poly (*p*-xylene-[alpha]-tetrahydrothiophenium) (PXT) exhibit nearly balanced injection, near-perfect recombination, and reduced pre-turn-on leakage currents [103]. This technique uses alternate monolayer of conducting and non-conducting polymer which is further modified by adding hydrazine hydrate to form gradient. We report nano-organized architecture of alternate films of two p-type doped conducting polymers PEDOT-PSS and PPy via LbL. Here, PEDOT-PSS and PPy act as polyanion and polycation, respectively, to form the gradient. The formation of this gradient facilitates controlled carrier hopping.

CHAPTER 3

THEORY OF INKJET PRINTING OF POLYMERIC MICRO-RINGS

3.1 Drop Mechanism

When you spill a drop of coffee on a table, there is dark material deposited on the outer edge after the drop dries. This deposition of material on the outer edge is due to a capillary action in which the contact line of the drying drop is fixed. The contact line of the drying drop is fixed because the rate of evaporation at the outer edge is more than the rate of evaporation in the interior of the drop. To compensate this evaporated liquid from the outer edge, the liquid from the interior moves outward and so does the solute particles as shown in Figure 3.1.

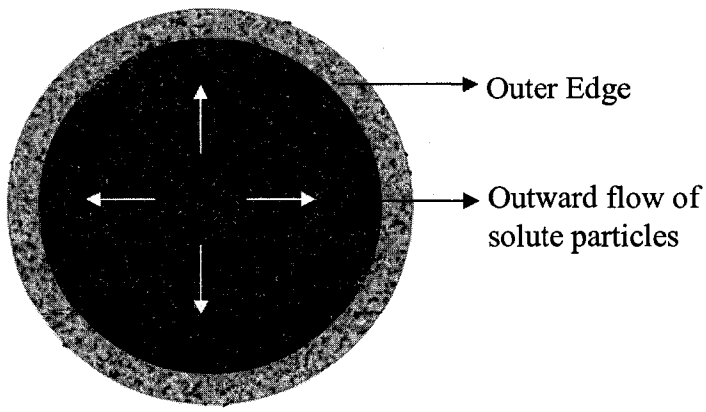

Figure 3.1 Outward flow of solute particles towards periphery

Sidney Nagel and his colleagues at the University of Chicago found that no one has given reasoning behind this phenomenon known as "Coffee drop effect." They determined that ring formation is ubiquitous and robust and does not depend on the solvent as long as the solvent is wetting and volatile. The point of contact should also be fixed. Traditional mechanisms of solute transport such as, Marangoni flow, Rayleigh-Benard convection, diffusion, electrostatic and electrokinetic effects, and wetting phenomenon do not account for ring formation. They Figured out that this phenomenon is some form of unexplored capillary flow. In this capillary action, the outer ring point of contact of the drying drop is fixed and the solute from the inside moves towards outer ring to compensate for the evaporation loss [105].

3.2 Rate of Evaporation

Figure 3.2 shows a cross sectional representation of a drop during an infinitesimal increment of evaporation. The shaded portion represents the volume of liquid removed by evaporation in a single time increment. Figure 3.2 (a) shows that the droplet shrinks as a result of evaporation. The liquid removed from the edge must be refilled by an outward flow of solute particles along with the solvent (indicated by arrows in Figure 3.2 (b).

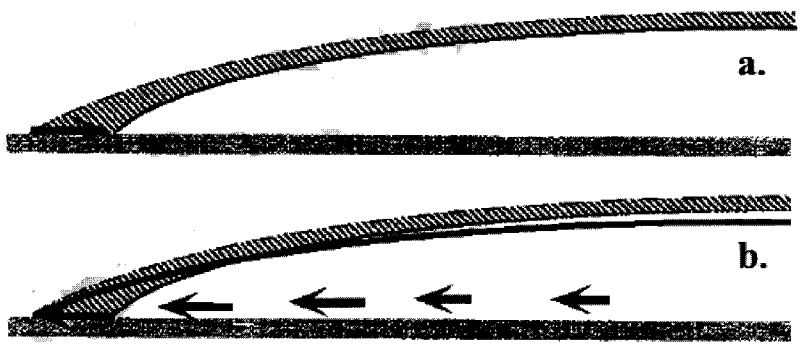

Figure 3.2 a) Shrinking of droplet due to evaporation b) Outward flow to refill the solvent lost due to evaporation [106]

A qualitative analysis by altering the morphology of the ring deposit was done. Since evaporation is the driving mechanism, different deposits can be produced by changing the evaporation profile. Figure 3.3 shows the schematic of the three evaporation profiles and a corresponding image of the resulting deposit. The doted lines indicate the amount of liquid removed at a given radius. When the evaporation profile is such that no water leaves from the edge (Figure 3.3c), no ring is formed [107, 108].

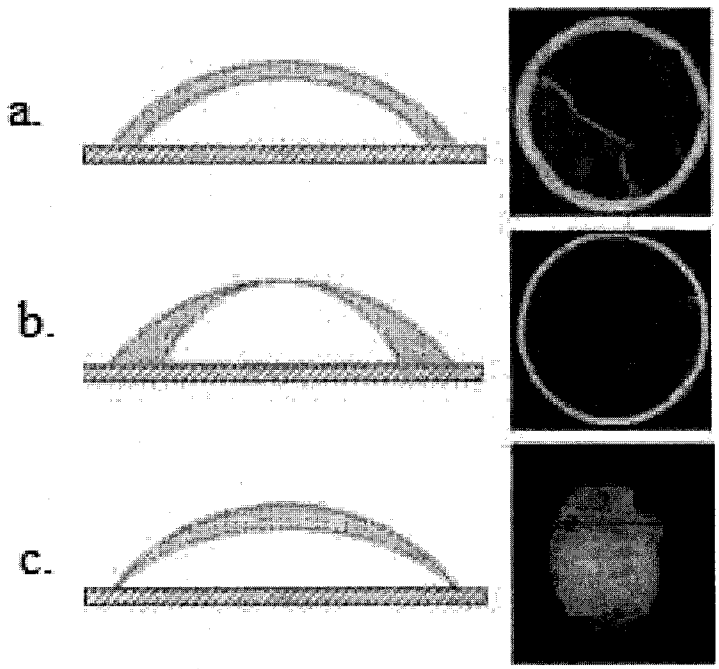

Figure 3.3 a) Uniform evaporation of the drop b) normal evaporation
c) evaporation at the center [107,108]

The outward flow of solute particles is independent of the nature of solute. The size of the solute particles should be small enough, so that sedimentation of these particles does not occur. Moreover the inkjet printed droplet from a 70 μm nozzle is so small that the surface tension is dominant and the gravitational effects are neglected. The balance of surface tension and gravitational force is accounted by Bond number (B_0)

$$B_o = \frac{\rho g R h_o}{\sigma}, \tag{3.1}$$

where ρ is the density of fluid, g is the gravitational constant, R is the size of drop in the plane of substrate, h_0 is the maximum height of the drop before drying and σ is the surface tension at the liquid-air interface.

3.3 Other Factors Influencing Drop Dynamics

Impact energy of the drop: When a drop strikes a surface, its spherical shape is changed into disc form due to spreading. The amount of spreading depends on the balance between driving and resisting forces. The driving force for this impact spreading is the kinetic energy of the droplet. The flow resistance is provided by viscosity and surface tension of the liquid [109]. The relative magnitudes of the kinetic and surface energies can be expressed with Weber number:

$$We = \frac{\rho u^2 d_o}{\sigma}, \tag{3.2}$$

where ρ is the liquid density, u is the impact velocity, d_o is the drop diameter before impact, and σ is the surface tension.

For larger values ($W_e > 1$) of Weber number the kinetic energy of the drop is able to overcome the surface tension of the liquid and thus spreading takes place. For low values of Weber number i.e. low impact velocity, the drop does not change its shape if no wetting takes place [109].

Drop viscosity: The effect of viscosity on the drop can be provided by Reynolds number:

$$R_e = \frac{\rho u d_o}{\mu}, \tag{3.3}$$

where ρ is the liquid density, u is the impact velocity, d_o is the drop diameter before impact, and μ is the liquid viscosity.

Thus, large Reynold number (> 4000) shows that the liquid has low viscosity and thus the kinetic energy of the drop is large enough to overcome the viscous resistance. This leads to the spreading of the drop when it impinges on the surface. Whereas small Reynold number shows that the liquid has high viscosity and the kinetic energy of the drop has very minimal effect on the drop. This reduces the spreading of the drop on impact with the surface.

Spreading factor (d*): It is defined as the ratio of the drop diameters before and after spreading.

$$d^* = \frac{d_1}{d_o}, \tag{3.4}$$

where d_1 is the diameter of the drop after spreading and d_o is the diameter of the drop before spreading.

Contact angle (θ): When a liquid does not spread on a substrate, a contact angle is formed which is defined as the angle between liquid-substrate interface at the line of contact. A contact angle of zero results in wetting, while an angle between 0° and 90° results in spreading of the drop and angles greater than 90° indicates that the liquid tends to shrink away from the solid surface. Thus oxygen plasma treatment of the substrate is done before inkjet printing. This wets the surface and renders negative charge to it thus decreasing the contact angle of PEDOT:PSS drop with ITO substrate to less than 90° as shown in Figure 3.4.

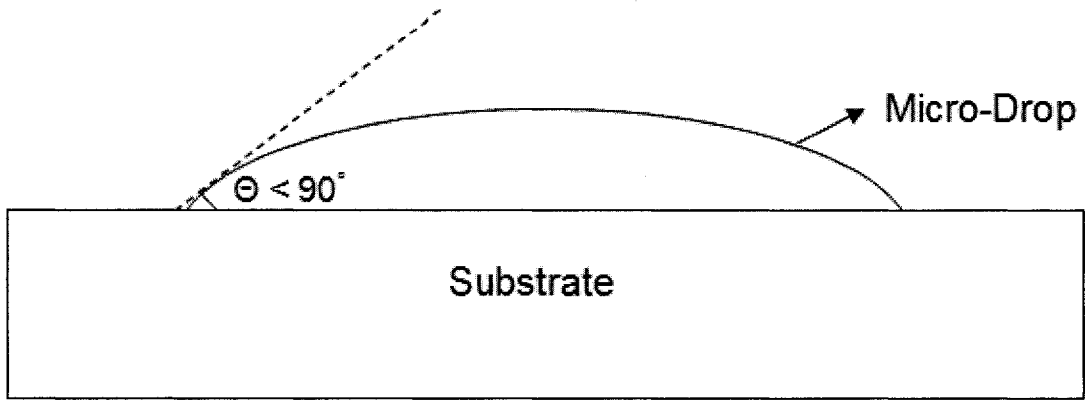

Figure 3.4 The contact angle between the substrate and micro-drop

If the influence of kinetic energy of the drop is negligible, then the drop will spread due to capillarity to its equilibrium contact angle. Thus the spreading factor is only a function of contact.

Surface tension: This is an internal force, due to an imbalance in molecular forces that occurs at the interface when liquid drop comes in contact with substrate. The force is due to the tendency of all materials to reduce their surface area in response to the imbalance in molecular forces that occurs at their points of contact. The result of this force dictates the wettability and contact angle between the drop and substrate.

The temperature of the substrate was increased to 70°C because surface tension decreases with temperature. Thus the solute particles tend to move away from each other and therefore increase the deposition at the periphery of the drop.

Velocity of drops: Drops leaving the nozzle are bound by a minimum velocity because a minimum pressure is required to overcome the pressure developed by surface tension at the nozzle given by P_n [110].

$$P_n \approx \frac{2\sigma}{R}, \tag{3.5}$$

where R is the radius of the nozzle and σ is the surface tension of the liquid.

The pressure to overcome surface tension is generated by the inertia of the liquid drops given by

$$P_n \approx \rho_l V^2, \tag{3.6}$$

where ρ_l is the density of the liquid and V is the velocity of the drop.

The typical minimum velocity of the drops as they leave the nozzle can be obtained by equating the above two equations

$$V_{\min} \approx \sqrt{\frac{2\sigma}{\rho R}} \tag{3.7}$$

3.4 Drop Dispensing

The two drop dispensing techniques used for varying the diameter and height of the micro-rings are named as "instant dispensing" and "dispense and dry" respectively. The flow chart in Figure 3.5 represents both techniques for fabricating micro-rings of varying dimensions for various applications.

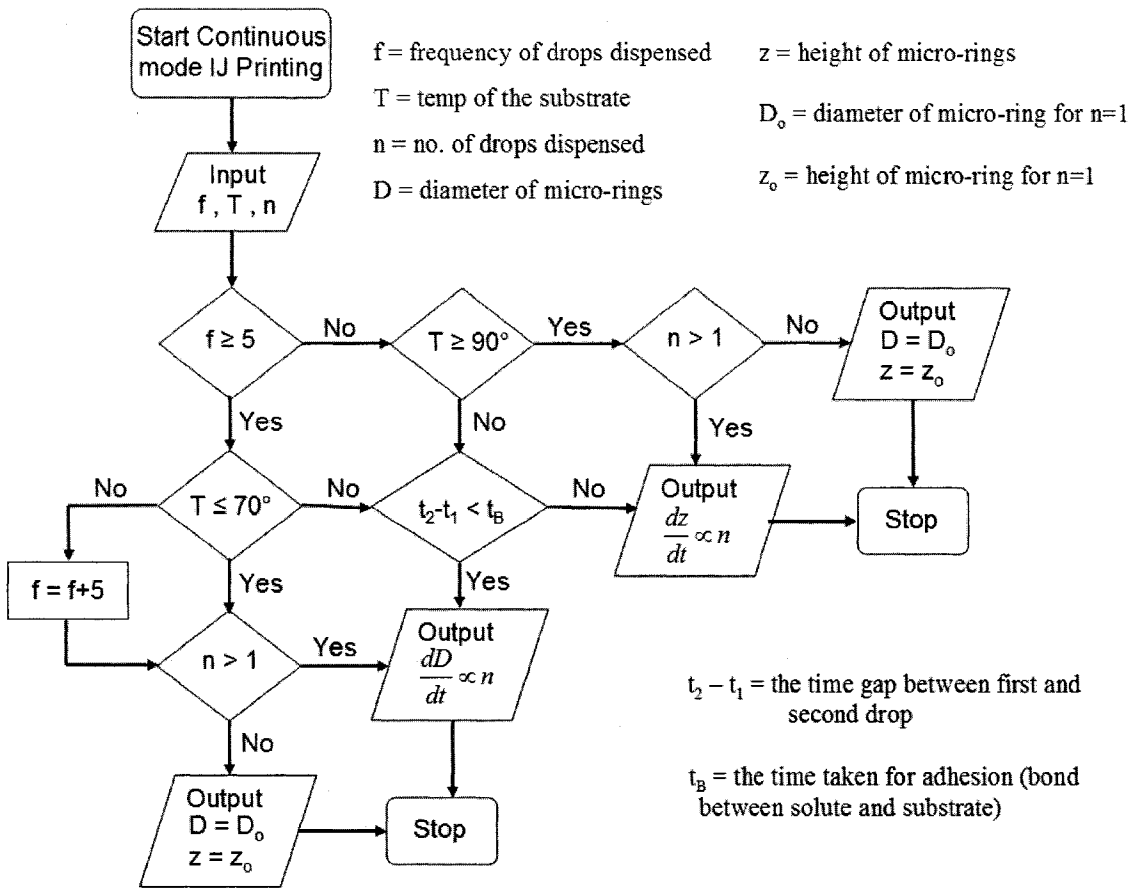

Figure 3.5 Flow chart for inkjet printing of rings with varying diameter and height

There are two modes of printing in the Autodrop inkjet printer i.e. continuous mode and burst mode. In the continuous mode, both frequency and number of the drops dispensed can be varied, whereas in the burst mode only number of drops dispensed can be varied. Thus we use continuous mode inkjet printing. The parameters to be varied are frequency of drops dispensed (f), temperature of the substrate (T) and number of drops dispensed (n) as shown in Figure 3.6.

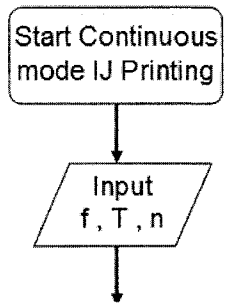

Figure 3.6 Continuous mode and parameter varied for IJ printing

The frequency of the drops dispensed can be varied from 1 to 2048 drops/sec. Initial assumption for frequency of drops is taken to be 5. If frequency of drops is more than 5, then we have to see if substrate temperature is less than of equal to 70°C. If frequency of drops is less than 5, then we have to consider if the temperature of the substrate is greater than or equal to 90°C as shown in Figure 3.7.

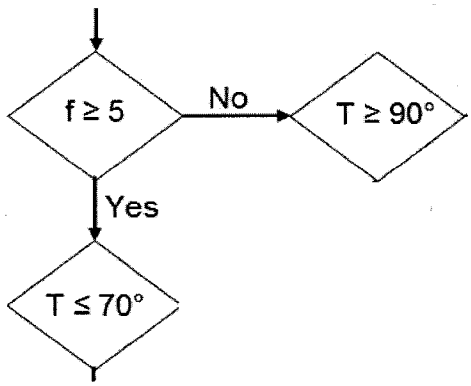

Figure 3.7 Frequency and substrate temperature parameters

If temperature of substrate is less than or equal to 70° C and number of drops dispensed is greater than one, then the diameter of the micro-ring is proportional to number of drops dispensed i.e. $\frac{dD}{dt} \propto n$ as shown in Figure 3.8. Thus we go in accordance with "instant dispensing" technique.

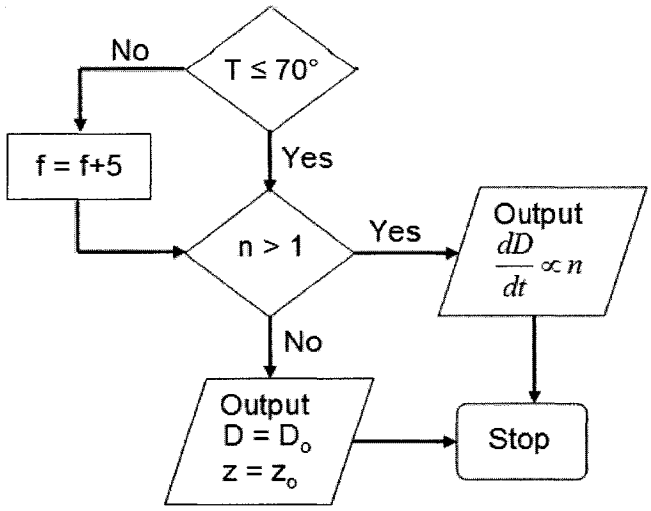

Figure 3.8 Flow chart for "instant dispensing" technique

From Figure 3.7, if frequency of drops is less than 5, then we have to consider if temperature of substrate is greater than or equal to 90°C. If yes, and number of drops dispensed are greater than one, then the height of the micro-ring is proportional to the number of drops dispensed i.e. $\frac{dz}{dt} \propto n$ as shown in Figure 3.9. Thus we follow "dispense and dry technique."

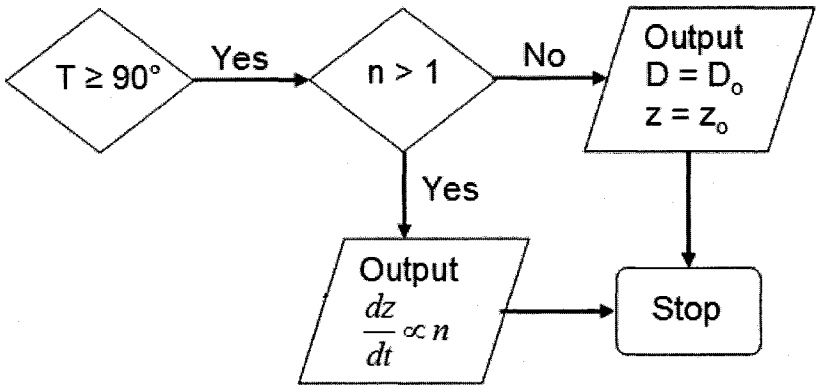

Figure 3.9 Flow chart for "dispense and dry" technique

In Figure 3.7 and Figure 3.8, if number of drops dispensed in equal to one, then the diameter and height of the micro-ring remains same irrespective of the dispensing technique.

Time of adhesion (t_B) is one of the factors mentioned in flow chart in Figure 3.10 which can vary the ring formation to either diameter change or height change.

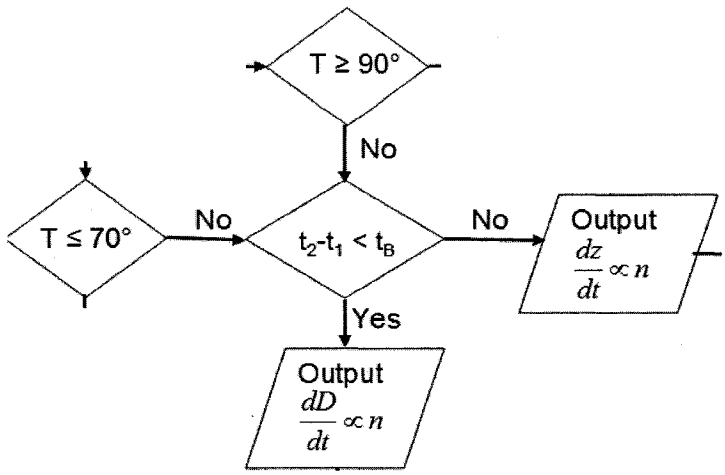

Figure 3.10 Flow chart for time of adhesion

We know that the adhesion of the polymer material to the surface is very strong once the bonds are formed. Thus, the dispensing parameters have to be varied in such a way that the frequency of the drops dispensed is more than the time taken to form a bond in "instant dispensing" technique and is vice versa in "dispense and dry" technique. Let

$t_2 - t_1$ = the time gap between first and second drop,

t_B = the time taken for adhesion (bond between solute and substrate)

Thus varying diameters can be obtained by using instant dispensing technique i.e.

$$t_2 - t_1 < t_B \quad \text{and} \tag{3.8}$$

varying thickness/height can be obtained by using dispense and dry technique i.e.

$$t_2 - t_1 > t_B \tag{3.9}$$

Instant dispensing: With the same printer head nozzle size, the diameters of the micro-rings in a range of 100 μm to 500 μm have been fabricated using the technique named "instant dispensing." The optical images are obtained using high resolution OLYMPUS Vanox AHMT3 optical microscope. The varying diameter of the micro-rings using "instant dispensing" technique is shown in Figure 3.11.

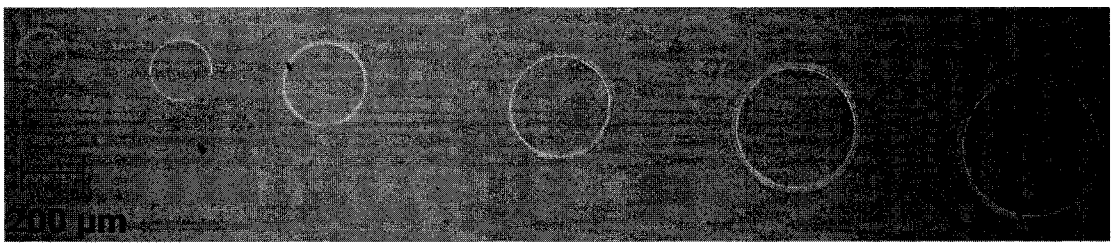

Figure 3.11 Varying diameter of the micro-rings using "instant dispensing"

Using this technique the diameter of the micro-rings can be varied without significant change in the height of the micro-ring. The substrate temperature was set to 70°C in order to maximize the polymer deposition at the edges of the drop. The frequency of the drops (f) dispensed was set to more than 5 drops per second. If the substrate temperature (T) is higher, then the frequency of the drops can be increased in order to change the diameter (D) of the rings. The number of drops dispensed (n) are further varied in order to get varying diameters. Thus the rate of change of diameter is proportional to the number of drops dispensed ($\frac{dD}{dt} \propto n$).

Dispense and dry: The second drop dispensing technique is the "dispense and dry" which allows each drop to dry for about 1 second using the substrate temperature of 90°C or above before dispensing another drop on top of it. The first drop fixes its boundary and forms a strong bond with the surface and the second drop carries its solute

to the boundary of the first drop and accumulates the solute on top of the ring, thus increasing the height (z) of the drop. In this case, the diameter shows negligible change. Thus, rate of change of height is proportional to the number of drops dispensed ($\frac{dz}{dt} \propto n$).

The optical microscopic image of 1, 2, 5, 10, 20 and 30 drops dispensed by second technique is shown in Figure 3.12.

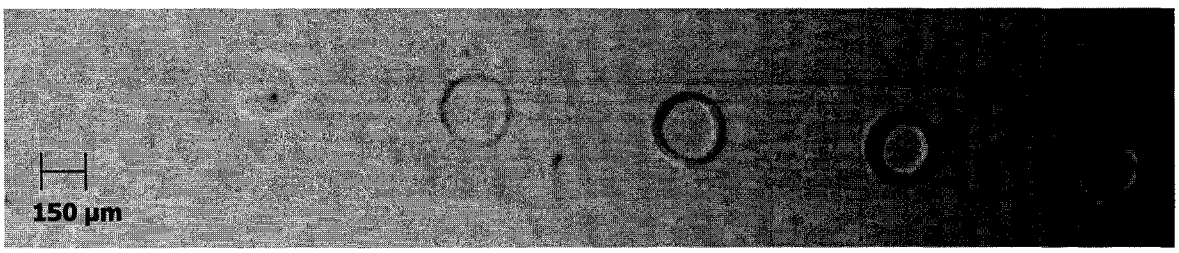

Figure 3.12 Optical image of micro-rings using "dispense and dry" technique

The experimental values of diameter and height of micro-rings for both the dispensing techniques as measured by surface profilometer, are shown in Table 3.1.

Table 3.1 Variation in diameter and height of micro-rings before and after plasma etching using both techniques

No. of drops (n)	**Instant Dispensing Technique**			**Dispense and Dry Technique**		
	Diameter (µm)	Height (nm)		Diameter (µm)	Height (nm)	
		Before RIE	After RIE		Before RIE	After RIE
1	170	102	70	150	105	72
2	254	147	84	151	215	151
5	305	207	145	163	820	775
10	351	255	165	149	1980	1885
20	428	349	295	151	5714	4708
30	480	379	319	147	9755	8813

Figure 3.13 shows a plot of varying diameter and height of micro-rings.

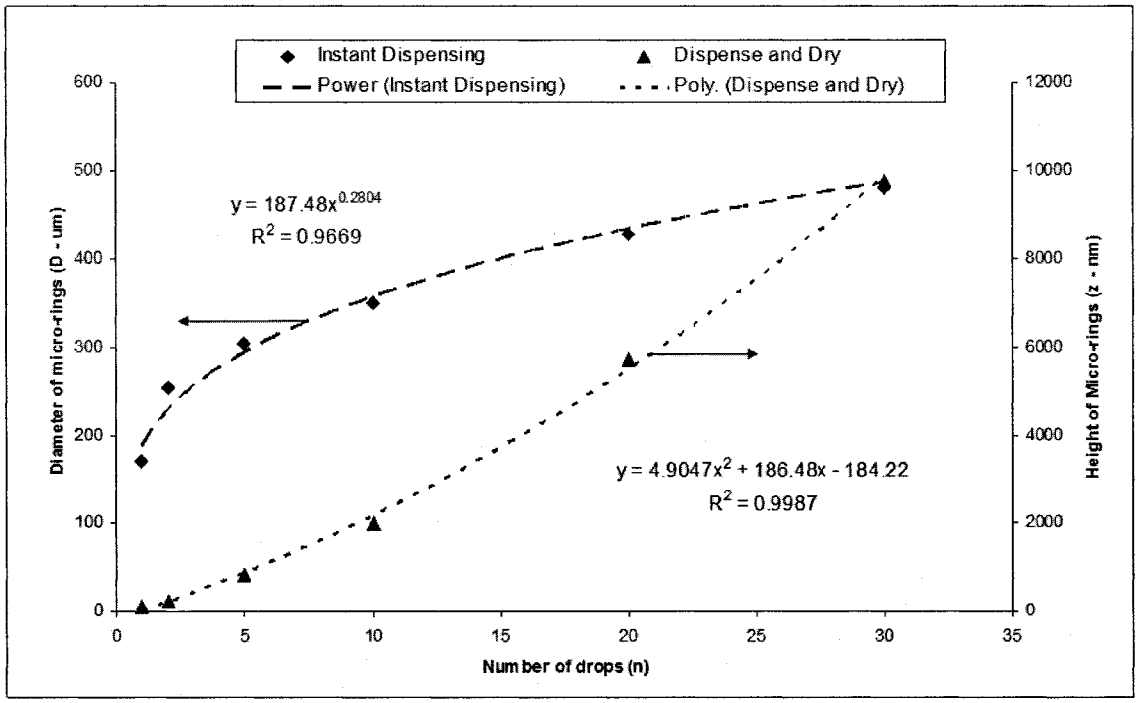

Figure 3.13 Diameter and height variation of micro-rings Vs number of IJ printed drops

The curve fitting was done for both the dispensing techniques. The rate of change of diameter (D) of micro-rings with increasing number of drops (n) fits in accordance with power equation as

$$D = 187.48n^{0.2804} \tag{3.8}$$

and $R^2 = 0.9669$, which is close to one, representing a good fit.

The rate of change of height (z) of micro-rings with increasing number of drops (n) fits in accordance with second order polynomial equation as

$$z = 4.9047n^2 + 186.48n - 184.22 \tag{3.9}$$

and $R^2 = 0.9987$, which is very close to one, representing a good fit.

Thus using the empirical analysis we can predict the diameter and height of micro-ring for "instant dispensing" and "dispense and dry" techniques respectively.

CHAPTER 4

LAYER-BY-LAYER (LbL) NANOARCHI – TECTURE OF PEDOT-PSS AND PPy ULTRATHIN FILMS

4.1 Overview

LbL self-assembly is a unique method for the fabrication of composite films with nanometer precision and has rekindled widespread interest in the field of nanotechnology. The attractive feature of this approach is its ability to assemble complex structures from modular components and integrate them into self-assembling constructions for a wide range of applications. In this technique, a charged substrate is exposed alternately to dilute aqueous solutions of oppositely charges polycations and polyanions that enables electrostatically driven deposition of these polyelectrolytes as thin films of controlled thickness and composition.

Rubner and co-workers developed this technique for controlled deposition of doped conducting polymers. Self-assembly of PEDOT-PSS, PPy and PANI with non-conducting polyionic species has been reported for microelectronic devices as well as electrochromic devices.

We fabricated nano-organized architecture of alternate films of two p-type doped conducting polymers PEDOT-PSS and PPy via LbL. Here, PEDOT-PSS and PPy act as

polyanion and polycation respectively to form the gradient. The formation of this gradient facilitates controlled carrier hopping.

4.2 LbL Nanoassembly of Conducting Polymers

The assembly was done on Pyrex® glass slides that were treated with cleansing solution which renders the glass surface negatively charged. The assembly was initiated by dipping glass slides in one type of conducting polymer solution for 10 minutes followed by rinsing in DI water for 30 seconds and then drying in nitrogen. This was followed by dipping the same glass slide in other type of conducting polymer and so on till you get the desired number of bilayers. Initially experiments were done to observe the self-assembly of various conducting polymers such as, PEDOT-PSS, PPy and PANI with each other.

Silver quartz crystal microbalance (QCM) resonators (10 MHz resonant frequency) were used as substrates for depositing of 5 precursor bilayers of PSS/PAH followed by 5 alternating bilayers of PANI/PPy, PEDOT-PSS(X)/PANI and PEDOT-PSS/PPy via layer-by-layer (LbL). PSS (Mw 70,000) and PAH (Mw 70,000) were purchased from Aldrich. PSS acts as the polycation and PAH as polyanion in the alternate LbL self-assembly process. Five alternate layers of $(PSS/PAH)_5$ act as the precursor layer to the subsequent alternating layers of conducting polymers. Change in the resonant frequency was observed using the QCM and the Sauerbrey equation was used to correlate change in frequency to the mass deposited and thickness of the self-assembled films.

Figure 4.1 shows the mass deposited on resonator with increasing number of bilayers.

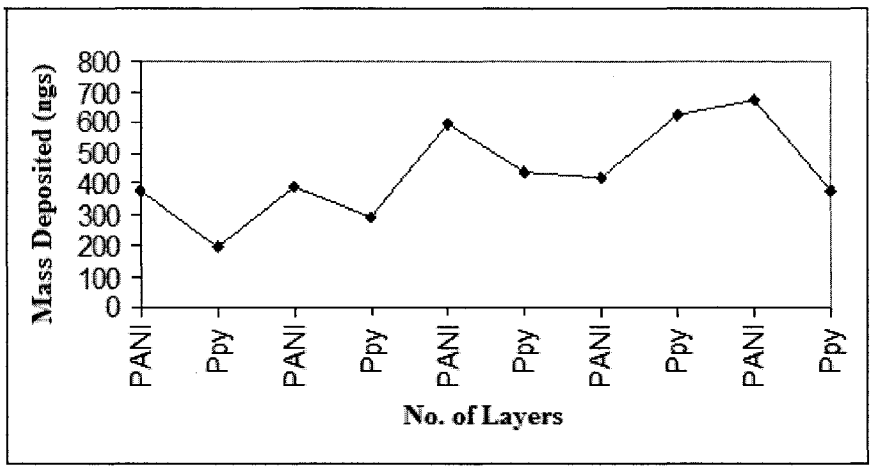

Figure 4.1 Mass deposited for $(PANI/PPy)_5$ bilayers

From this figure, it can be inferred that there has been no self-assembly of PANI and PPy as the mass deposited after each bilayer does not change. Similarly as shown in Figure 4.2, there is no mass deposition on the resonator thus no assembly is taking place.

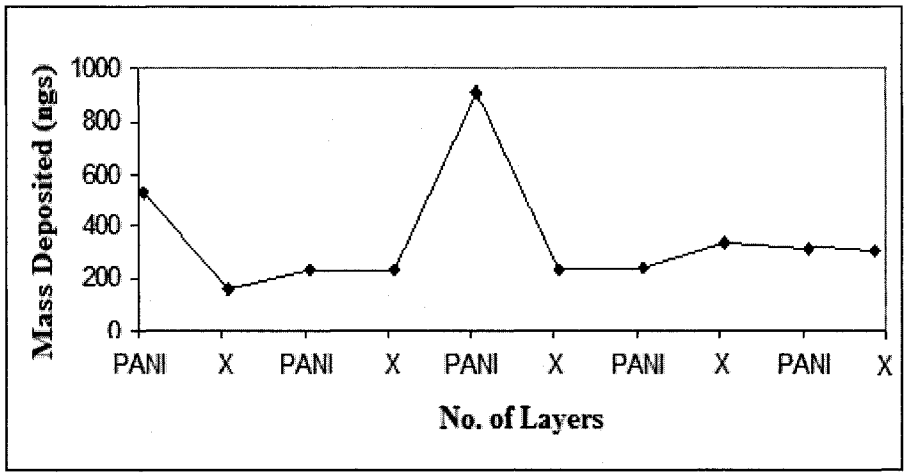

Figure 4.2 Mass deposited for $(PANI/PEDOT\text{-}PSS(X))_5$ bilayers

The layer-by-layer electrostatic assembly of anionic PEDOT-PSS and cationic PPy is based on the saturated adsorption of monolayers of these polymers in their conductive forms on a substrate surface. Samples coated with multiple layers of

alternating films of 10 bilayers of $(PEDOT\text{-}PSS/PPy)_{10}$ exhibited "super-assembly" when they were prepared at room temperature as shown in Figure 4.3. The overall increase in mass of materials deposited on the resonator shows the electrostatic assembly of these conducting polymers.

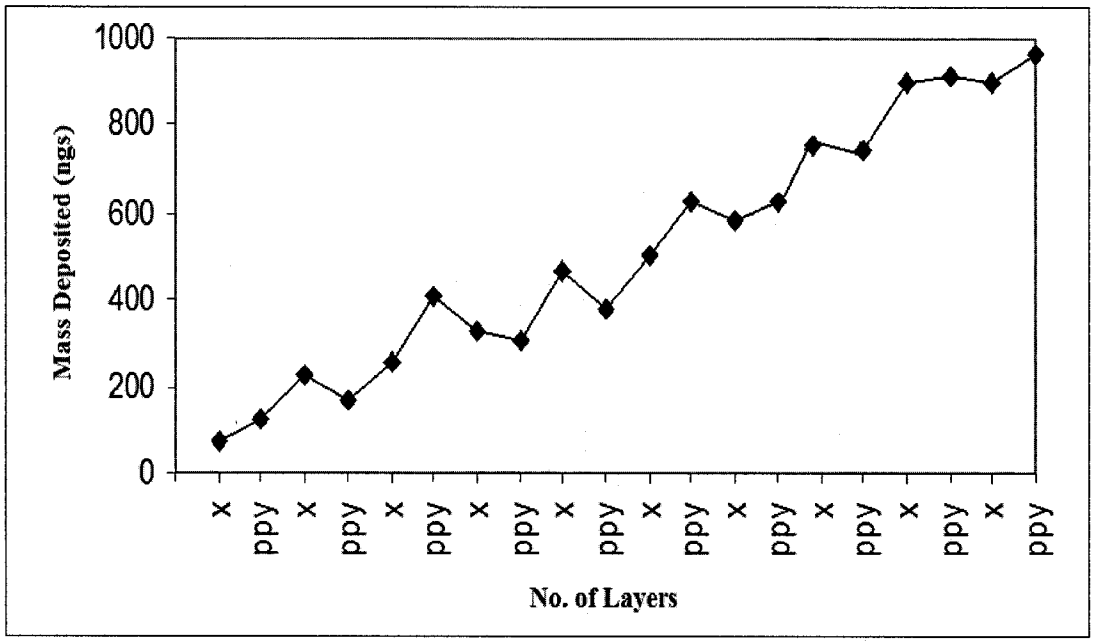

Figure 4.3 Mass deposited for $(PEDOT\text{-}PSS/PPy)_{10}$ bilayers

Using the extension of Sauerbrey equation, thicknesses of the deposited layers were calculated. Figure 4.4 shows the change in thickness with deposition of each layer of the conducting polymer. A typical step of the film growth was 1.8±0.1 nm for every other bilayer. The overall thickness of 10 bilayers is around 18 nm.

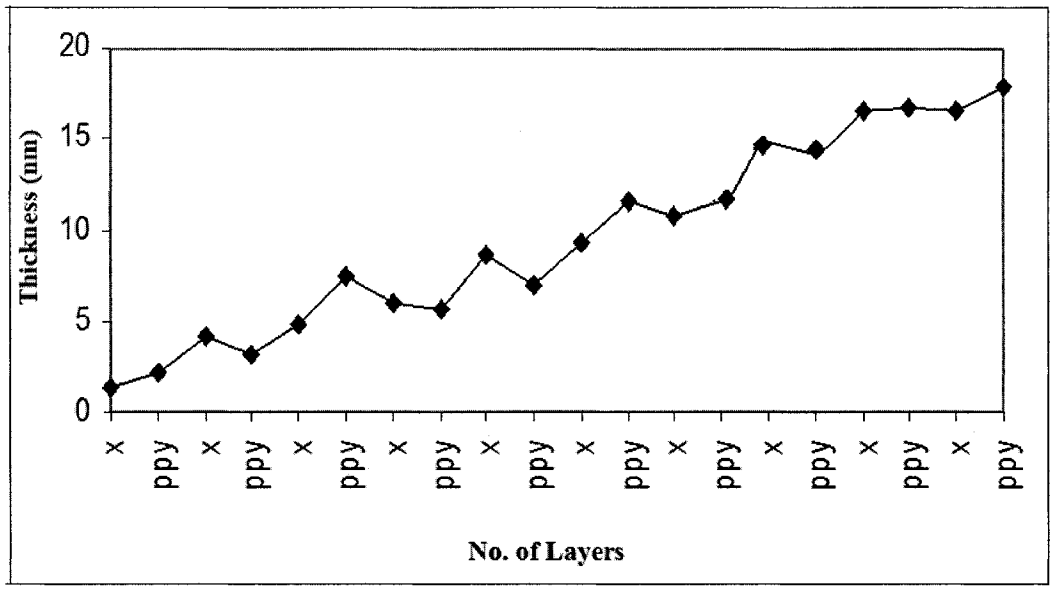

Figure 4.4 Change in thickness with increasing self-assembled layers

Further, the dependency of the thickness as a function of dipping time for the deposited PEDOT-PSS and PPy layer was studied in order to get maximum deposition of each layer in the least amount of time possible. The LbL assembly was done on three different samples with dipping time of 5, 10 and 15 min. Figure 4.5 shows the change in thickness with assembly for three dipping time periods. From the figure, we conclude that the deposition is not time dependent, and so further assembly for all the devices was carried out with a dipping time of 5 min.

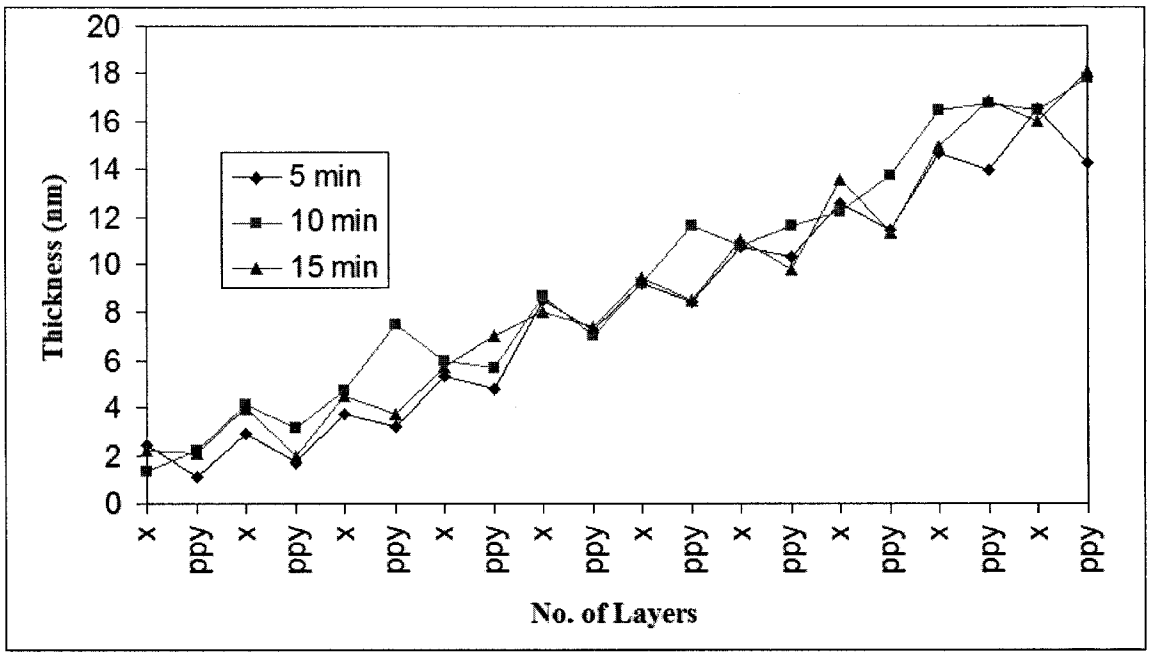

Figure 4.5 Time dependency on self-assembly of $(PEDOT\text{-}PSS/PPy)_{10}$

The LbL assembled thin film of PEDOT-PSS/PPy was characterized for electrical conductivity. The current-voltage curve for 10 bilayers of PEDOT-PSS/PPy on a glass substrate is shown in Figure 4.6.

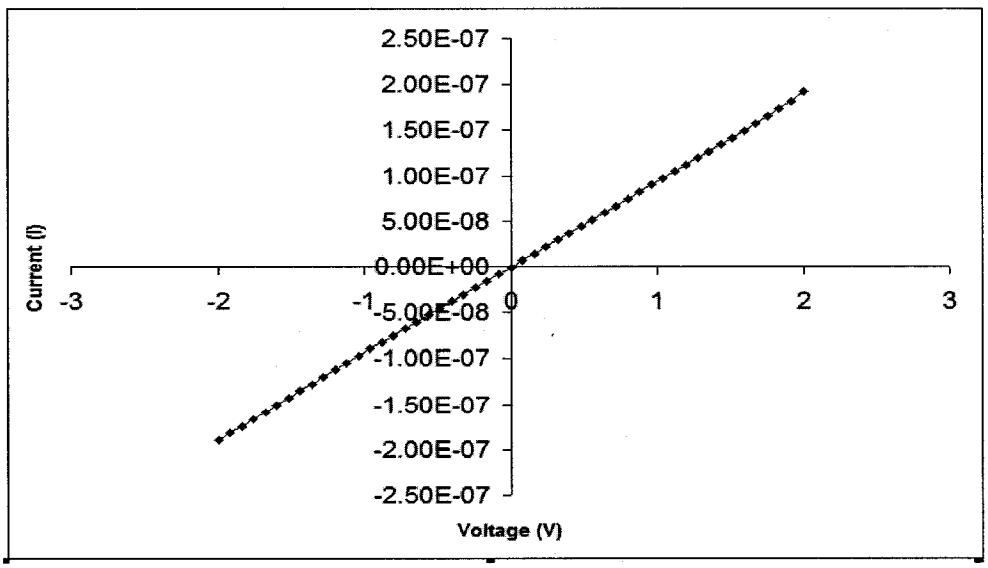

Figure 4.6 Current-voltage characteristics of $(PEDOT\text{-}PSS/PPy)_{10}$

The alternating LbL assembled 10 bilayers of two p-type conducting polymers PEDOT-PSS and PPy gave a conductivity of 0.04 S/cm.

4.3 Annealing Effect on LbL Assembled Layers

In order to study the effect of annealing on the assembly and conductivity of PEDOT-PSS/PPy thin film, we introduced a step of annealing the sample after deposition of every monolayer. Figure 4.7 shows the QCM results for thickness variation with deposition of each monolayer at room temperature and at different annealing temperatures. Samples coated with multiple layers of alternating films of these p-type doped conducting polymers exhibited "super-assembly", when they were prepared at room temperature without annealing. However, linear growth was observed when the samples were annealed above room temperature after deposition of each monolayer. The best linear growth was shown by samples annealed at 120°C.

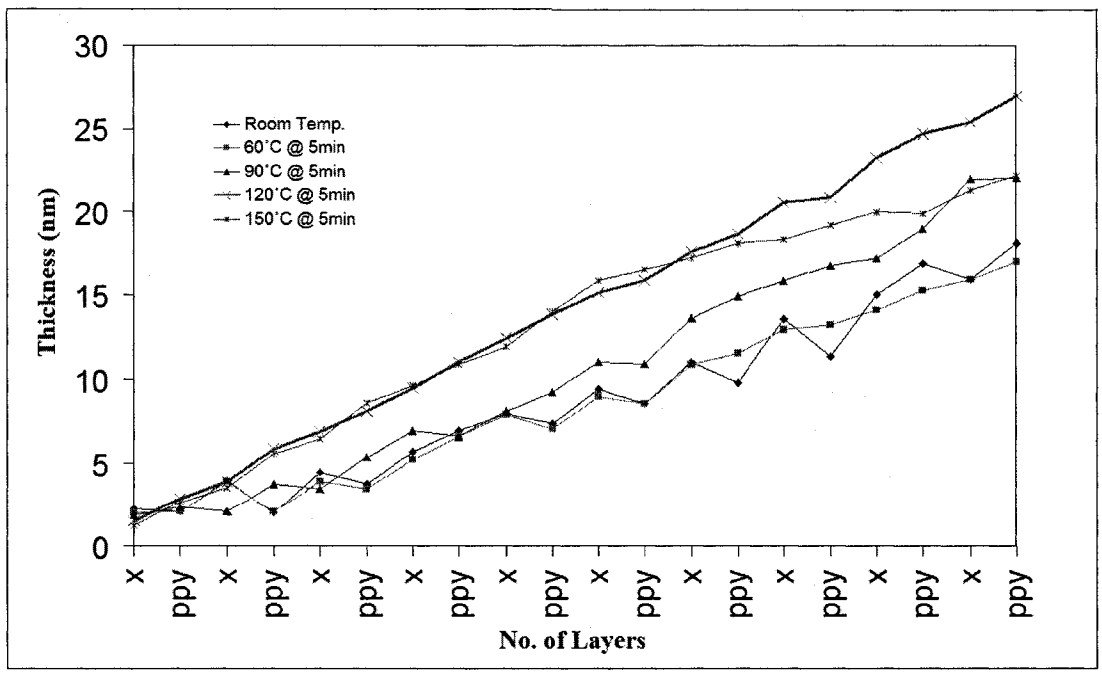

Figure 4.7 Effect of annealing at various temperatures on thickness and assembly

A typical step of the film growth was 2.3±0.1 nm for every other bilayer. Therefore, we could prepare polymer layers with the thickness proportional to this value (for example, a 10-bilayer film with a thickness of 23 nm). Figure 4.8 shows uv-vis absorbance spectra for deposited nano-assembled films at room temperature and at 120°C.

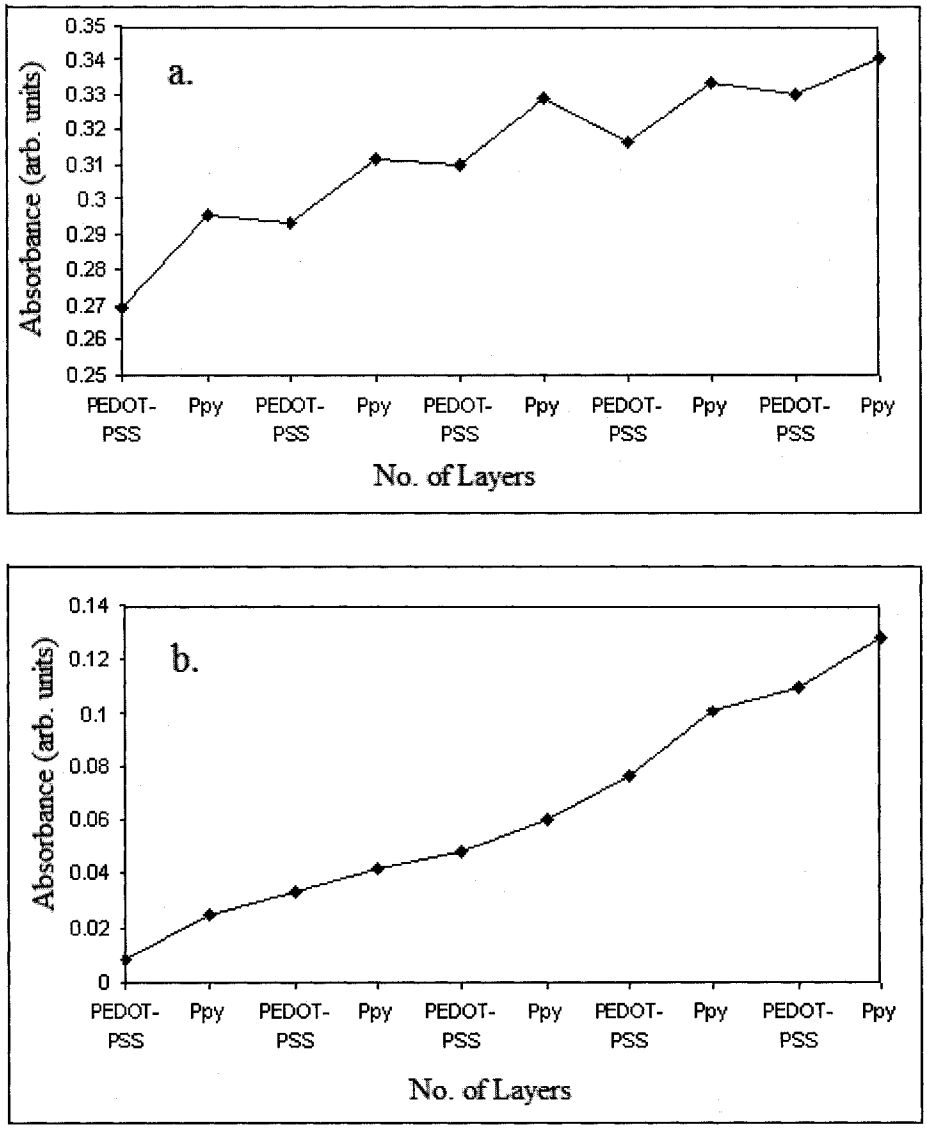

Figure 4.8 UV-Vis absorbance spectra for nano-assembled films at (a) room temp and (b) at 120°C

In some cases, after deposition of one of the charged species, there appears to be decrease in the thickness followed by an increase after the deposition of the next layer. This is due to the removal of non-specifically adsorbed excess material. Figure 4.9 shows the AFM image of the LbL assembled PEDOT-PSS/PPy film. The bigger spots in the AFM image are the adsorbed material in excess amount. The overall thickness of the film continues to increase, however.

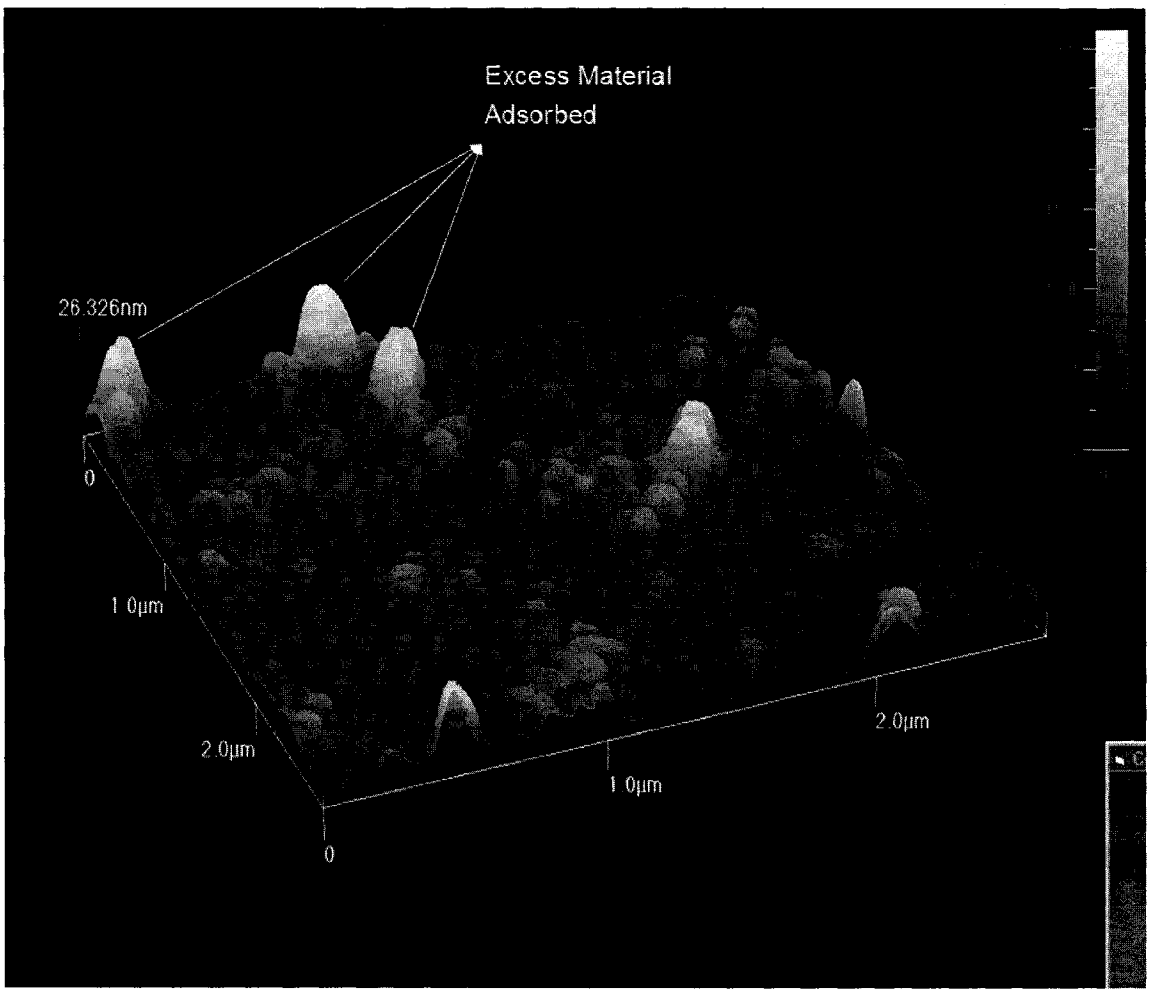

Figure 4.9 AFM image of LbL deposited PEDOT-PSS/PPy bilayers

Figure 4.10 shows the current – voltage characteristics of the annealed samples of 23 nm thick $(PEDOT\text{-}PSS/PPy)_{10}$ bilayers using van der Pauw four probe method.

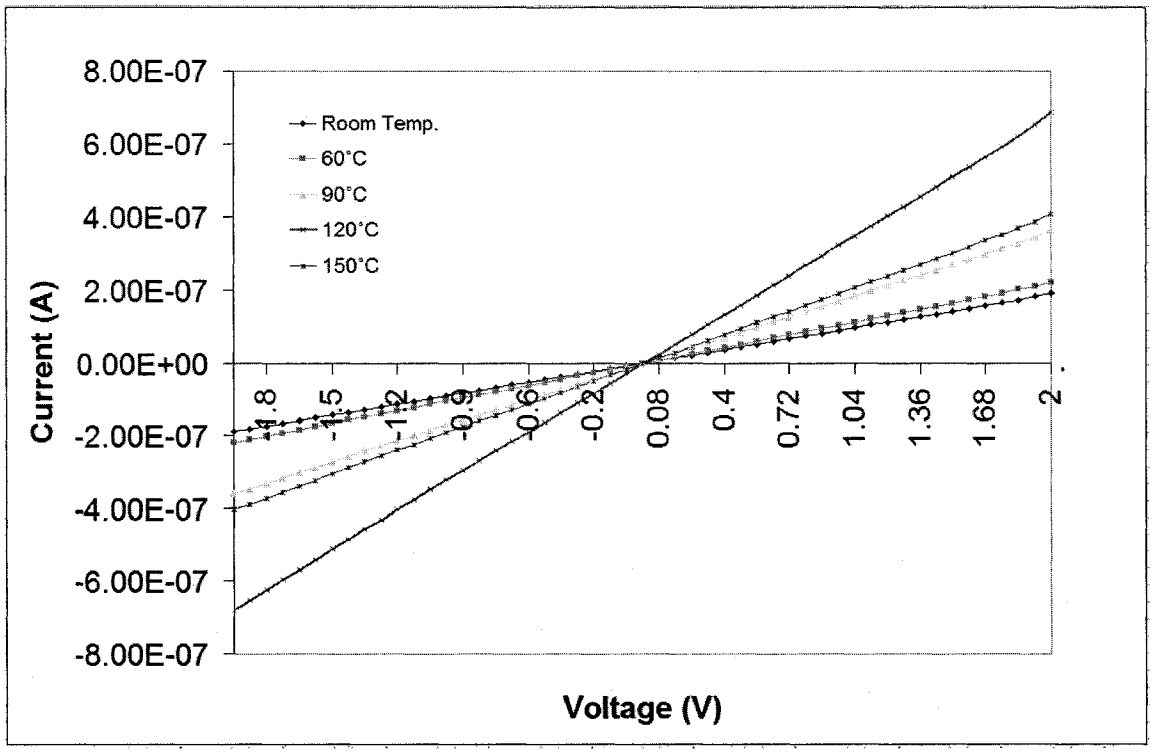

Figure 4.10 Current-voltage characteristics of PEDOT-PSS/PPy LbL assembled films at various annealing temperatures

Enhanced conductivities (Figure 4.11) of the alternately deposited bilayers of $(PEDOT\text{-}PSS/PPy)_{10}$ were observed as the annealing temperature was raised from room temperature to 120°C. This can be attributed to the observed behavior of disordered semiconductors. The conductivities obtained range from 0.037 S/cm at room temperature to 0.13 S/cm at 120°C. This increase in conductivity is attributed to the less scattering of holes in nano-assembled monolayer of p-type doped conducting polymer. Due to annealing the self-assembled layer or the chains of both polymers are so closely packed that inter-chain hopping between the two polymers increases.

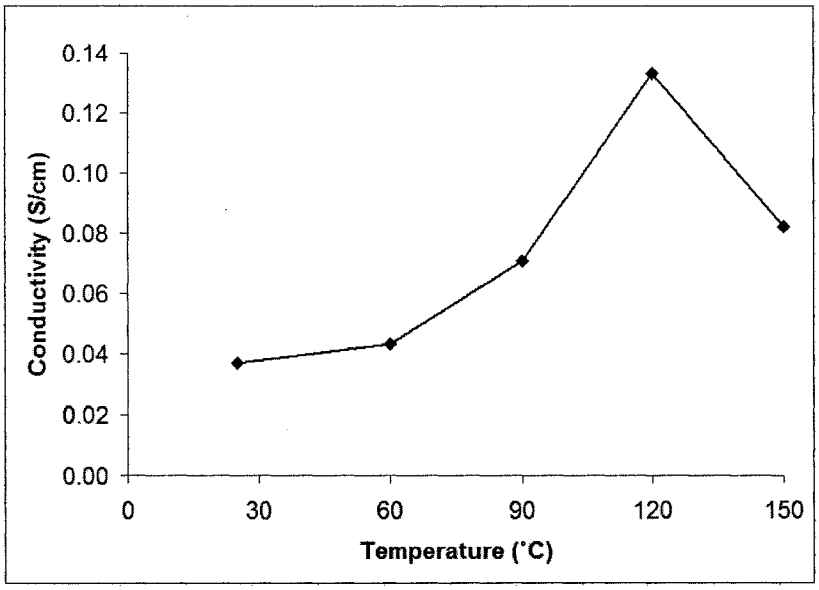

Figure 4.11 Conductivity variation with changing annealing temperature

A mechanism which explains the variation of bulk conductivity in conductive polymers with change in temperature is by proposing a model of several concentrated highly conducting charged regions in a sea of less conducting amorphous material. It has been reported that by decreasing temperature from 500°K to 0°K, the conductivity of certain conductive polymers decreases [111]. The electrical conductivity of disordered semiconductors follows a linear relationship with change in temperature. However, the range of temperature depends on the degradation of the conductive polymer. This temperature constitutes the limiting threshold for the increase of conductivity with increase in temperature. If the temperature is increased beyond this threshold, the conductive polymer may "degrade" causing partial or complete oxidation that could result in non-conducting oxides and/or carbon residues. In our case, PPy reaches its boiling point at 100°C. Therefore, raising the annealing temperature above 120°C, causes the degradation of PPy films resulting in non-conducting residues that deteriorate the overall conductivity of the PEDOT-PSS/PPy architecture.

CHAPTER 5

FABRICATION AND CHARACTERIZATION OF POLYMERIC MICRO-RINGS AND THEIR APPLICATIONS

5.1 Overview

Inkjet printing is considered to be one of the major techniques for soluble polymer deposition. At the boundary of inkjet printed dot there is a formation of ring. This is caused by pinned contact line that pulls the liquid outwards to compensate for evaporation loses. This phenomenon is known as "coffee drop effect." We have exploited this effect for directly printing polymer micro-rings. The drop dispensing rate, substrate temperature and reactive ion etching have been optimized for the fabrication of micro-rings with different height and diameter for several applications. Autodrop platform from Microdrop is used for drop-on-demand inkjet printing of soluble polymers. A printer head with a 70μm diameter nozzle was used for inkjet printing of polymer micro-rings. The ink solution is PEDOT-PSS was purchased from Bayer Inc.

The surface topography of the micro-rings have been analyzed with the help of scanning electron microscopy and atomic force microscopy. The micro-ring profile was studied by stylus alpha step profilometer. The presence of completely hollow micro-rings was observed under confocal microscope using layer-by-layer assembled red dye TRITC.

With the same printer head nozzle size, the diameters of the micro-rings in a range of 100 μm to 500 μm have been fabricated by using "instant dispensing" technique. Micro-rings with heights of 0.1 μm to 10 μm have been fabricated, while keeping the diameter of the micro-rings constant by "dispense and dry" technique.

Further we demonstrate the application of micro-rings for polymer based light emitting diodes, humidity sensor and vertical field effect transistor. These micro-rings were employed for the fabrication of high resolution polymer light emitting diodes. Each micro-ring was considered as an individual light emitting pixel. The current – voltage characterization of polymer light emitting diode was done using Keithley electric probe station. The resolution of polymer light emitting diode can be further enhanced by using inkjet printing of compact micro-rings.

An array of inkjet printed micro-rings was used as a platform for layer-by-layer nanoassembly of PEDOT-PSS. High sensitivity humidity sensors of PEDOT-PSS were fabricated by this technique. For every 5% increase in humidity 6%, 9% and 12% decrease in resistance was observed for the devices fabricated by inkjet printing, layer-by-layer and layer-by-layer over inkjet printed micro-rings, respectively. The high sensitivity is attributed to the ultra-thin film with a large sensing area for the layer-by-layer over inkjet printed polymer humidity sensors. The characterization of the devices were done using Keithley probe station and attenuated total reflection infra-red spectroscopy.

Highly conductive PEDOT-PSS was inkjet printed in the form of partially overlapping micro-rings to be used as source for FET. The central portion that was not overlapped was exposed to SF_6 plasma to etch the SiO_2 and expose the ITO below.

PEDOT-PSS acts as mask for the S/D insulation which consists of self-assembled layers of SiO_2 nanoparticles. MEH-PPV was spin coated, which comes in contact with ITO and PEDOT-PSS to act as channel for FET. Insulating layer of PVP of thickness 100 nm which acts as the gate dielectric was spin coated on top of MEH-PPV. Finally PEDOT-PSS was used for gate electrode. Initial experiments were performed on PEDOT-PSS gate for studying the effect of humidity on the output characteristics of the device. The current – voltage characterization of polymer vertical field effect transistor was done using electrical probe station.

5.2 Drop-on-Demand Inkjet Printed Polymer Micro-rings

5.2.1 Fabrication and Characterization of Micro-rings

Drop-on-demand inkjet printing is a technology to deposit low viscous polymers and requires that the viscosity of the ink is between 3-15 mPa at operating conditions. Thus the ink solution of PEDOT-PSS (Bayer Inc.) was prepared by adding DI water to PEDOT-PSS. This ink was filtered through 0.45 μm filter before printing.

A print head with a 70μm diameter nozzle was used for inkjet printing of polymer micro-rings. The parts of the print head that were in contact with the liquid were teflon and glass, which makes it compatible for a wide range of solvents. Moreover cleaning and operating of the head also becomes easy. Oxygen plasma treatment and cleansing solution treatment was performed on the glass substrate to make the surface hydrophilic in order to make good adhesion between the polymer and glass substrate. Laser scanning confocal microscope was used in order to observe the micro-rings.

The plasma treated glass substrate was coated with a nano-layers of fluorescent red dye named Tetramethyl Rhodamine Iso-Thiocyanate (TRITC) using layer-by-layer nanoassembly. Four bilayers of TRITC and oppositely charged polyelectrolyte were deposited alternately on plasma treated glass substrate.

Drops of PEDOT-PSS were inkjet printed on top of the glass slide coated with red dye. Figure 5.1 shows the inkjet printed PEDOT-PSS drops on top of TRITC layers in red. It is observed that the outer periphery of the drop is thicker than the inside of the drop.

Figure 5.1 PEDOT-PSS drops inkjet printed on top of TRITC

In order to make micro-rings, the thin inner layer of the drop should be completely removed. Oxygen plasma reactive ion etching (RIE) of the above sample was done to get the perfect micro-rings. Due to RIE the layers of TRITC below the inner layer of drop also gets etched. So, the only place where TRITC is left is below the outer edge of the micro-ring. So under confocal microscope, this red fluorescent dye can be observed showing the perfect and completely hollow micro-rings (Figure 5.2).

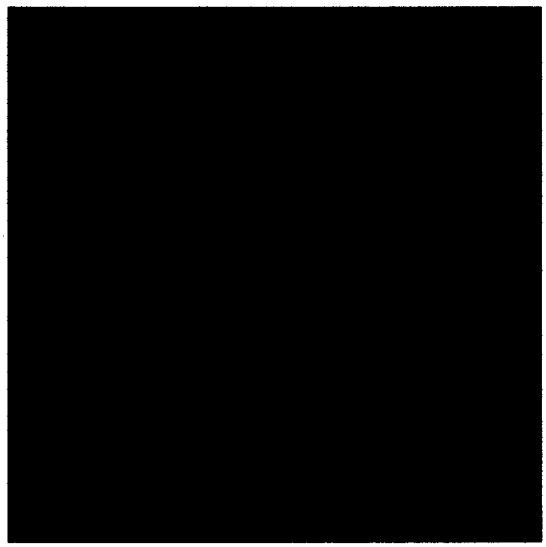

Figure 5.2 Hollow micro-ring depicted by TRITC

5.2.2 Drop Dispensing Techniques and Plasma Etching

With the same printer head nozzle size, the diameters of the micro-rings in a range of 100 μm to 500 μm have been fabricated using the "instant dispensing" technique. The micro-rings with heights in the range of 0.1 μm to 10 μm have been fabricated while keeping the same diameter of the micro-rings using the technique named "dispense and dry."

The optical images are obtained using high resolution OLYMPUS Vanox AHMT3 optical microscope. The varying diameter of the micro-rings using "instant dispensing" technique is shown in Figure 5.3. In this technique the number of drops to be dispensed together is specified. Using this technique the diameter of the micro-rings can be varied without significant change in the height of the micro-ring. The substrate temperature was set to 70°C in order to maximize the polymer deposition at the edges of the drop.

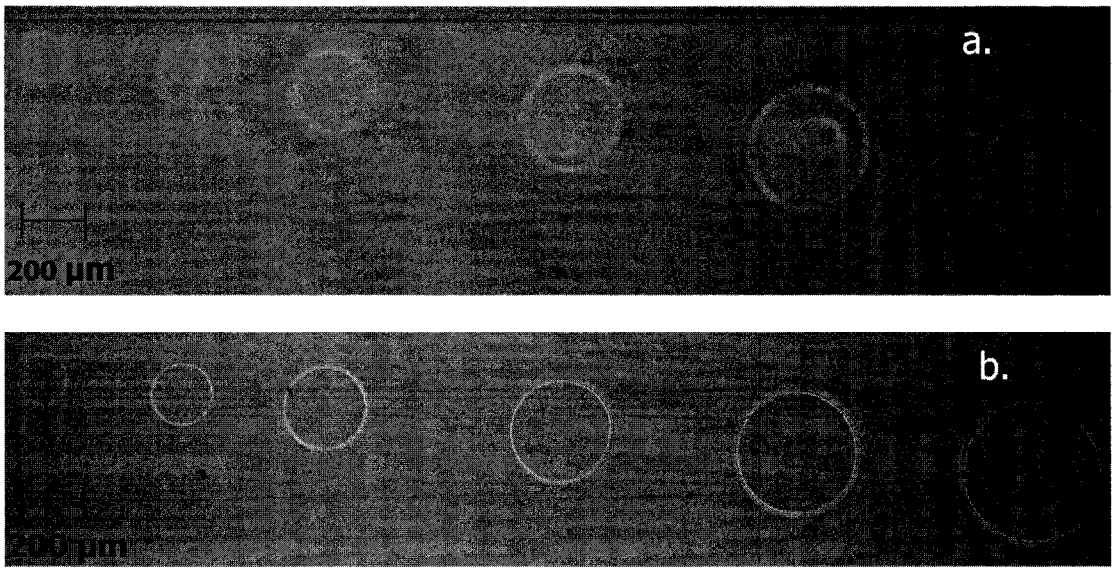

Figure 5.3 Varying diameter of the micro-rings using "instant dispensing" technique

Figure 5.3a and Figure 5.3b shows the optical image of 1, 2, 5, 10, 20 and 30 drops dispensed simultaneously before and after RIE. These micro-rings were further examined under scanning electron microscope (Figure 5.4).

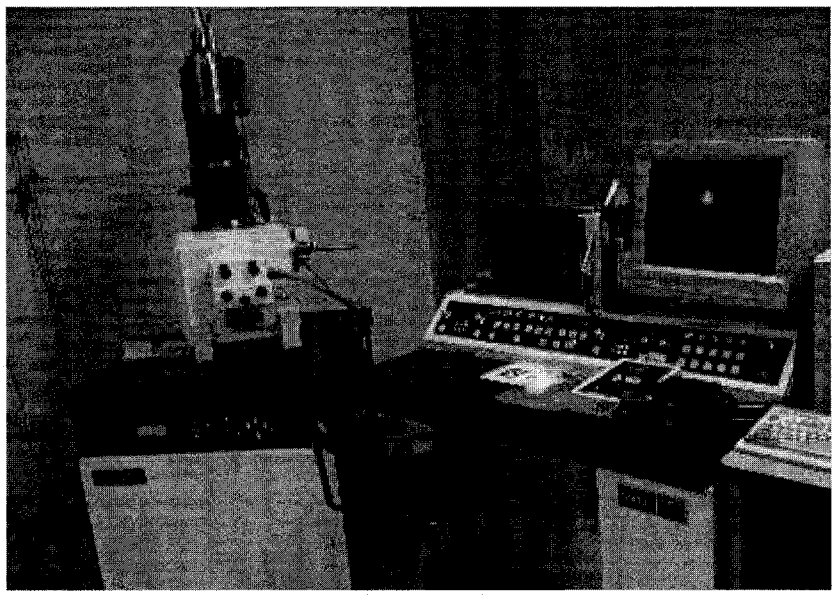

Figure 5.4 Scanning Electron Microscope at IfM

The SEM image of 10 drops dispensed after RIE are shown in Figure 5.5. These images depict that the micro-rings are completely hollow from inside.

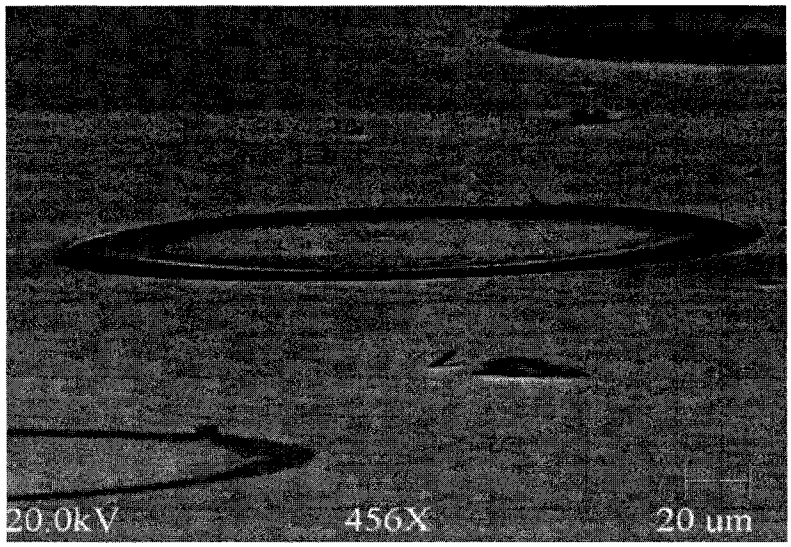

Figure 5.5 Ten drops after RIE

The Alpha-step surface profilometer was used to measure the micro-ring profile. The profile of 30 drops dispensed using this technique has been shown in Figure 5.6.

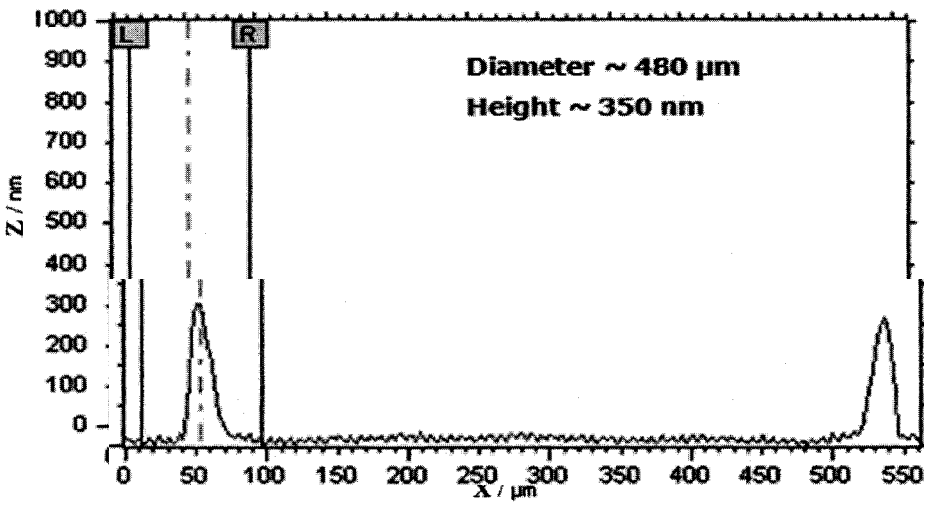

Figure 5.6 Step profile of micro-ring with diameter of 480 µm

The second drop dispensing technique "dispense and dry" allows each drop to dry for about 1 second using the substrate temperature before dispensing another drop on top of it. The first drop fixes its boundary and the second drop partially dissolves the first drop from the center and carries the solute from the middle to the edges. Thus every next drop that falls increases the thickness of the outer edge without diameter variation. Therefore by using RIE we have to just etch the thin inner layer (few nanometers) without altering the height of the micro-ring significantly. The optical microscopic image of 1,2,5,10,20 and 30 drops dispensed by second technique is shown in Figure 5.7.

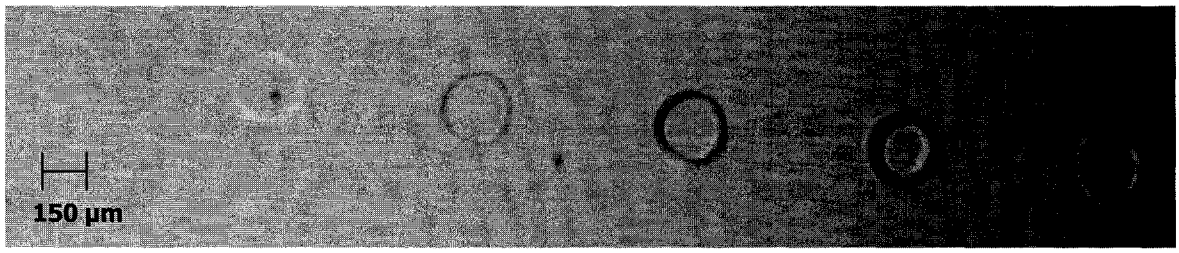

Figure 5.7 Optical microscope image of micro-rings fabricated using "dispense and dry" technique

The profile of 30 drops dispensed using the second technique is shown in Figure 5.8.

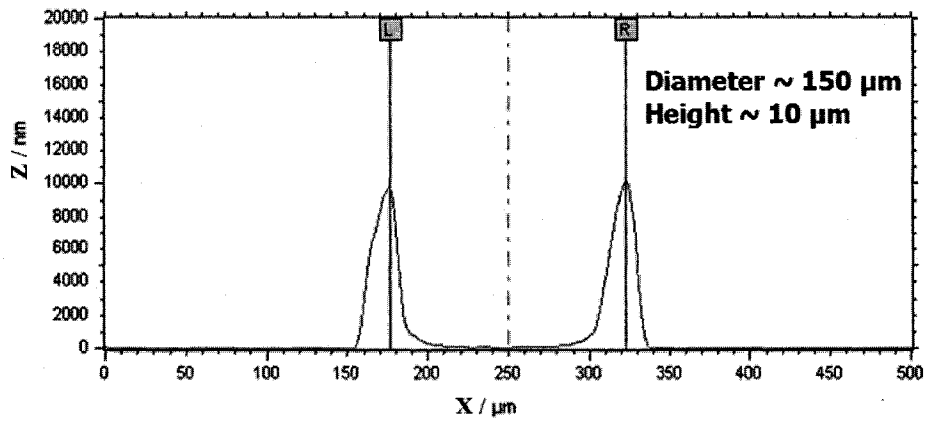

Figure 5.8 Step profile of micro-ring with height of 10 µm

Height of polymer micro-rings versus number of inkjet printed drops for both the techniques before and after plasma etching has been shown in Figure 5.9.

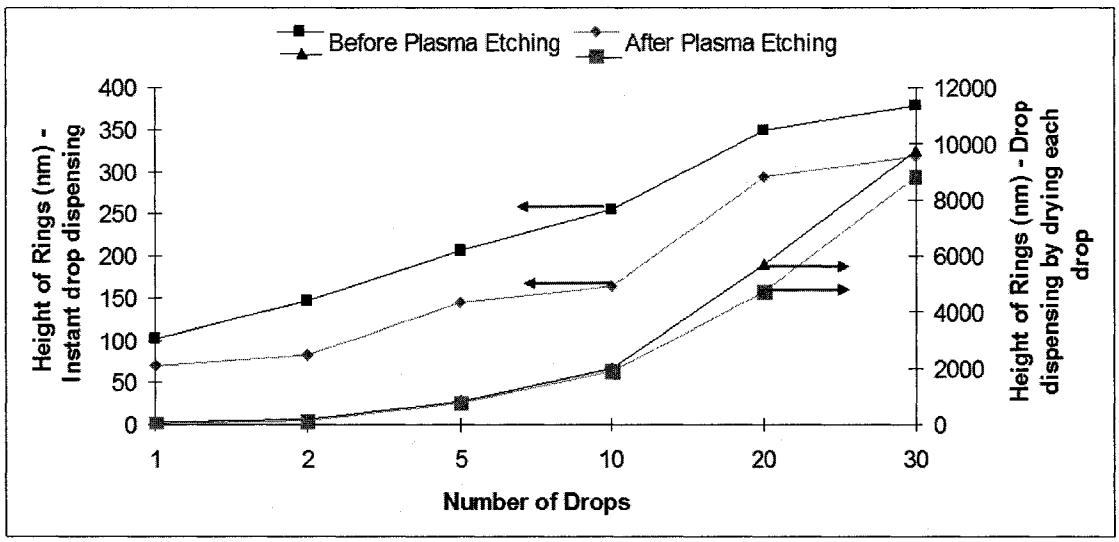

Figure 5.9 Height of micro-rings Vs number of IJ printed drops

The variation in diameter and height of the micro-rings for both techniques after plasma etching is shown in Figure 5.10.

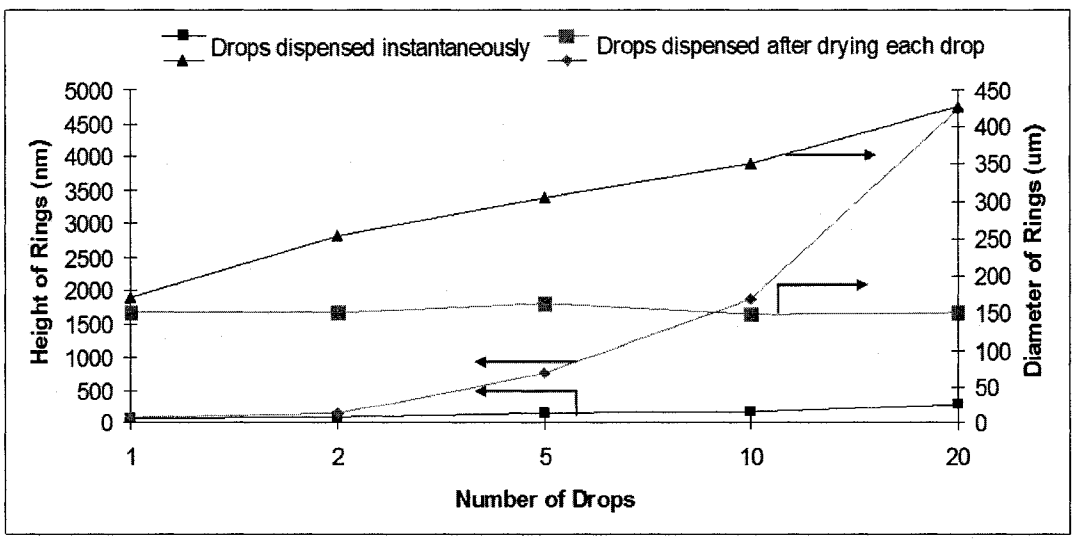

Figure 5.10 Diameter and height variation of polymer micro-rings Vs number of IJ printed drops after plasma etching

The height of the inner base layers before and after RIE was monitored using the stylus surface step profilometer to ensure the complete removal of the inner layer. Figure 5.11 shows the height of inner layers before and after RIE for both techniques.

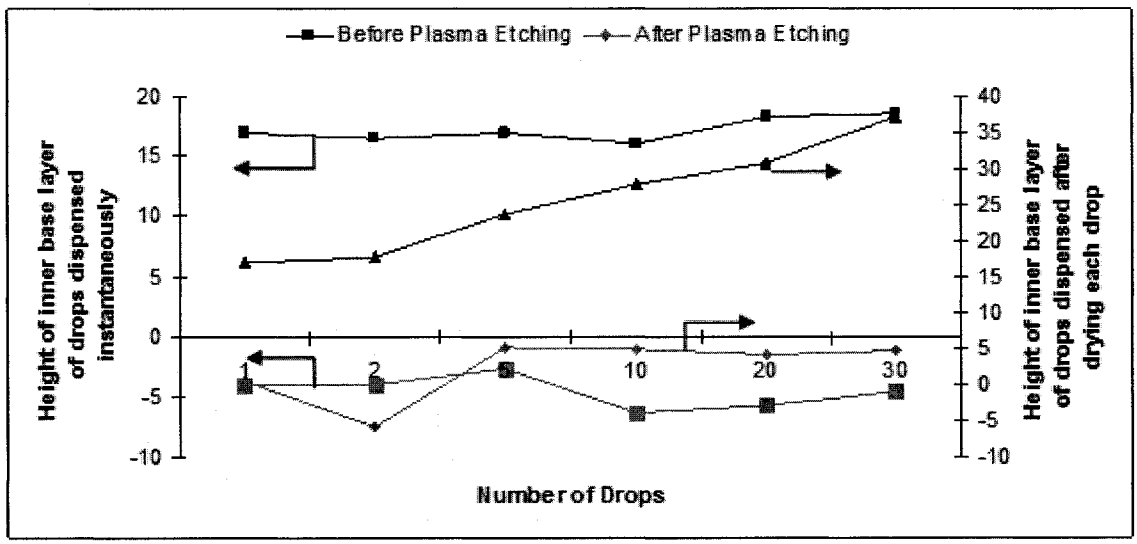

Figure 5.11 Height of inner base layer before and after RIE

The measured results show that the height of micro-rings is in the range of 0.1 μm to 10 μm and have diameter up to 500 μm. Drops dispensed by drying each drop (second technique) showed a significant change in height and negligible change in diameter. High aspect ratio micro-rings can be fabricated by this technique. Whereas the drops dispensed without drying (first technique) showed significant increase in diameter.

5.3 Micro-ring Applications

5.3.1 Micro-ring Pixels for High Resolution PLED

5.3.1.1 Detailed steps for design and fabrication of micro-ring PLED pixels

Step 1: Patterning of ITO coated glass substrate

ITO coated glass substrate used as an anode for polymer LED was bought from Delta Technologies. A positive photoresist is used for masking the ITO layer during exposure to ITO etchant. The pattern transfer was performed using the UV photolithographic process. Photolithography is an optical means of transferring patterns from a mask to the substrate. The steps for photolithography process involve

1. ITO cleaning
2. Prebaking
3. Photoresist coating
4. Softbaking
5. Alignment and exposure
6. Development
7. Hardbaking
8. Etching

A commercially available PR 1813 positive resist (from Shipley) was used in this process for pattern transfer. As this resist is quite viscous, it can be spun into thick layers over a spin range of 500-2500 rpm. As a first step, the ITO used for lithography was chemically cleaned prior to photoresist coating to remove any traces of particulate matters, organic, inorganic, and metallic impurities. The substrate was then prebaked at a

high temperature (175 °C for 20 min) to ensure that it was completely dry. Approximately 1 ml of PR 1813 photoresist was dispensed on the glass slide and spun according to the spin curve shown in Figure 5.12.

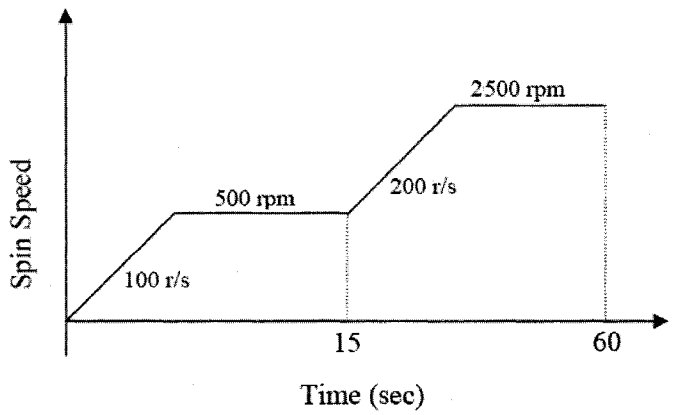

Figure 5.12 Spin curve for coating PR 1813

After spin coating the photoresist, softbaking was done at 110°C for 90 sec. Softbaking plays an important role in the subsequent exposure and development steps. Under-softbaking will prevent light from reaching the photoactive compound; as a result, considerable solvent remains after developing. On the contrary, over-softbaking will degrade the sensitivity of resist by destroying a part of the sensitizer. After alignment with a photomask, the resist-coated substrate was exposed to UV-light for 60 sec. Exposing the resist to the UV light (I-line of Hg lamp, with wavelength of 410 nm) induces the photochemical reaction in the resist sensitizer which allows the resultant product to dissolve in the solvents.

The resist samples were developed in MF 319, positive photoresist developer for about 2 min. The developed patterns were inspected under an optical microscope for

undeveloped resist or residues in the developed area. The patterns were found to be fully developed. This patterened sample was hard-baked for 35 min at 110°C.

The composition for ITO etchant is prepared by mixing the following chemicals in the composition of 20% HCl, 5% HNO_3 and 75% H_2O. At room temperature it takes about 10 min to etch the ITO layer. The samples are constantly observed under optical microscope to ensure complete etching. Now the masked photoresist is removed with acetone. Figure 5.13 shows the pictorial representation of the patterned ITO.

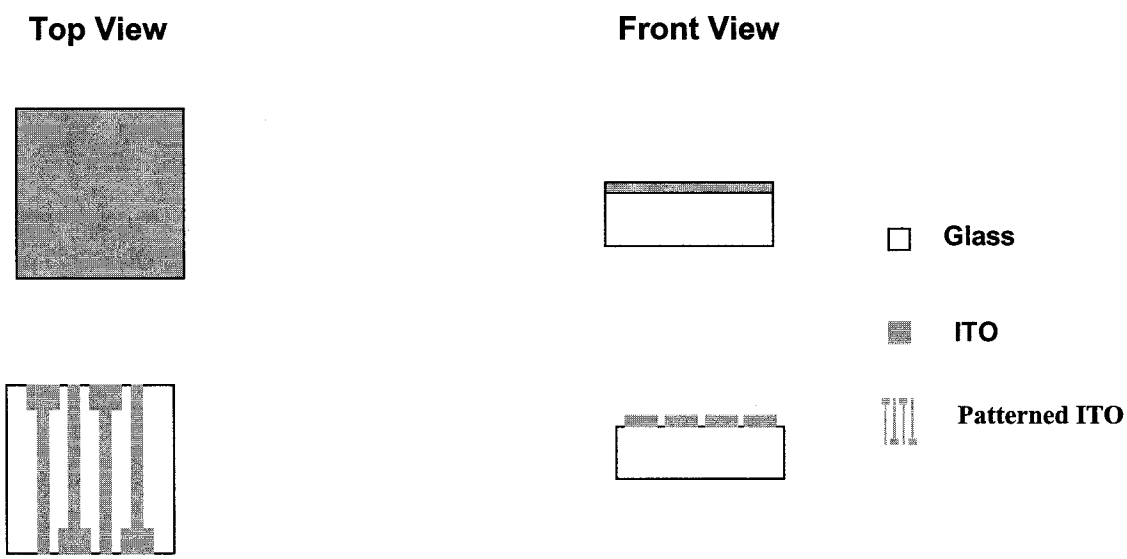

Figure 5.13 ITO patterned glass slide

Step 2: Cleaning and O_2 plasma treatment of ITO

The workfunction of ITO lies between 4.5 – 5.0 eV and the electronic properties are strongly dependent on the preparation and cleaning methods used. Following a proper cleaning process helps improve the workfunction of ITO. Thus the ITO patterned

substrate was sonicated in DI water, acetone and IPA for 10 min each. Finally the substrate was rinsed in DI water followed by drying with nitrogen gun.

After cleaning the ITO substrate the next important step for improving the work-function of ITO is oxygen plasma treatment. Since oxygen is electronegative, it renders negative charge to the surface of ITO which may cause depletion of electrons below the ITO surface which induces band bending and increases the work function.

The ITO substrate is loaded into the top chamber of the Micro-RIE unit. After pumping down the chamber to 50 mtorr, the RF power was turned on (200 W), establishing a pale blue plasma. The inlet valve on the chamber was then slowly opened to let in a small stream of oxygen (5.5 sccm), turning the plasma pink. The substrate was exposed to oxygen plasma for 3 min. After 3 min, the RF power was turned off, the chamber was vented and the substrate was removed.

Step 3: Inkjet printing of micro-rings

The temperature of the substrate was set to 70°C prior to inkjet printing. PEDOT-PSS solution to be used was filtered through 0.45 μm filter. A 70 μm print head nozzle was used for printing the polymer solution. Array of micro-rings were printed adjacent to each other on patterned ITO. The micro-rings were fabricated in such a way that the outer edge of the rings is much thicker as compared to the inner base layer. The techniques used for fabricating micro-rings have been discussed in chapter 5. The micro-rings had diameter in the range of 110 - 120 μm and the thickness of the ring on the periphery of each dot was in the range of 5-7 μm. The micro-rings were also fabricated using "dispense and dry" technique in order to achieve micro-rings with increased heights but fixed diameter. Thus the heights achieved were about 500 nm while the diameter was

fixed in the range of 110 - 120 μm. The height of the inner base layer was about 10 nm. Figure 5.14 shows the schematic representation of inkjet printed micro-ring array fabricated on patterned ITO with outer ring and central base layer of the polymer.

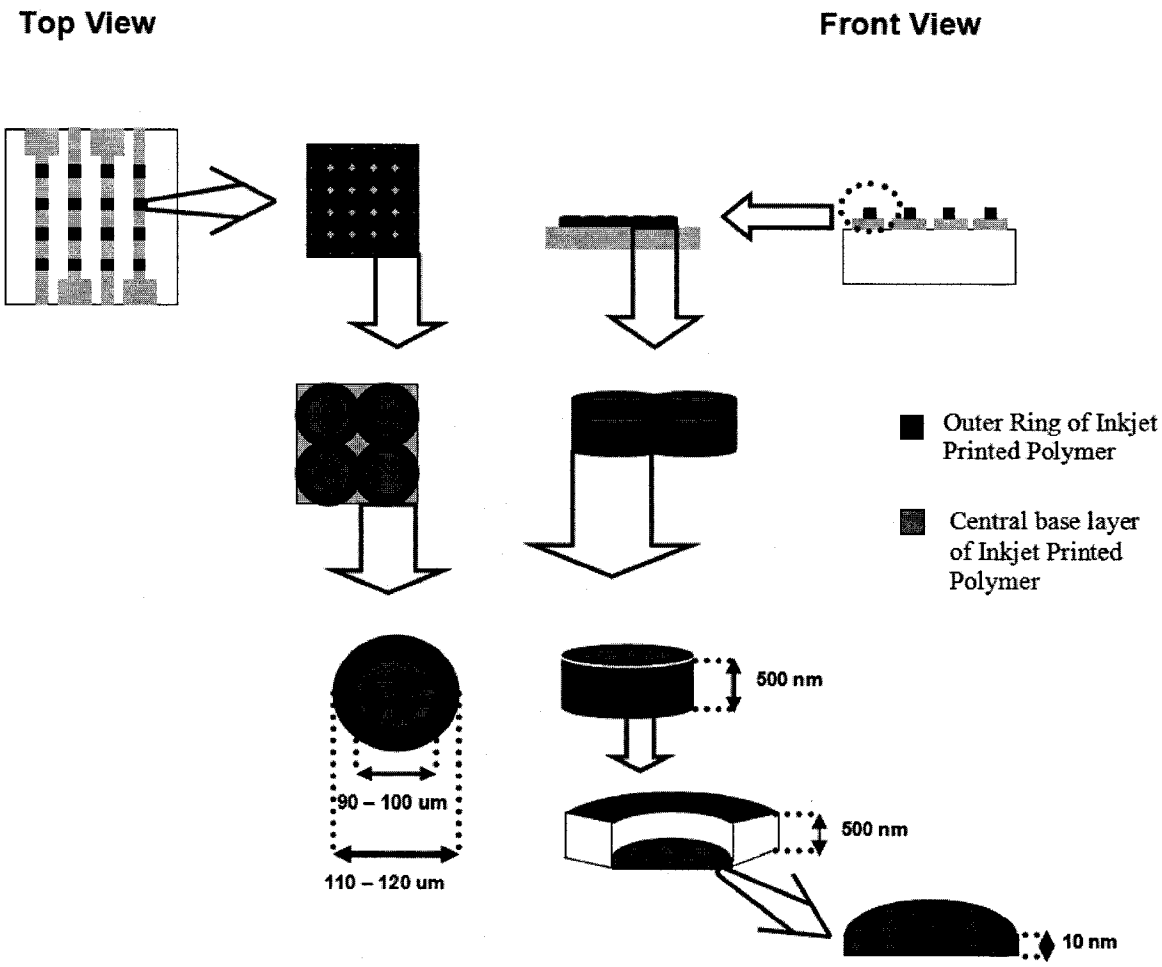

Figure 5.14 Schematic of IJ printed micro-rings with outer ring and central base layer

Step 4: Oxygen plasma reactive ion etching

The central base layer was etched in order to expose the ITO that acts as an anode. Oxygen plasma reactive ion etching was used to remove 10 nm central base layer. After etching the central layer, oxygen plasma comes in contact with ITO which improves the work function of ITO. The improved work function enhances the hole

injection from ITO to the polymer. Oxygen plasma etching was performed at a pressure of 375 mTorr and power of 200W until the inner base layer was completely removed. Finally we obtain a hollow micro-ring or micro-torus as shown in Figure 5.15.

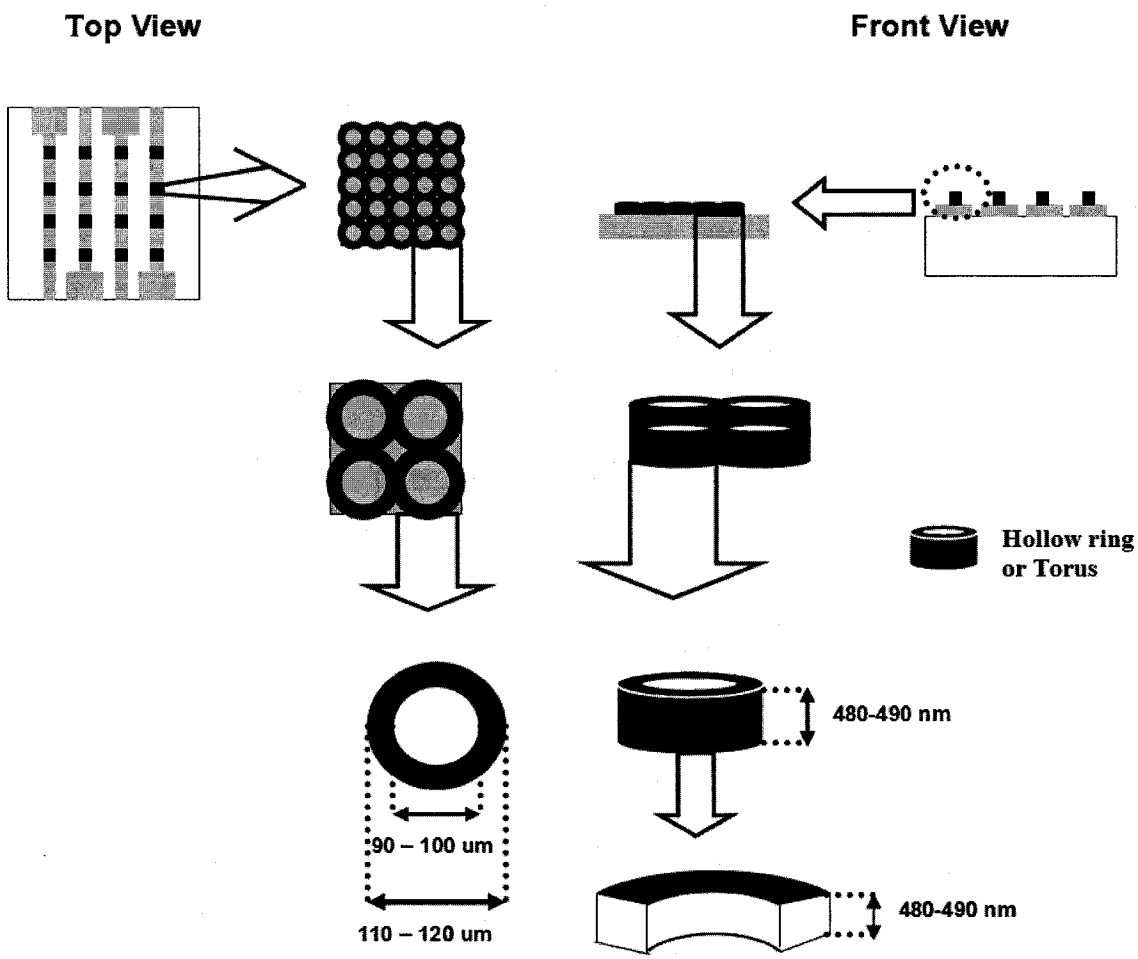

Figure 5.15 Plasma etching of micro-rings to form Torus

Step 5: Spin coating of electroluminescent polymer (MEH-PPV)

Light emitting diodes are fabricated using [2-methoxy-5-(2-ethylhexoxy)-1, 4-phenylene vinylene] (MEH-PPV) as an electroluminescent polymer. A 0.6% solution of MEH-PPV in p-xylene is prepared by sonicating the solution for more than 3 hrs at 50°C. Approximately 1 ml of MEH-PPV was dispensed on inkjet printed torus and spun

according to the spin curve shown in Figure 5.16, resulting in a 100 nm thick film as shown in Figure 5.17. The samples are kept in vacuum overnight for complete drying of the MEH-PPV layer.

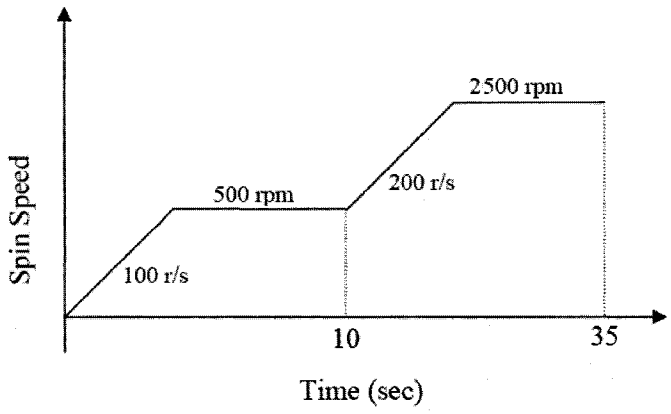

Figure 5.16 Spin curve for coating MEH-PPV

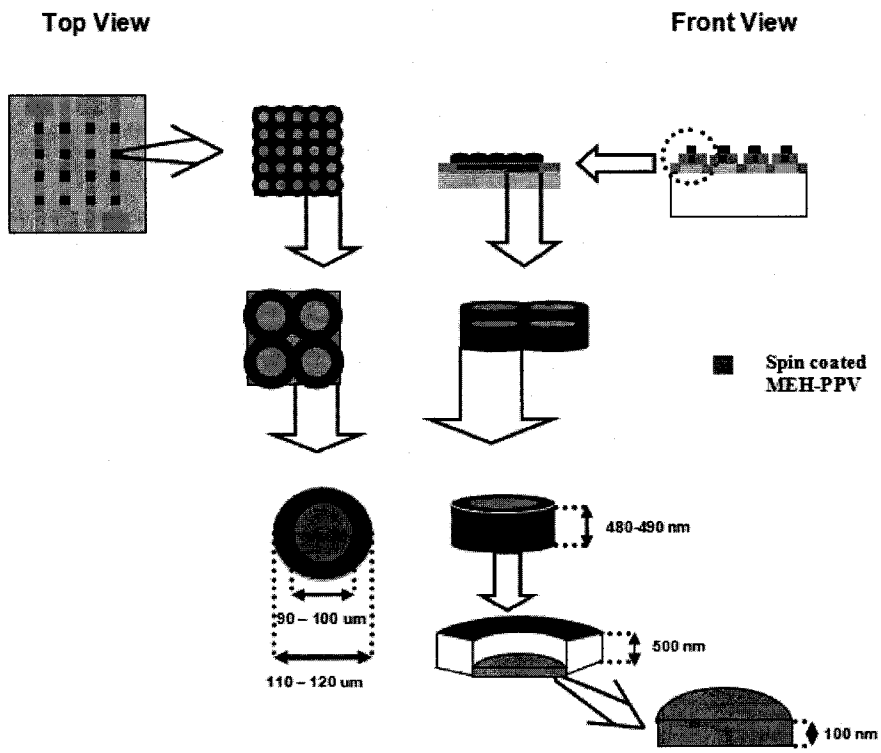

Figure 5.17 Spin coated MEH-PPV on inkjet printed Torus

Step 6: Aluminum evaporation for cathode electrode

Thermal evaporation of aluminum is performed at pressures around 5×10^{-7} Torr at a rate of 3 Å/s by using a shadow mask. The thickness of the aluminum deposited is around 100 nm as shown in Figure 5.18. Aluminum electrode acts as cathode amd ITO serves as anode . The MEH-PPV layer is the active electroluminescent layer.

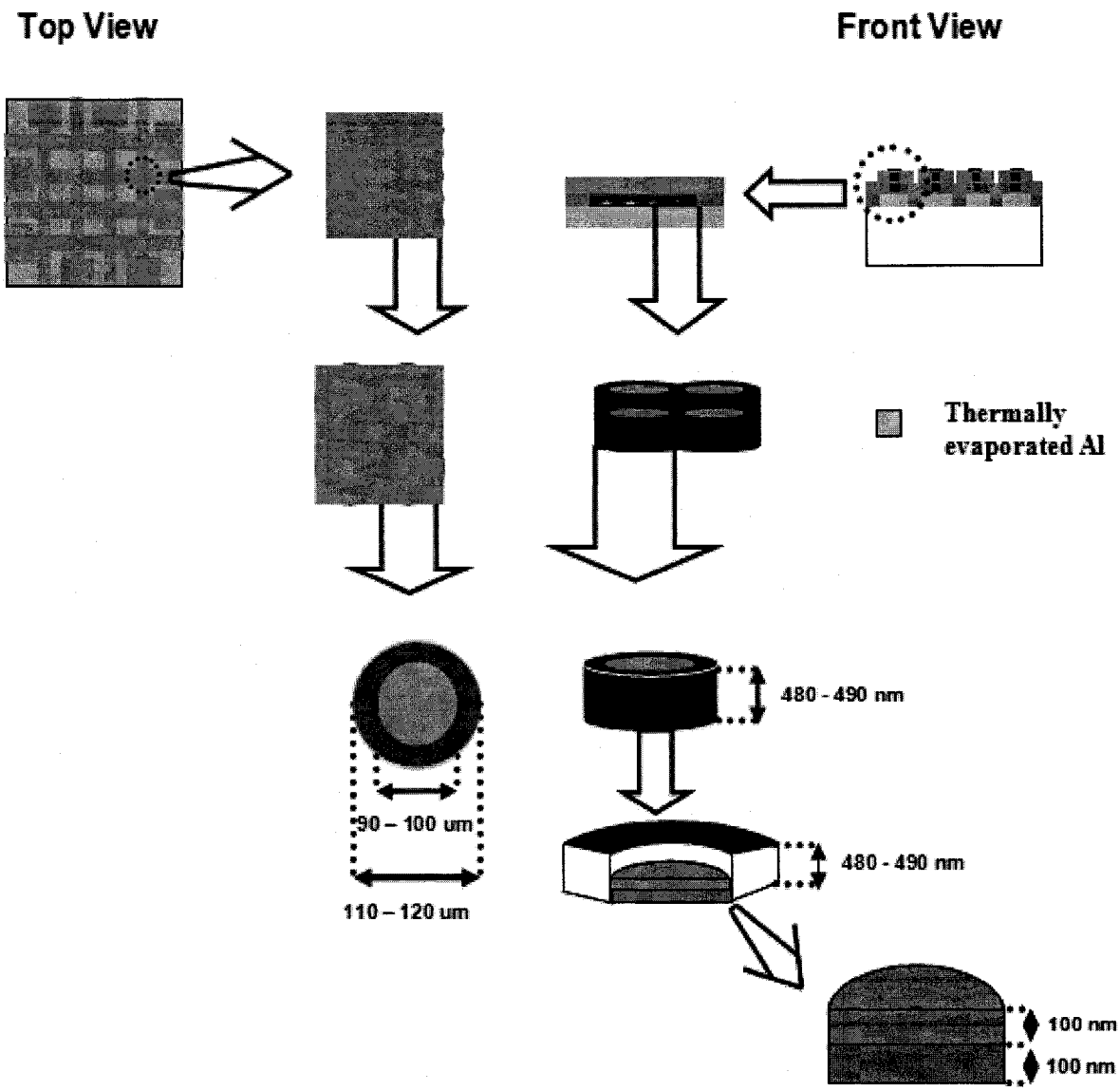

Figure 5.18 Thermal evaporation of aluminum

Step 7: Applying bias voltage

A positive bias voltage is applied to ITO that acts as an anode in the sandwiched structure ITO/MEH-PPV/Al. A negative bias voltage is applied to aluminum electrode. MEH-PPV acts as the light emitting polymer due to recombination of holes and electrons from ITO and Al, respectively, as shown in Figure 5.19. The recombination of electrons and holes form an exciton which when falls to the ground state emits a photon. Thus each micro-ring acts as a single light emitting pixel.

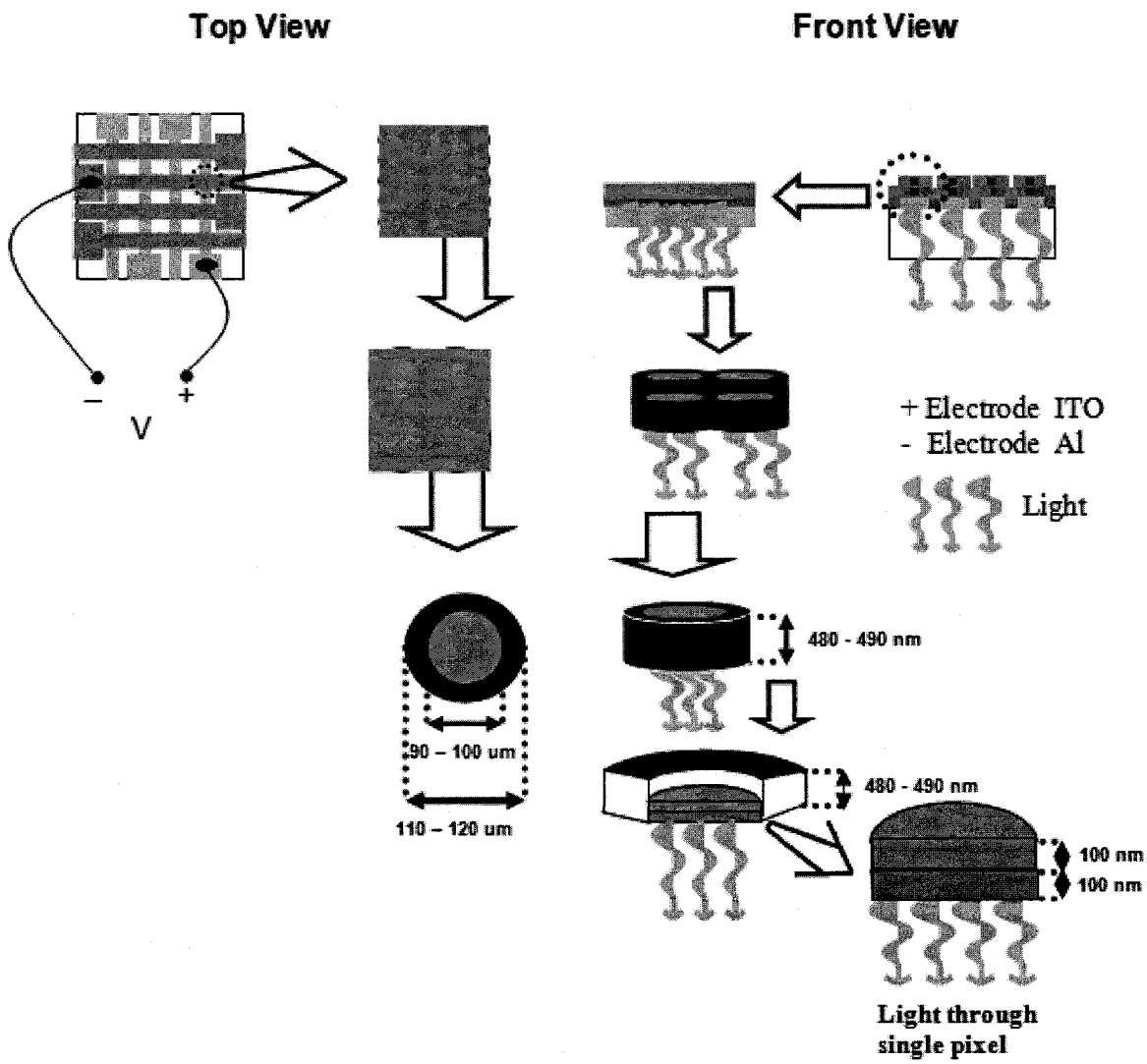

Figure 5.19 Light emitting pixels on applying voltage bias

5.3.1.2 Results and discussion

Figure 5.20 demonstrates the high resolution (> 200 pixels per inch) polymer light emitting diode through inkjet printed micro-ring torus for the single inkjet printed micro-ring array. The light is emitted around a voltage bias of 4V. The brightness of the light emitting device increases at higher voltages.

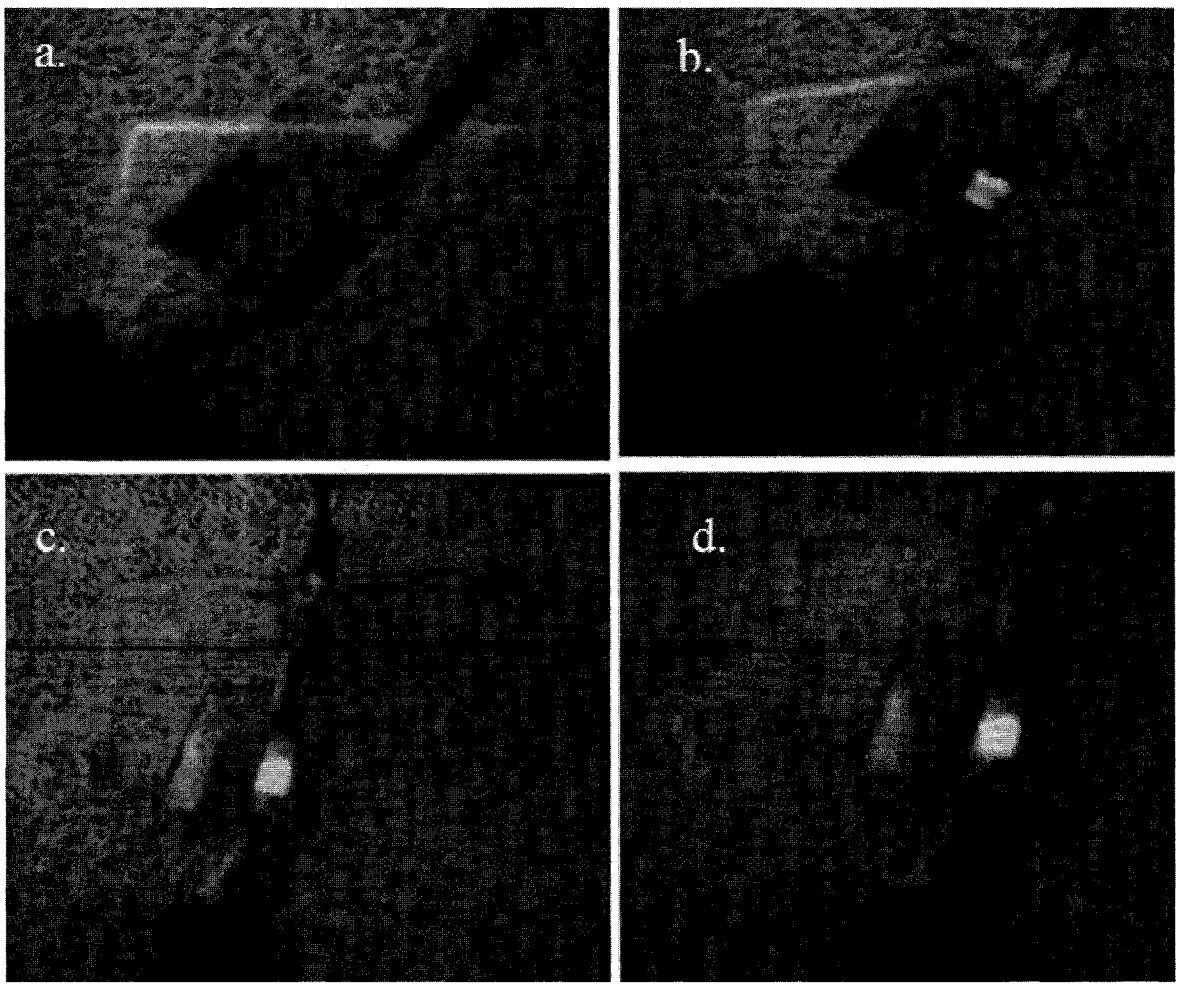

Figure 5.20 Polymer light emitting diodes (a) without bias (b) At 4V (c) At 5V (d) At 5V with zoom

The I-V characterization of the PLEDs is done using electrical probe station (Figure 5.21). The 236, 237, and 238 units are fully programmable instruments, capable of sourcing and measuring voltage or current simultaneously.

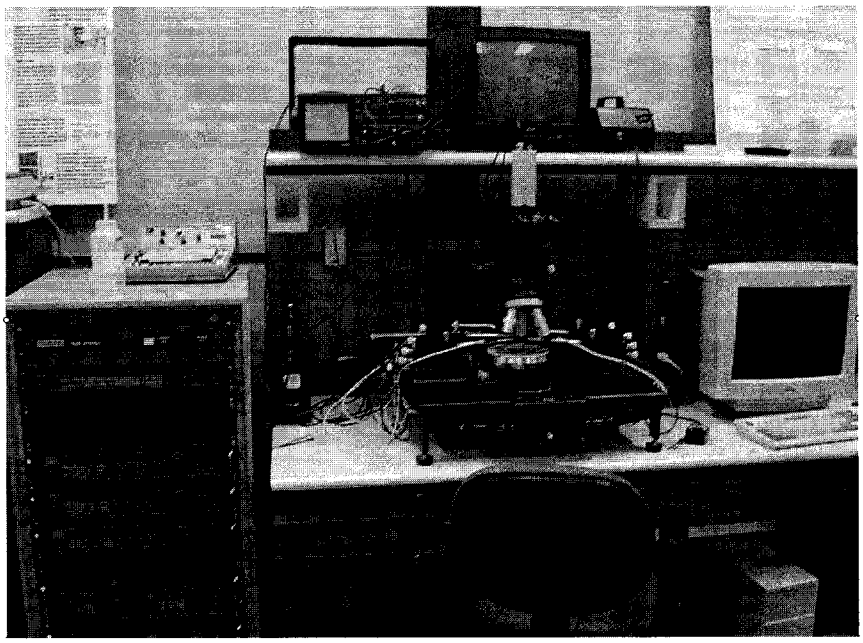

Figure 5.21 Keithley Probe Station

Various polymer light emitting diodes were fabricated to study the effect of thickness variation of MEH-PPV on the device characteristics. All the above mentioned steps were kept the same except step 6. MEH-PPV was spin coated at various spin speeds to vary the thickness of deposited layer. Thus we attained devices with MEH-PPV layer thickness of 80 nm, 100 nm, 120 nm and 150 nm. The I-V characteristics of these devices are shown in Figure 5.22.

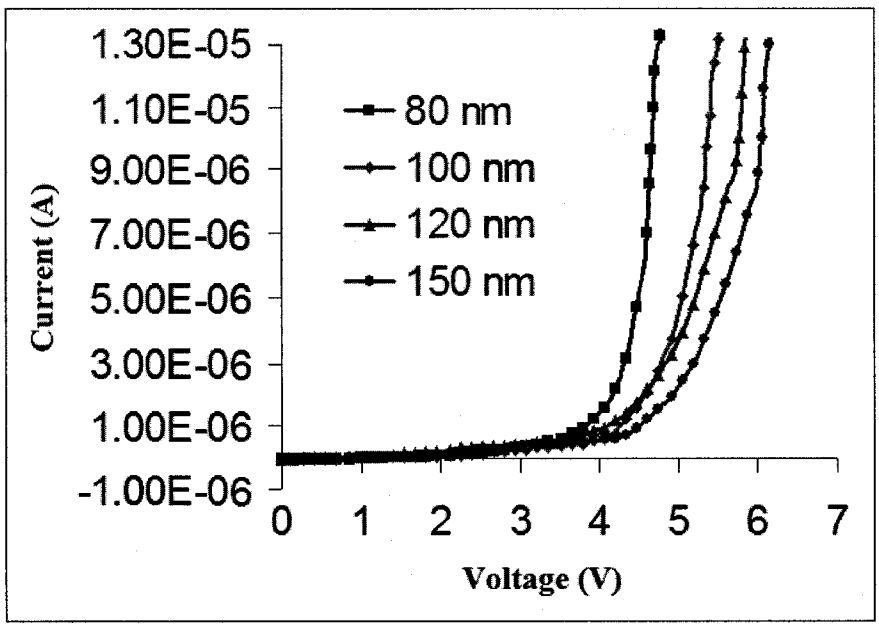

Figure 5.22 I-V characteristics for varying MEH-PPV film thickness

It is evident from the I-V characteristics that with decreasing thickness of the MEH-PPV film, the turn-on voltage of the device decreases. But it was observed that the devices with smaller MEH-PPV thickness showed smaller lifetime. Moreover the devices with smaller thickness cannot withstand higher voltages as compared to those with thicker MEH-PPV films. Thus there is a trade-off between low turn-on voltages and longer lifetime.

Higher the number of pixels per unit, better is the resolution. An array of micro-rings that we used for high resolution polymer light emitting diode had empty space (void) in between four adjacent micro-rings as shown in Figure 5.23. If we can remove the voids, pixels will be closer to each other. Thus we can have more number of pixels per unit i.e. we improve the resolution of our device by fabricating compact micro-rings.

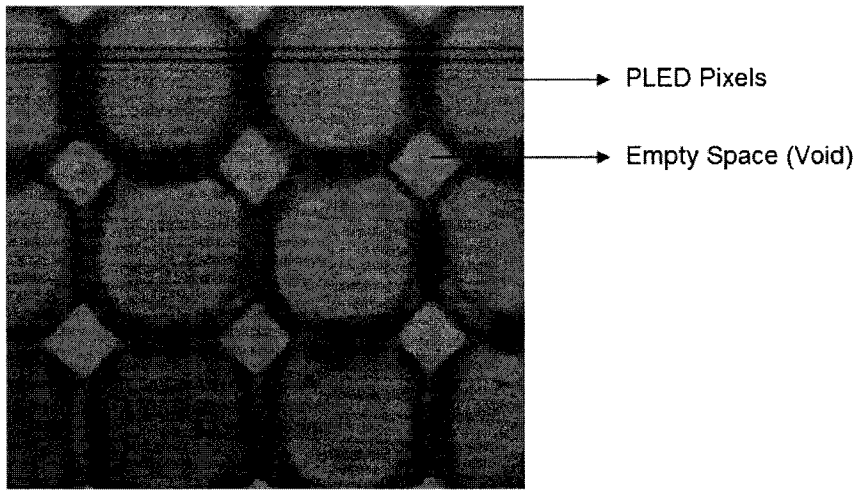

Figure 5.23 Voids between pixels

In our attempt to further improve the resolution we dispensed drops close enough to each other such that the voids are covered. This array was examined under scanning electron microscope to find out if the voids were eliminated. But the overlapping of the drops gave an intertwined array as shown in Figure 5.24.

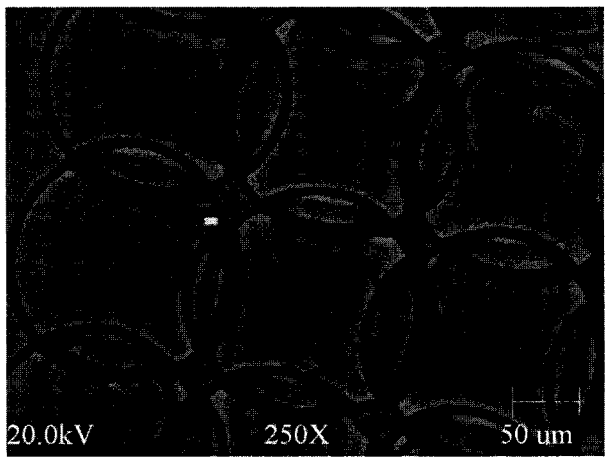

Figure 5.24 Intertwined array of micro-rings

In this case each micro-ring cannot act as a single pixel and it is very difficult to spin coat MEH-PPV within these micro-rings. In our next set of experiments we reduced

the temperature of the substrate from 90°C to 70°C. Figure 5.25 shows the optical microscope image of the obtained compact micro-rings before and after etching the inner base layer at 70°C.

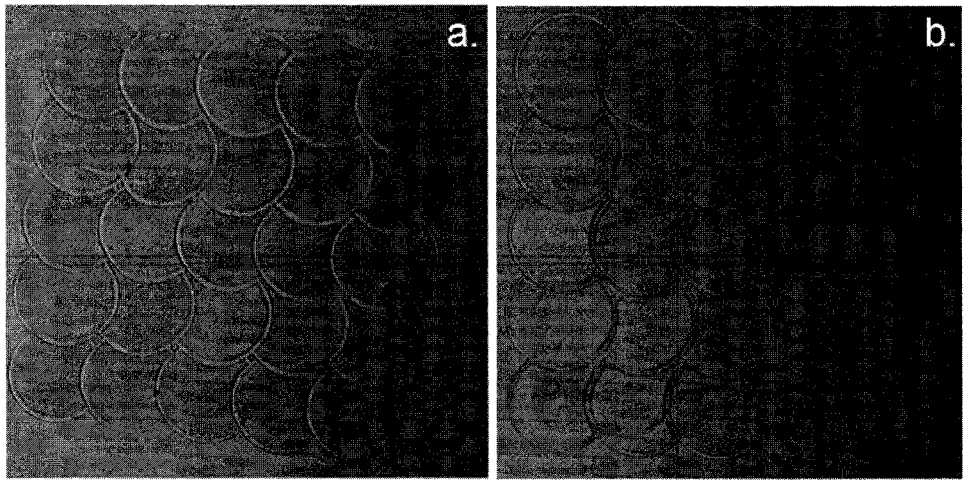

Figure 5.25 Optical microscope image of compact micro-rings (a) before RIE (b) after RIE

The micro-rings now are not intertwined due to the fact that the edge of the drop that falls first is dissolved by the following second drop and adds to the thickness of the second micro-ring, and so on. We can still see that the micro-ring pixels formed are not completely uniform even after etching the inner base layer.

In next set of experiments we changed the rate of dispensing. The time lapse between each drop dispensed was varied to study its effect. It was observed that decreasing the rate of dispensing i.e. increasing the time lapse between two drops produced more uniform micro-rings before and after etching the inner base layer as shown in Figure 5.26.

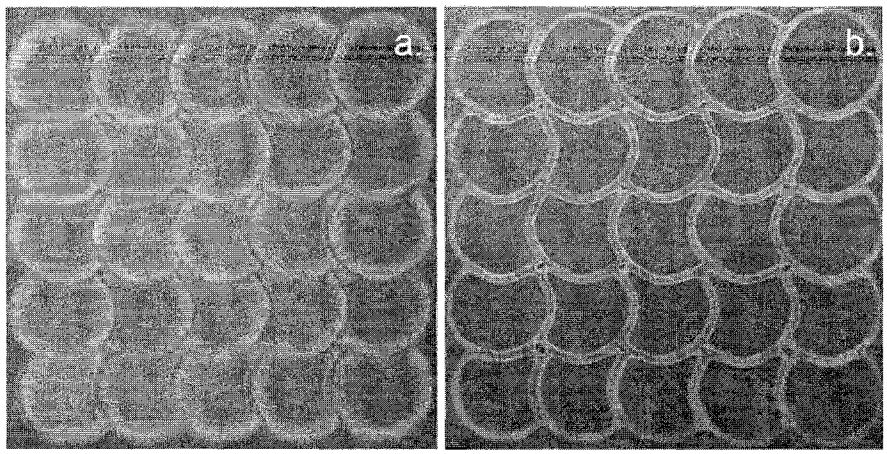

Figure 5.26 Optical microscope image of compact micro-rings with decreased rate of drop dispensing (a) before RIE (b) after RIE

This uniformity of the micro-rings by changing the rate of dispensing is attributed to the fact that the second drop is dispensed only when the first drop has completely moved the solute from the inner layer to the outer periphery. Thus there is no uneven deposition left due to instant drying of drop which solidifies the solute inside the micro-ring. From Figure 5.26(b), we can see that the color of outer periphery is different from that of the inner edges of the array. This is due to the fact that the inner edge consists of polymer from its own drop and part of polymer from the previous drop which was dissolved by the second drop. Thus the thickness of the inner edges is more than the outer edge which is shown by color change in the optical image. These compact micro-ring pixels contribute to the further improvement in resolution of polymer light emitting diodes.

5.3.1.2 Degradation study of MEH-PPV thin films due to oxygen and moisture traps

The lifetime and efficiency of the polymer light emitting diodes (PLED) and polymer field effect transistors need to be improved in order to compete with conventional inorganic semiconductor devices. MEH-PPV is an electroluminescent polymer widely used in the fabrication of PLEDs [112-114]. The degradation of MEH-PPV is a major factor that leads to short lifetime and low efficiency of PLED. It is believed that the presence of oxygen and moisture traps results in the degradation of MEH-PPV polymer.

Techniques such as deep level transient spectroscopy and thermally stimulated current are normally used to identify the origins and states of the traps in polymer layers. Campbell et al, [115] used the deep level transient spectroscopy technique to study traps in the PPV based Schottky diodes. Recently Tseng et al, [116] have reported that the molecular oxygen and moisture traps can form in MEH-PPV through field induced thermally stimulated current and photoexcitation thermally stimulated current.

The electrical and chemical changes in MEH-PPV polymer leading to device degradation are studied. The oxygen traps in MEH-PPV are characterized through Attenuated Total Reflection Infrared (ATR-IR) spectroscopy and capacitance – voltage (C-V) analysis.

5.3.1.4 Design and fabrication of MEH-PPV thin films for C-V and ATR-IR analysis

A 0.6% solution of MEH-PPV in p-xylene was spin-coated on p-type silicon substrates, resulting in an 80 nm thick MEH-PPV film. The samples were kept in vacuum overnight for complete drying of the MEH-PPV layer. Subsequently, a 150 nm thick aluminum was thermally evaporated on the MEH-PPV film. The pressure in the thermal evaporator was maintained at 1×10^{-6} Torr during deposition. A shadow mask was used for selective aluminum deposition. Reactive ion etching was used to remove the polymer from the exposed areas. The C-V measurements of the resulting metal-insulator-semiconductor (MIS) (Al/MEH-PPV/ p-Si) devices were conducted using the electrical probe station. The high frequency and quasi-static C-V measurement was done using Keithley 590 CV analyzer and Keithley 595 CV analyzer respectively.

The ATR-IR spectroscopic measurements were performed using a Thermo Nicolet Nexus 470 FTIR equipped with ZnSe ATR crystal. Infrared light enters through the ZnSe crystal and passes through the MEH-PPV sample where it is internally reflected. The spectrometer is fitted with a DTGS-KBr detector and all the ATR-IR spectra are calculated from 512 scans at 4 cm^{-1} resolution. The samples were prepared by spin coating a MEH-PPV layer on aluminum and overnight drying in vacuum before measurements.

5.3.1.5 ATR-IR spectroscopy

Figure 5.27 show the ATR-IR spectroscopy results.

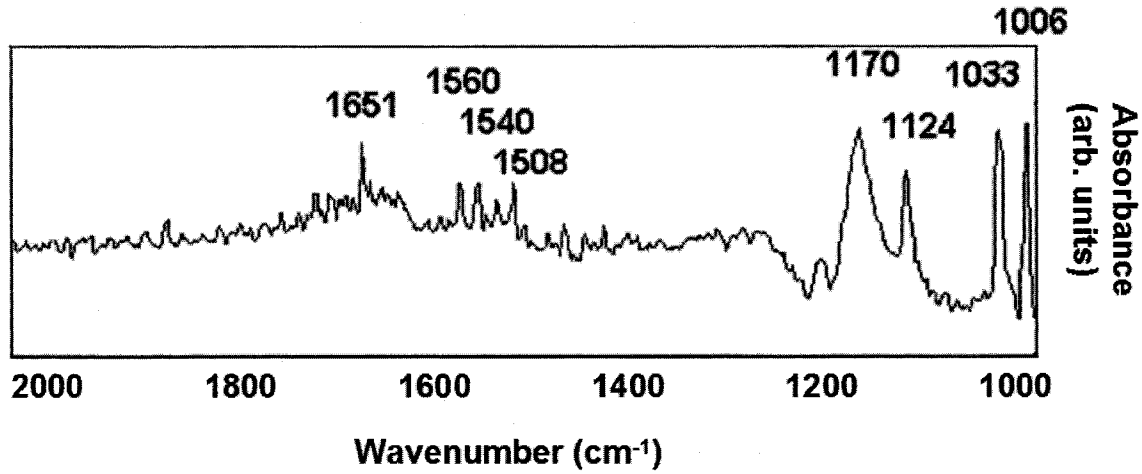

Figure 5.27 ATR-IR spectrum depicting the peaks of the MEH-PPV sample after 24 hrs aging in ambience at room temperature

The detailed peak information is listed in Table 5.1. Our assigned modes to the peaks are consistent with the report of Scott et.al., [117].

Table 5.1: ATR-IR spectroscopic results from MEH-PPV polymer

Wavenumber (cm^{-1})	Modes
1651	Carbonyl associated with aromatic aldehyde
1560, 1540, 1508	Phenyl ring stretch
1170	Strong absorption from phenyl – oxygen stretch
1124	weak absorption from oxygen – alkyl group
1033 and 1006	trans – hydrogen wagging bands

The spectral peak at 1651 cm^{-1}, indicates the carbonyl mode associated with aromatic aldehyde.The peaks at 1560, 1540 and 1508 cm^{-1} are associated with phenyl ring stretching mode. The two peaks at 1170 cm^{-1} and 1124 cm^{-1} are associated with strong and weak absorption from phenyl – oxygen stretching and oxygen – alkyl groups, respectively. The vibrations at 1033 cm^{-1} and 1006 cm^{-1} are the wagging bands associated with trans–hydrogen. The change in concentration of oxygen in the MEH-PPV was monitored with aging in ambient conditions.Figure 5.28 shows the infrared spectrum of MEH–PPV film (a) after 1 hr (b) after 24 hrs (c) after 48 hrs (d) after 72 hrs aged environmentally in air at room temperature. The presence of a carbonyl peak at 1651 cm^{-1} with aging (shown by an arrow) indicates the presence of oxygen in the polymer film. With further aging, the changes in the peaks at 1170 cm^{-1} and 1124 cm^{-1} show that the phenyl – oxygen and oxygen – alkyl groups are stretching and losing conjugation.

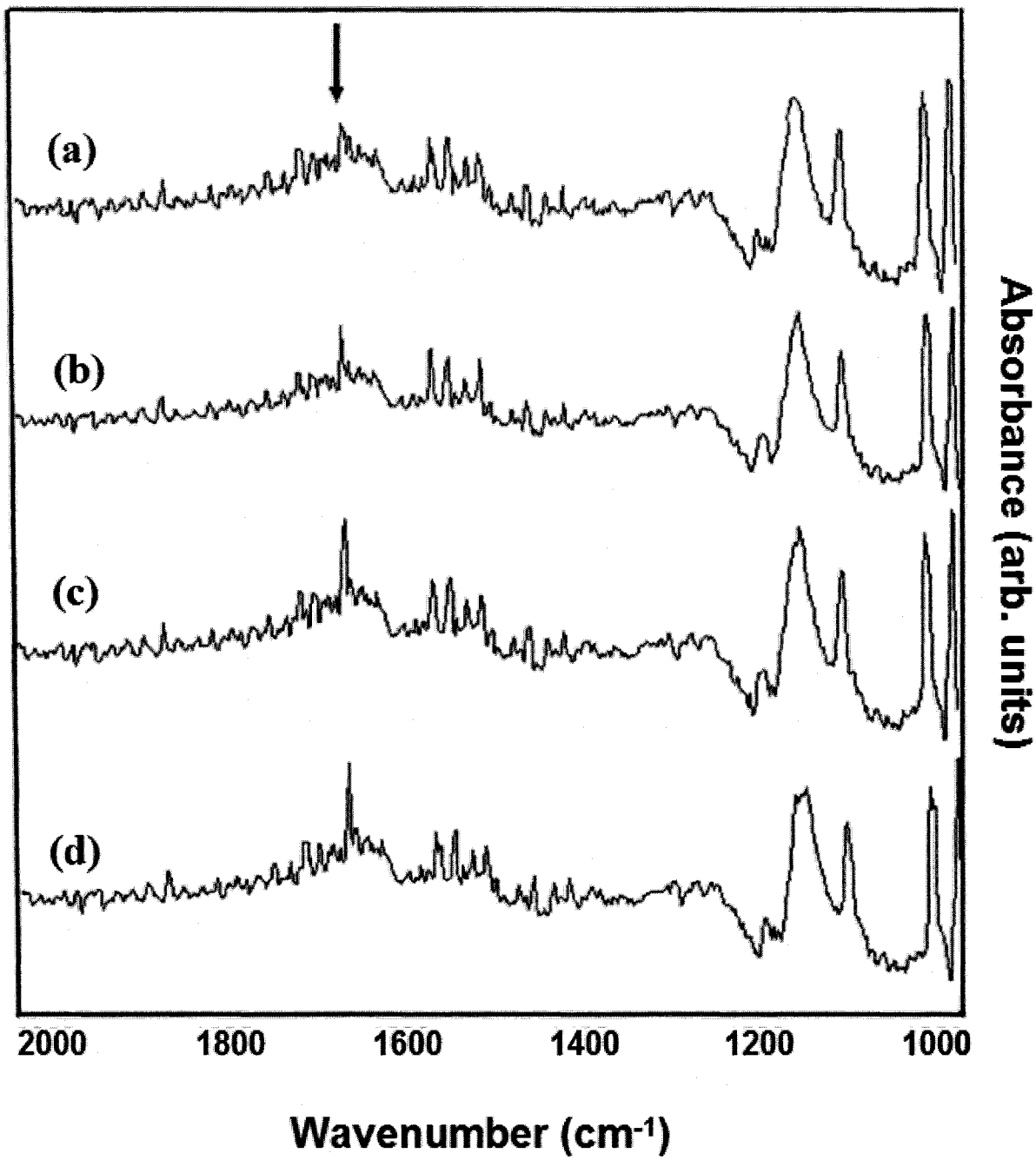

Figure 5.28 ATR-IR spectrum depicting the carbonyl peak formation at 1651 cm^{-1} with aging (a) after 1 hrs (b) after 24 hrs (c) after 48 hrs (d) after 72 hrs in ambience at room temperature (the arrows point to the peak)

5.3.1.6 Capacitance – voltage analysis

Figure 5.29 provides high frequency C-V curves for the MIS (Al/MEH-PPV/ p-Si) capacitor. The results show 63.7% decrease in C_{max} capacitance after 24 hours, indicating an increase in the thickness of the MEH-PPV polymer layer and change in dielectric constant of the polymer. The Alpha step profilometer shows 50% increase in film thickness. So, the rest of the decrease in capacitance is due to a change in dielectric constant.

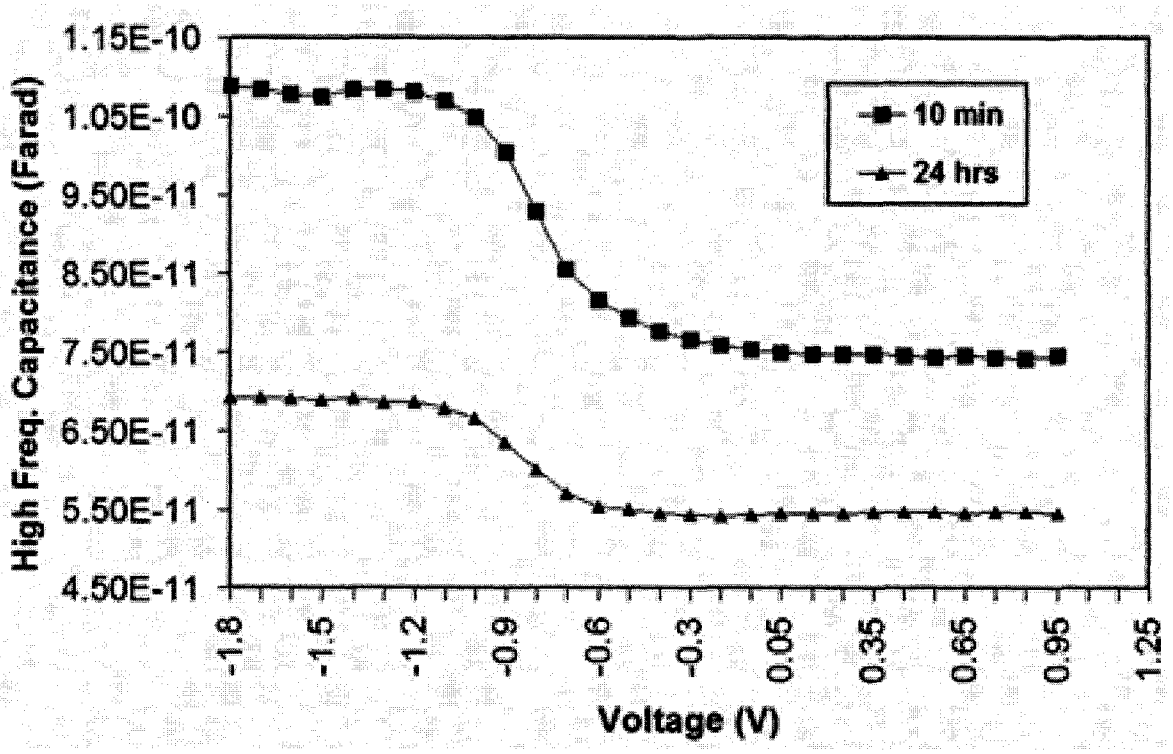

Figure 5.29 High-frequency Capacitance – Voltage curves measured on 10-min and 24-hr old samples of MEH-PPV

Figure 5.30 shows quasi-static C-V curves for the MIS capacitor with p-type Si as the substrate. One C-V curve was measured 10 minutes after the sample was prepared and the other C-V curve was measured after 24 hours. These results show the occurrence of an extension to the weak inversion region. This suggests that the minority carriers

from the p-Si start recombining with the holes in the MEH-PPV polymer layer. This extension to the weak inversion region extends until the minority carriers recombine. After recombination of the minority carriers, the quasi-static C-V curve follows the strong inversion.

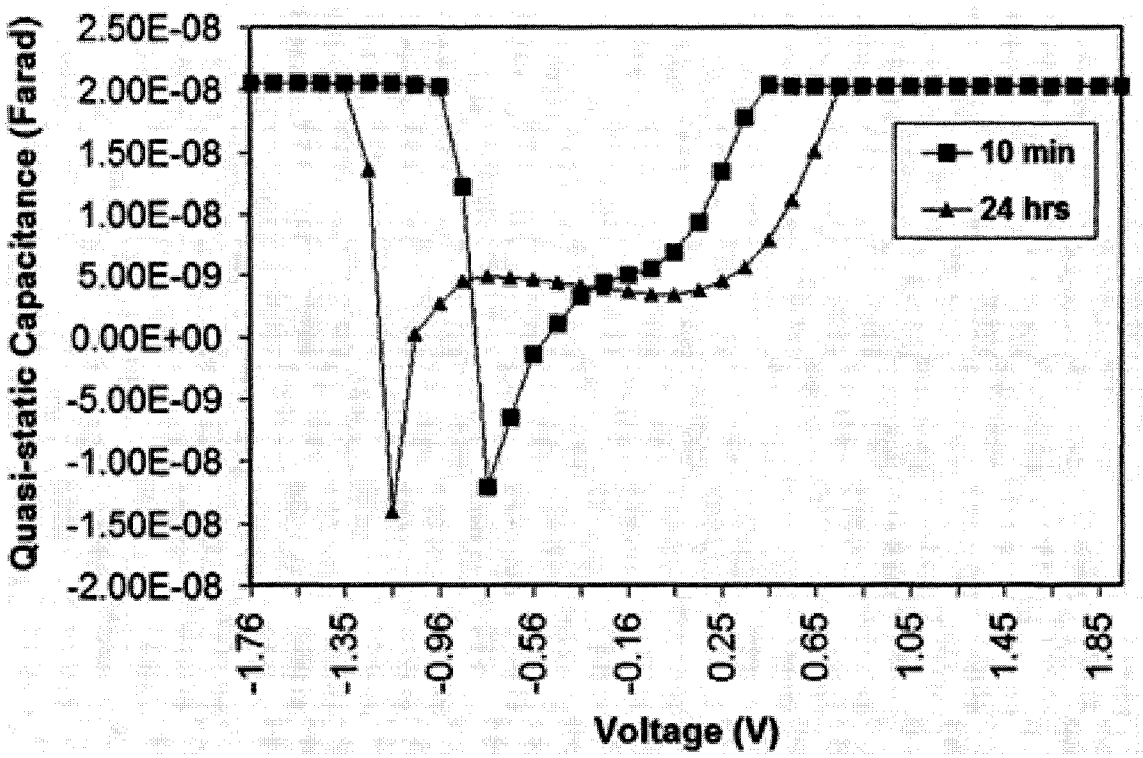

Figure 5.30 Quasi-static Capacitance -Voltage curves measured on 10-min and 24-hr old samples of MEH-PPV

From the second C-V curve in Figure 6.5 it can be observed that with aging, the extension in the weak inversion region of this curve extends further. Other researchers have shown that the molecular oxygen serves as a trap in the MEH-PPV layer, which attaches with the electron to form negative ion O_2^-, an n-type carrier trap. In the weak inversion region the minority carrier (electrons) enhancement occurs.

The electrons start combining with oxygen present in MEH-PPV layer as

$$O_2 + e^- \rightarrow O_2^-$$

The charge neutrality requires every positive charge to be compensated by an equal and opposite charge in MEH-PPV and silicon. Thus the strong inversion will be delayed due to capture of electrons by oxygen and causing more extension of the weak inversion region. In this work, the MEH-PPV trapped charge density has been determined from the high frequency and quasi-static C-V curves. The trapped charge density of the samples measured after 10 minutes was $1.2 \times 10^{+11}$ cm^{-2} and the trapped charge density of the same sample measured after 24 hours was $1.7 \times 10^{+11}$ cm^{-2}. This increase in the trapped charge density is attributed to the presence of oxygen negative ions (O_2^-) that also explains the extension of the weak inversion region with aging in the quasi-static C-V curve.

5.3.2 Micro-ring Array for PEDOT-PSS Based Humidity Sensor

The devices were fabricated on thoroughly cleaned Pyrex® glass slides. PEDOT-PSS based humidity sensors were fabricated by depositing layer-by-layer (LbL) nano-assembled film on a platform of inkjet printed micro-rings. These humidity sensors were compared with devices fabricated by inkjet printing, LbL assembly and spin coating individually. All these sensors fabricated with different techniques were tested for sheet resistance, sensitivity, response time, recovery time and degradation. Attenuated total reflection infra-red spectroscopy (ATR-IR) was used to study the sensing mechanism of PEDOT-PSS film after moisture absorption.

5.3.2.1 Design and fabrication of humidity sensors

An array of inkjet printed micro-rings of PEDOT-PSS was made by using drop-on-demand Microdrop inkjet printer. A 70μm diameter nozzle was used for IJ printing of polymer micro rings from aqueous solution of PEDOT-PSS. Oxygen plasma treatment was done to the substrate prior to dispensing the drop to make the surface hydrophilic. Oxygen plasma was also used to remove the center base layer of the micro-rings.

Figure 5.31 shows an array of inkjet printed micro-ring pattern designed as a platform for the fabrication of humidity sensor using layer-by-layer nano-assembly. The diameter of each ring is 120 μm and height of the ridge is 100 nm. The width of the ridge is 8-10 μm as measured by Alpha step profilometer. The glass substrate was heated in order to enhance the evaporation of the solvent to form micro-rings. This micro-pattern is unique with its resolution better than usual patterns produced with inkjet printing.

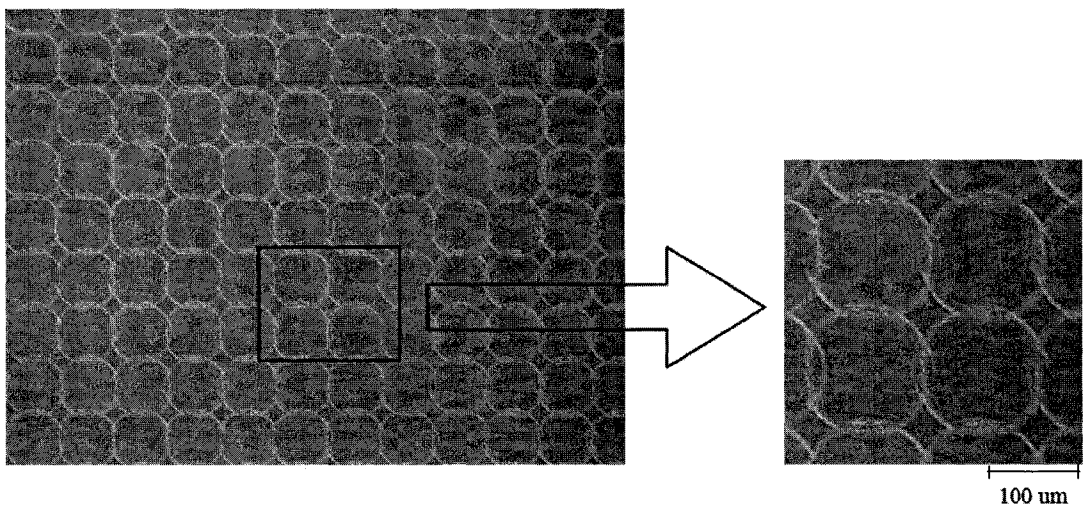

Figure 5.31 A micro-ring array fabricated by inkjet printing of conducting polymer PEDOT-PSS

The cross-section of the device is shown in Figure 5.32. This is due to the fact the resolution is based not on inkjet printing nozzle but on dispensing technique and on interaction of micro-ring ridge and their drying kinetics.

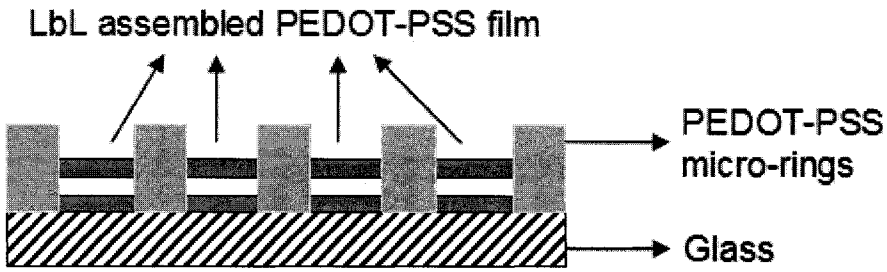

Figure 5.32 Cross-section of LbL/Micro-ring devices used for sheet resistance measurement

Poly (sodium 4-styrenesulfonate) (PSS, Molecular weight (Mw) 70,000) and Poly (allylamine hydrochloride) (PAH, Mw 70,000) were purchased from Aldrich. PSS acts as the polyanion and PAH as polycation in the alternate LbL self-assembly process. Alternate layers of $(PSS/PAH)_5/(PEDOT\text{-}PSS/PAH)_{10}$ were assembled with time and concentration optimization elaborated. The precursor layers ensure uniform deposition of polymer sensing film on glass substrate. The assembly was initiated by dipping glass slides in PAH solution followed by rinsing in DI water and then drying. This is followed by dipping in PEDOT-PSS solution followed by rinsing in DI water and drying. All the assembly was performed with polyion aqueous solutions of 3 mg/mL concentration and at pH of 6.5 when all the components are strongly charged.

Silver quartz crystal microbalance (QCM) resonators (10 MHz resonant frequency) were used for monitoring and optimizing the assembly process. Change in the resonant frequency was observed using the QCM and the Sauerbrey equation was used to

correlate change in frequency to the change in mass and thickness of the self-assembled films.

PEDOT-PSS was also inkjet printed, LbL assembled and spin-coated on the glass substrate to compare the effect of fabrication techniques on the sheet resistance, sensitivity, response time, recovery time and degradation of the humidity sensors.

5.3.2.2 Characterization of humidity sensor

Controlled humidity chamber was used to characterize the electrical properties as a function of percentage relative humidity. Pre-calibrated humidity meter model 810 bought from Indoor Health, Inc, was used in the chamber to measure the relative humidity which is varied from 50% to 90%. After testing the device, the sample was stored in dry environment. The change in sheet resistance, sensitivity, response time, recovery time and degradation of the polymer sensors were measured.

The change in the sheet resistance of the LbL assembled layer was monitored for each of these devices as the relative humidity was varied. The sensitivity of the sensor was defined by the percent change in sheet resistance per 5% change in the humidity. The response time was the time taken by the sensor to show the variation in sheet resistance after 5% change in relative humidity. The recovery time of the sensor was found to be one of the most important parameter. If the polymer was not given enough recovery time during testing it showed large variations in the sheet resistance values. The degradation of the sensing film is defined as change in baseline resistance of the device versus time. The change in baseline resistance was monitored before every testing. Baseline resistance is established at humidity present in ambient. The experimental error for change in sheet resistance measurement of the sensors is taken as 5%.

The ATR-IR spectroscopic measurements were performed using a Thermo Nicolet Nexus 470 FTIR equipped with ZnSe ATR crystal. The spectrometer is fitted with a DTGS-KBr detector and all ATR-IR spectra are calculated from 512 scans at 4 cm^{-1} resolution. Moisture absorbed by the PEDOT-PSS layer is observed through the peaks in ATR-IR spectrum in order to study the sensing mechanism.

5.3.2.3 Results and discussion

The change in sheet resistance was measured when the sensor was exposed to varying humidity. The experimental results showed that the sheet resistance of polymer sensors fabricated using PEDOT-PSS reduced with the increase in relative humidity (%).

This is attributed to a stronger screening effect between counter ions and charge carriers that reduce the Coulomb interaction between positively charged PEDOT and negatively charged PSS dopant which enhances the hopping rate.

The layer-by-layer assembly on the inkjet printed micro-ring platform technique for fabrication of PEDOT-PSS humidity sensors enabled the greater surface area for enhancing the sensitivity of the sensor. The sheet resistance of the sensor decreased when the sensor was exposed to humidity. The variation of sheet resistance with humidity was examined after exposing the samples for one, two and three days respectively as shown in Figure 5.33. The sensitivity of the sensor for 5% change in relative humidity was measured to be 12.03%. The response time and recovery time of the device was measured as 55 sec and 93 sec, respectively. The change in the base resistance was measured as 8.18% per day.

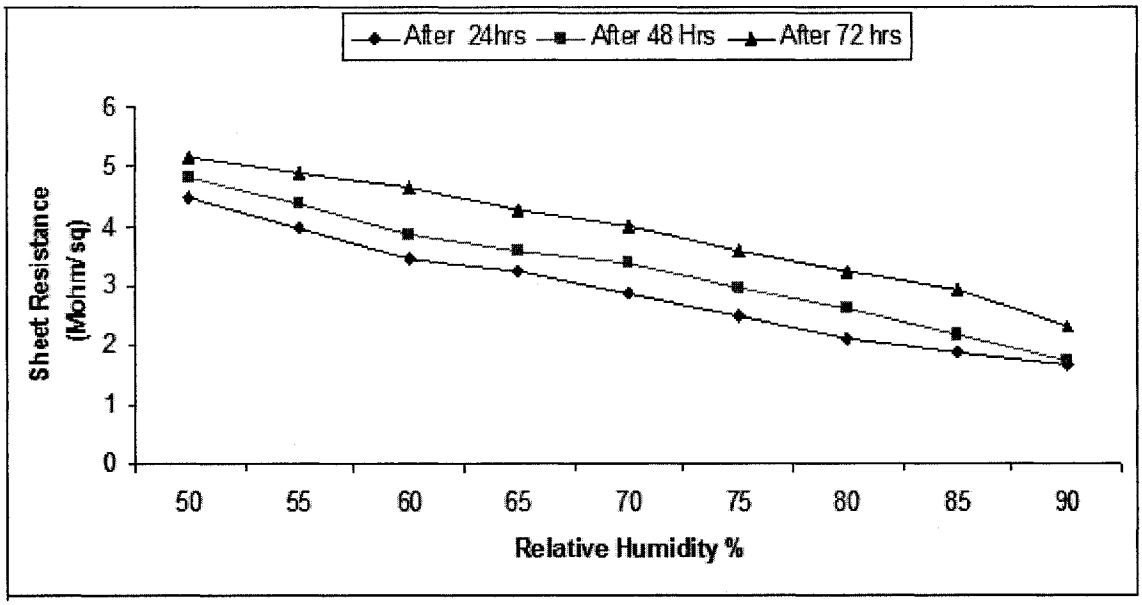

Figure 5.33 Variation of sheet resistance versus humidity for LbL assembled film over inkjet printed micro-rings

Figure 5.34 shows the variation of sheet resistance with respect to change in relative humidity for inkjet printed PEDOT-PSS sensors after one, two and three days.

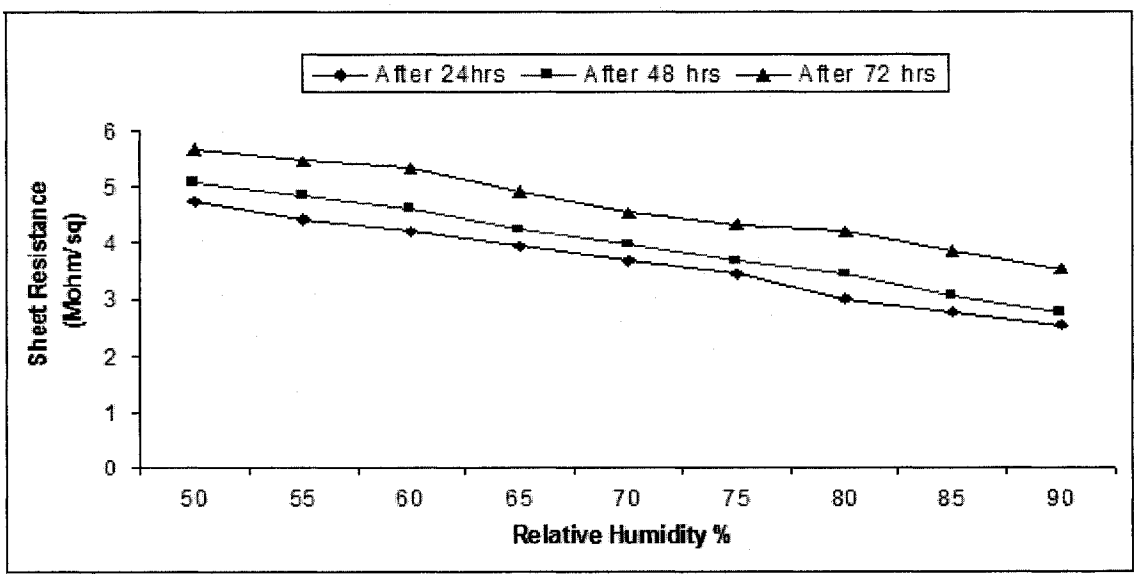

Figure 5.34 Variation of sheet resistance versus humidity from an inkjet printing based PEDOT-PSS sensor

The response time and recovery time of the device was measured to be 75 sec and 136 sec, respectively. The sensitivity for the inkjet printed sensor was measured to be 7% and the baseline drift was measured at 13.2% per day.

Figure 5.35 shows the variation of sheet resistance versus relative humidity for LbL-based PEDOT-PSS sensors. The response time for sensing 5% increase in relative humidity was measured to be about 45 sec and the recovery time was measured to be 70 sec.

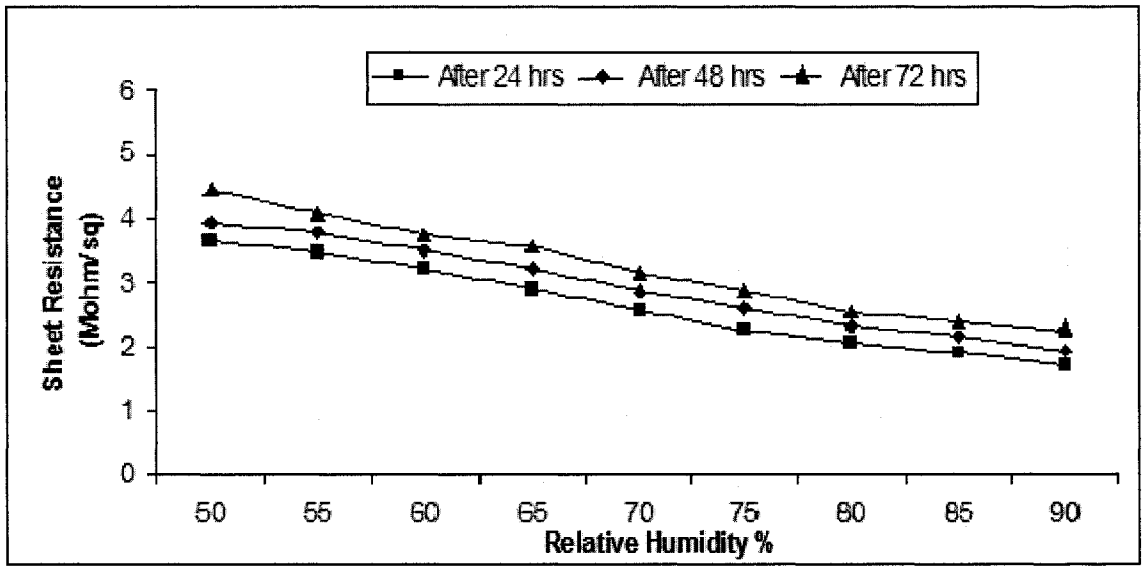

Figure 5.35 Variation of sheet resistance versus humidity for LbL based PEDOT-PSS sensor

The sensitivity for the LbL based sensor was measured at 9% and the baseline drift was measured to be 10.4% per day. The LbL-based device showed consistent response when exposed to humidity.

Figure 5.36 shows the variation of sheet resistance with respect to change in relative humidity of the spin-coated device after one, two and three days. The response

time and recovery time for spin coated devices was measured to be 90 sec and 150 sec, respectively. The sensitivity for the spin coated sensor was measured to be 5.2% and the baseline drift was measured to be 17.6% per day.

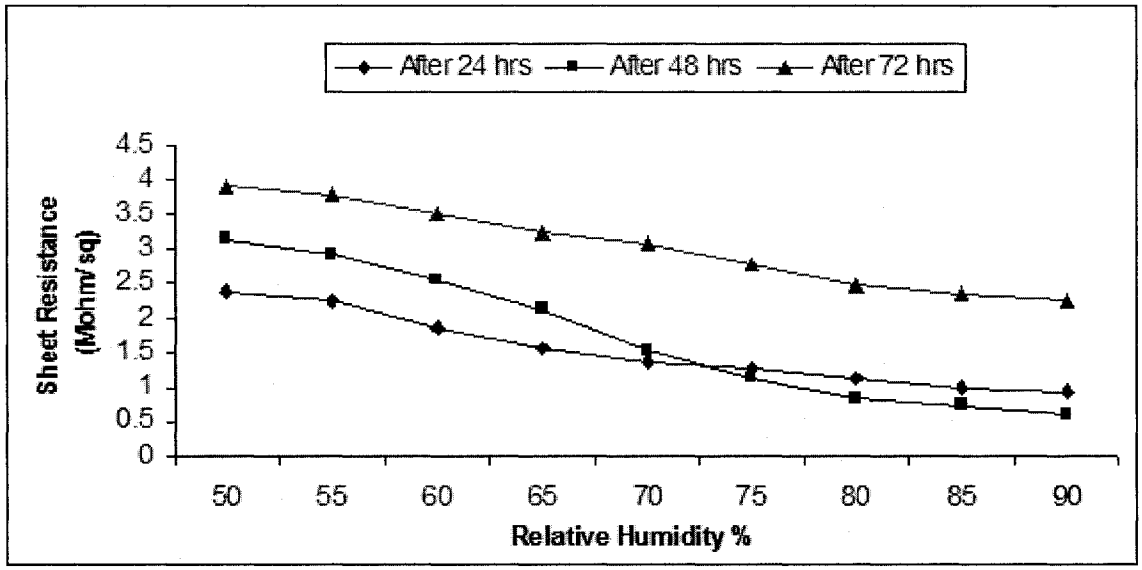

Figure 5.36 Variation of sheet resistance versus humidity from a spin coating PEDOT-PSS based sensor

The change in sheet resistivity ΔR/R for PEDOT-PSS based LbL/micro-ring, inkjet printed, LbL assembled and spin coated sensors is shown in Figure 5.37. The LbL/micro-ring technique showed highest sensitivity as compared to other thin film deposition techniques. This is attributed to larger surface sensing area provided by micro-rings for ultra-thin self-assembled films of polyelectrolytes. Increased polymer density at the ridge of the micro-ring and interconnection between the micro-rings contribute to the enhanced sensing.

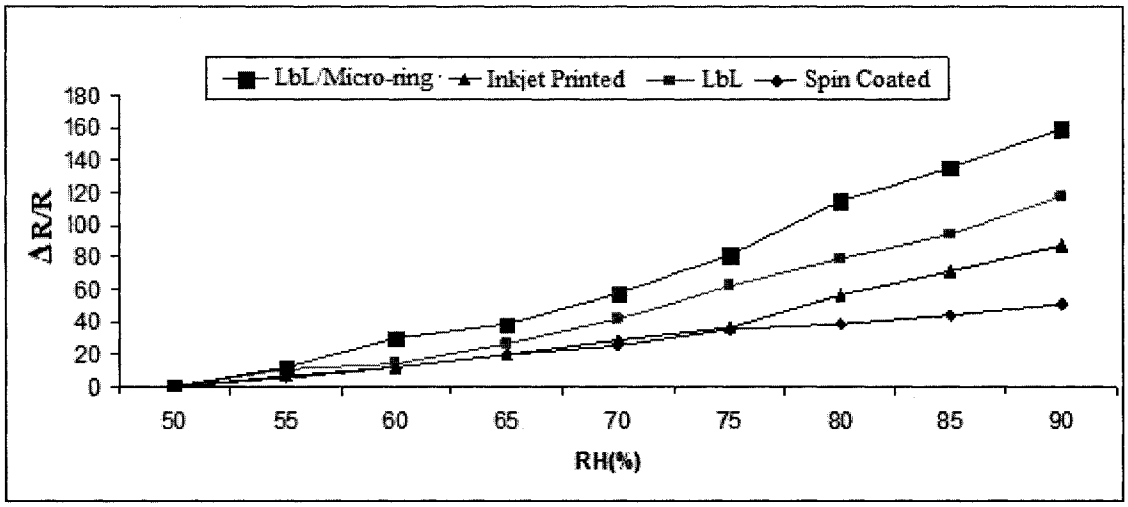

Figure 5.37 Change in sheet resistivity for PEDOT-PSS based sensors

To study the degradation of the PEDOT-PSS-based devices, they were exposed to an open environment for 10 days. The relative humidity of the environment was fixed at 50%. The total degradation of the device was 26%. These devices were also exposed to air after testing the device at 90% humidity. Figure 5.38 shows the degradation of the PEDOT-PSS based humidity sensor at 50% and 90% relative humidity.

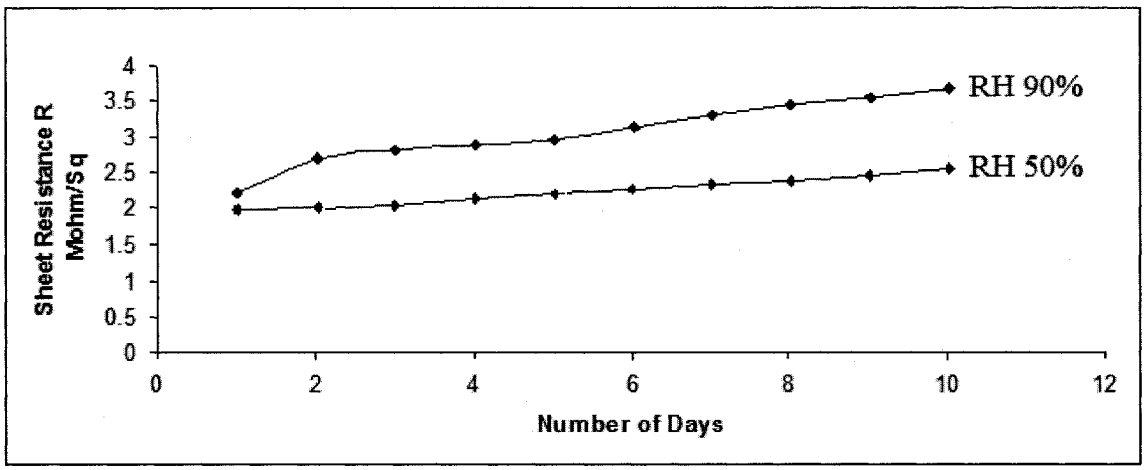

Figure 5.38 Device degradation of PEDOT-PSS at 50% and 90% relative humidity

To study the sensing mechanism of PEDOT-PSS after humidity absorption, attenuated total reflection-infra red (ATR-IR) spectroscopy was used. Figure 5.39 shows the ATR-IR spectrum of the polymer after humidity absorption for 20 seconds.

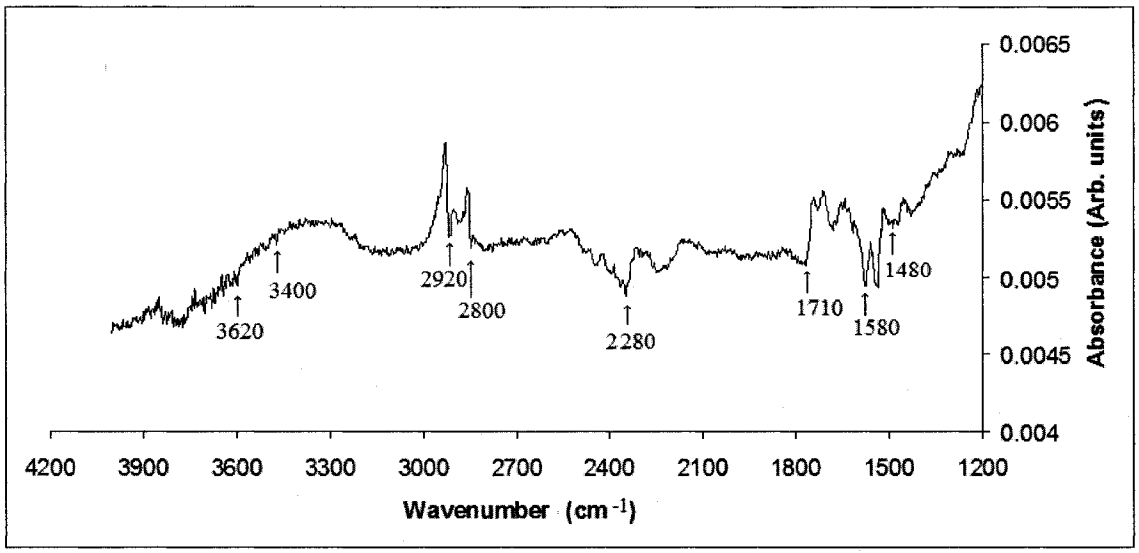

Figure 5.39 ATR-IR spectra for PEDOT-PSS after humidity absorption

The detailed peak information is listed in Table 5.2.

Table 5.2 ATR-IR spectroscopic peaks of PEDOT-PSS after moisture absorption

Wavenumbers (cm^{-1})	**Significant Modes**
1480-1500	Benzoid ring
1580, 2280	C=C bond stretching
1710	C=O bond stretching
2800-2920	C-H bond stretching
3500-3650	O-H bond vibrations

Modes have been assigned to various peaks. Peak at 1480 cm^{-1} is due to the benzoid ring. Peak at 1580 cm^{-1} and 2280 cm^{-1} are associated with carbon – carbon double bond stretching. Peak at 1710 cm^{-1} is associated with strong carbonyl absorbance which is attributed to the oxidation of polymer. Two peaks at 2800 cm^{-1} and 2920 cm^{-1} correspond to carbon – hydrogen bond stretching. Two peaks at 3400 and 3620 cm^{-1} shows oxygen – hydrogen bond vibration.

Figure 5.40 compares the performance of PEDOT-PSS-based humidity sensors fabricated by different techniques.

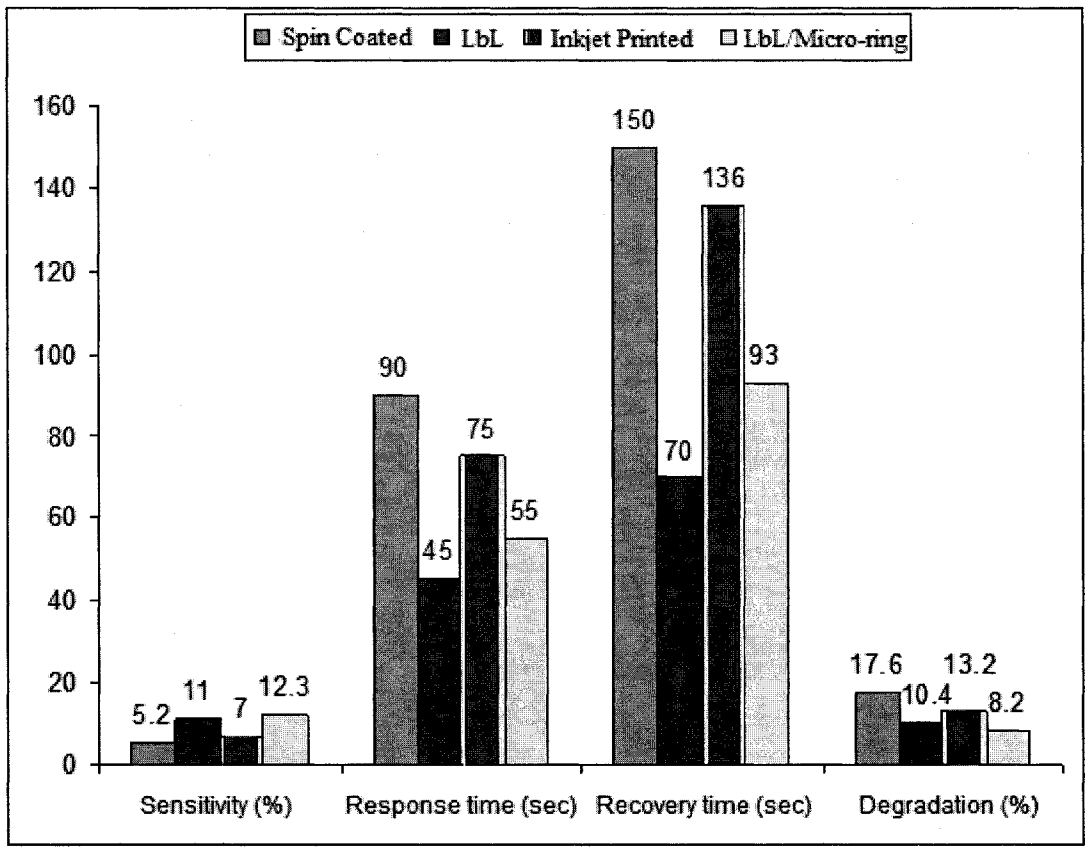

Figure 5.40 Comparison of PEDOT/PSS sensor performance

From the chart above, it can be inferred that the devices fabricated by LbL/micro-ring technique have higher sensitivity and lower degradation with time as compared to other fabrication techniques. Whereas LbL based devices have shorter response and recovery time as compared to other fabrication techniques.

5.3.3 Micro-ring Array for Vertical Channel Field Effect Transistor

5.3.3.1 Design and fabrication of vertical channel micro-ring FETs

Step 1: Cleaning/Plasma Treatment

ITO coated PET flexible substrates were used for the fabrication of vertical FETs. ITO film which acts as a drain for VFET had a thickness of 120 nm and resistivity of 10 Ωcm, and PET had a thickness of 200 μm. ITO patterned substrate was sonicated in DI water, acetone and IPA for 10 min each. Finally the substrate was rinsed in DI water followed by drying with nitrogen gun. After cleaning the ITO substrate the next important step for improving the work-function of ITO is oxygen plasma treatment. Since oxygen is electronegative; it renders negative charge to the surface of ITO which may cause depletion of electrons below the ITO surface which induces band bending and higher work function. Moreover the negative charge on the ITO surface helps layer-by-layer assembly of PAH/PSS/PAH/SiO_2. Thus the ITO substrate is loaded into the top chamber of the Micro-RIE unit. After pumping down the chamber to 50 mtorr, the RF power was turned on (200 W), establishing a pale blue plasma. The inlet valve on the chamber was then slowly opened to let in a small stream of oxygen (5.5 sccm), turning the plasma pink. The substrate was exposed to oxygen plasma for 3 min. After 3 min, the RF power was turned off, the chamber was vented and the substrate was removed.

Step 2: Source/Drain Insulation

Layer-by-layer self-assembly of 3 bilayers of PAH/PSS which act as precursor layer were deposited on top of ITO surface. This was followed by 5 bilayers of PAH/SiO_2 as shown in Figure 5.41. SiO_2 nanoparticles have a diameter of 7nm. The total thickness of 8 bilayers is about 50 nm. These bilayers act as insulation between source and drain.

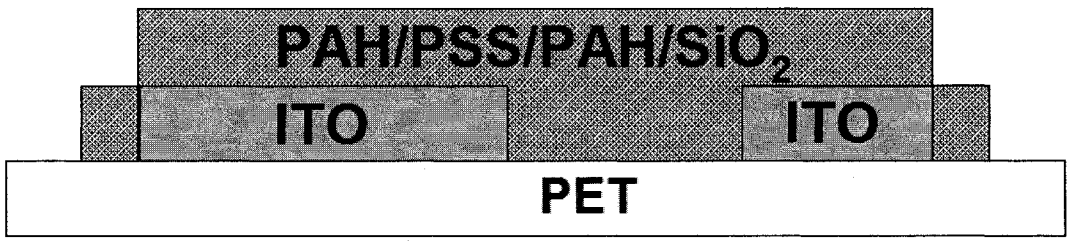

Figure 5.41 Schematic of SiO_2 nanoparticle insulating layer over ITO

Step 3: Inkjet Printing of Micro-rings for Source

Inkjet printed micro-rings of PEDOT-PSS were dispensed such that the space between four drops is minimum. The thickness of the outer ridge is about 130 nm as shown in Figure 5.42.

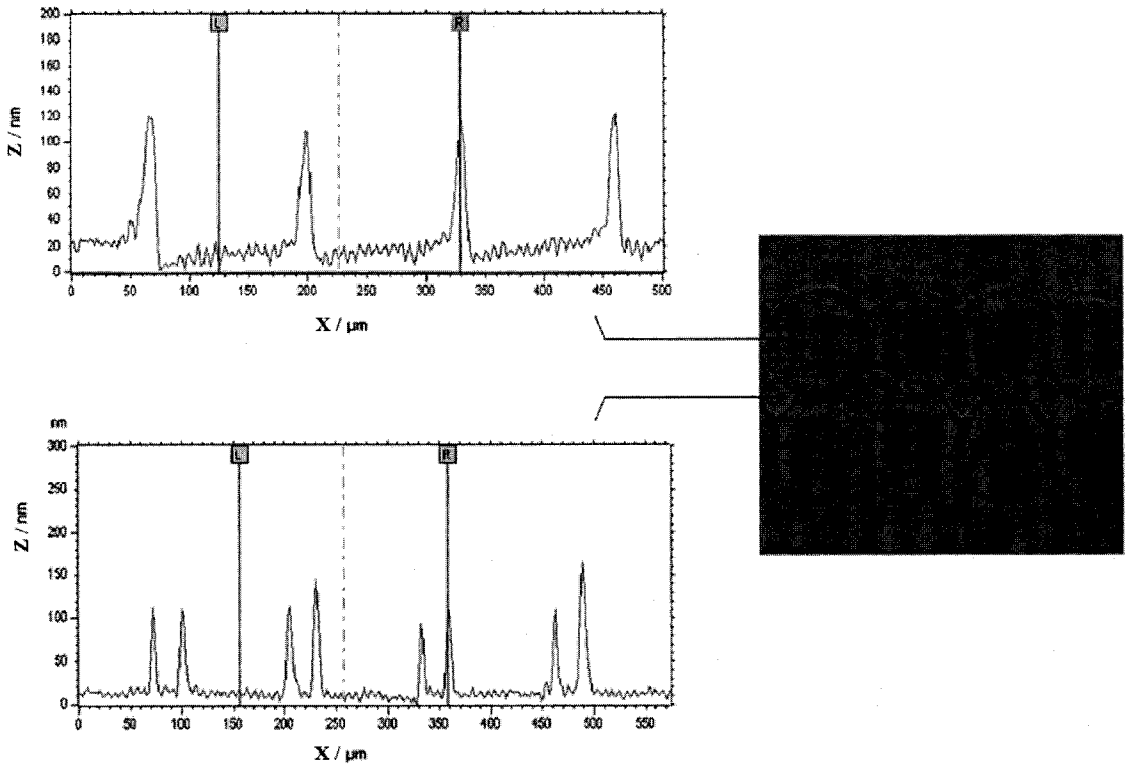

Figure 5.42 Surface profile of inkjet printed micro-ring spacers

Figure 5.43 shows the schematic of the source patterning using micro-ring spacers.

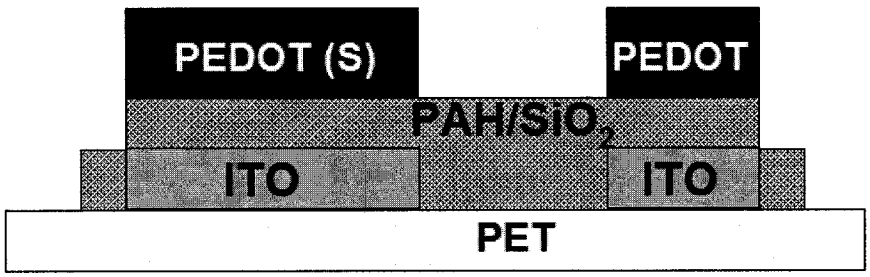

Figure 5.43 Schematic of micro-ring spacers for source

Step 4: RIE Plasma Etching of SiO_2

The SiO_2 insulating layer between the micro-ring spacers was etched using SF_6 plasma in RIE chamber. The parameters used for etching were 60sec at a pressure of

100mTorr and power of 200W. Figure 5.44 shows the optical image of inkjet printed micro-ring spacers before and after SF_6 etching. It also shows that PEDOT-PSS rings act as mask in blocking the insulation layer below them.

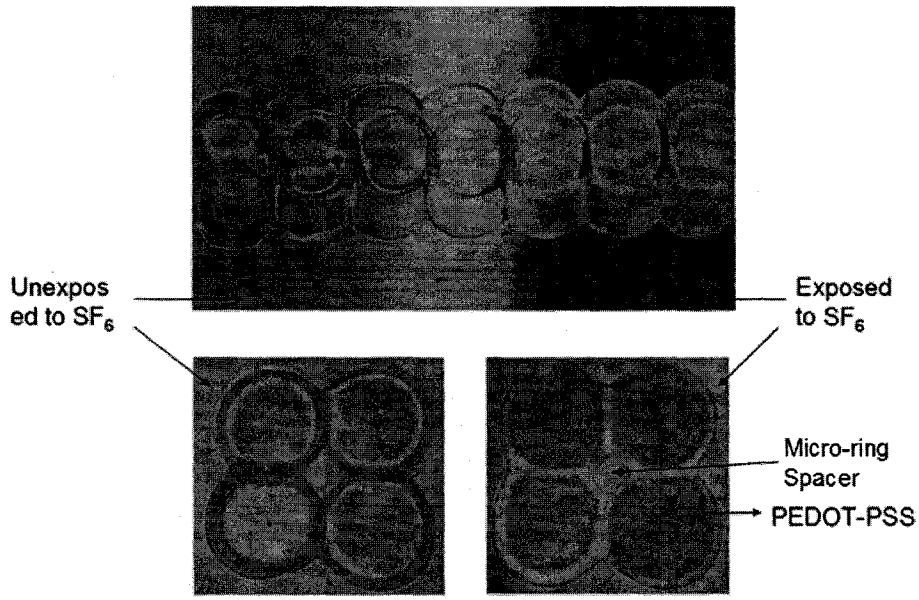

Figure 5.44 Optical image of SF_6 plasma etching on micro-rings and SiO_2

Figure 5.45 shows the schematics of the SF_6 etched SiO_2 insulating layer between the micro-ring spacers. The PEDOT-PSS micro-rings act as a mask for protecting the insulation of source and drain. These spacers are used as channels and the thickness of the insulating layer determines the channel length.

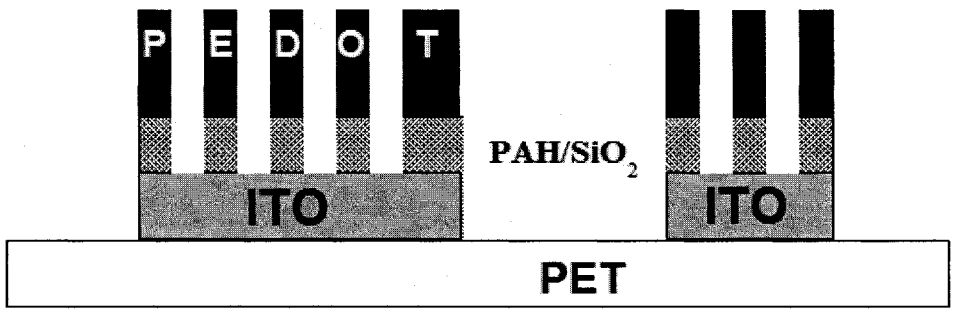

Figure 5.45 Schematic of SF_6 etched SiO_2 for channel

Step 5: Spin Coating of Channel Material

A 0.6% solution of MEH-PPV in p-xylene is prepared by sonicating the solution for more than 3 hrs at 50°C. Approximately 1 ml of MEH-PPV was dispensed on inkjet printed micro-rings and spun at speed of 2500 rpm for 30 sec which resulted in 80 nm thick film as shown by schematic in Figure 5.46. The samples are kept in vacuum for 15 hrs for complete drying of the MEH-PPV layer. Thus MEH-PPV acts as a channel material for vertical FET. It is in contact with both source (micro-rings) and drain (ITO). MEH-PPV exhibits ambipolar behavior, but it acts more as a p-type than n-type material.

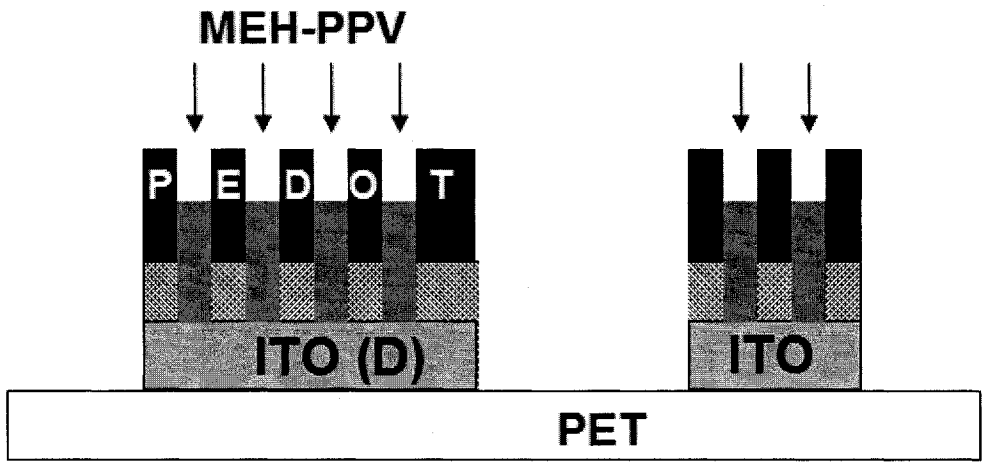

Figure 5.46 Schematic of spin coated MEH-PPV channel

Step 6: Deposition of Gate Dielectric

Poly-4-vinylphenol (PVP) acted as gate dielectric layer. PVP was spin coated from a solution of isopropyl alcohol which resulted in a thickness of 150 nm. Figure 5.47 shows the schematic of PVP dielectric layer on top of micro-rings and channel material. The dielectric constant of PVP is about 2.8.

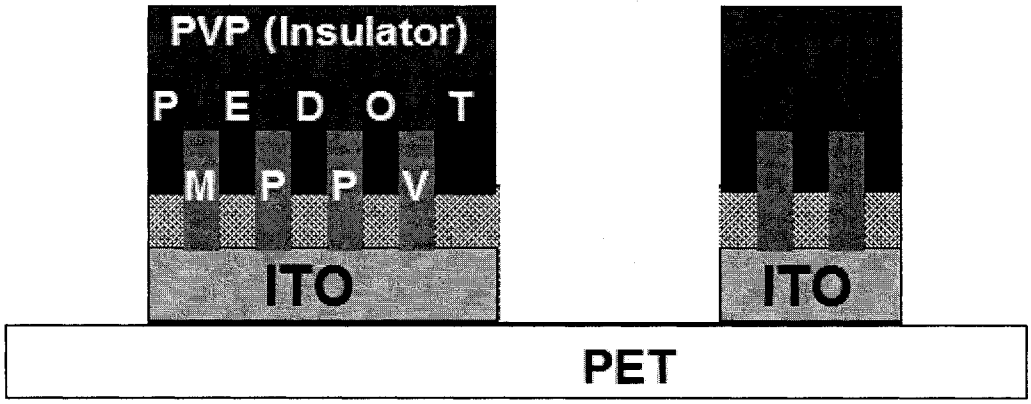

Figure 5.47 Schematic of PVP gate dielectric on top of micro-rings and channel

Step 7: Gate Deposition

PEDOT:PSS was used as gate material for vertical FET. Four layers of PEDOT:PSS were inkjet printed on top of the insulator. The thickness of gate was around 200 nm. Conductive epoxy was used to make contacts to gate. The other contacts to source and drain were made by exposing them to oxygen plasma in RIE chamber. Figure 5.48 shows the schematic of the final device.

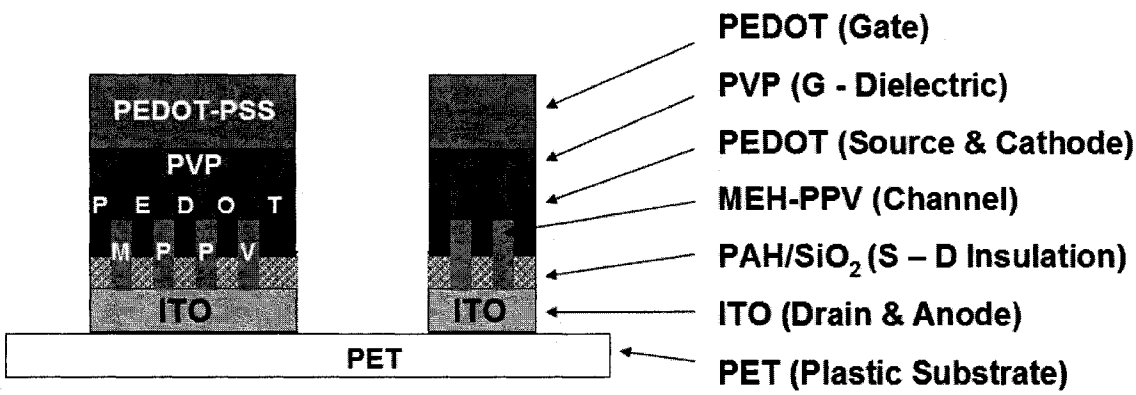

Figure 5.48 Schematic of final vertical FET device

5.3.2 Results and Discussion

Figure 5.49 shows the output characteristics of the MEH-PPV based 3×4 array of vertical channel FETs. The gate voltages were varied from 0 to -8 V.

In the linear region, the drain to source potential V_{ds} is smaller as compared to the sum of the gate's built-in potential V_{bi} and the gate to source potential V_{gs}. Thus, the drain current I_d, increases linearly with the drain voltage V_d according to equation 5.1 [118].

$$I_d = \frac{Z}{L}\mu C_i (V_g - V_T) V_d \tag{5.1}$$

where Z is the channel width, L is the channel length, μ is the charge carrier mobility (cm^2/Vs), C_i is the capacitance of the insulator per unit area, typically reported in nF/cm^2, V_g is the applied gate voltage and V_T is the threshold voltage.

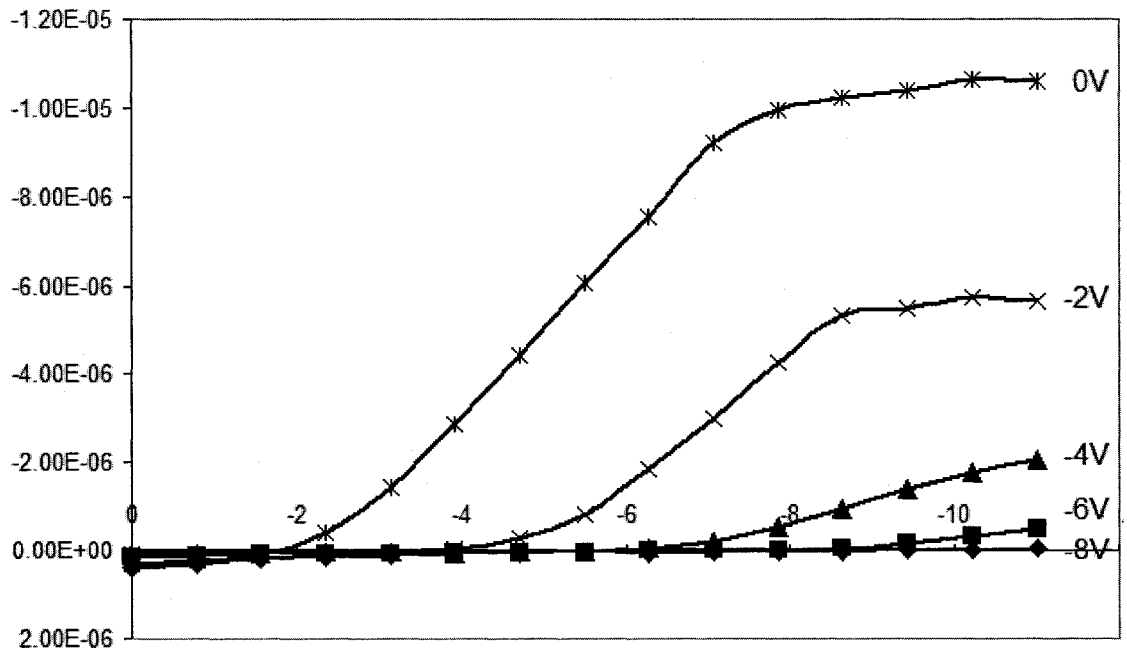

Figure 5.49 $I_d - V_d$ characteristics of vertical channel polymer FET

In the saturation region, increasing V_d beyond the cut-off point i.e., $V_d > V_{dsat}$ causes the channel to deplete more and more and I_d curves become saturated and the drain current does not increase further. The saturation current I_{dsat}, can be described by equation (5.2) [115].

$$I_{dsat} = \frac{Z}{2L}\mu C_i (V_g - V_T)^2 \tag{5.2}$$

However, with negative increase in gate voltage, the drain current decreases. This is opposite to the conventional p-channel MOSFET behavior. This phenomena is thought to be due to the fact that when negative gate voltage is applied, the holes from PEDOT:PSS source (micro-rings) get attracted on the upper part of the ring. Thus on the lower part were the source and channel are in contact, the carrier concentration decreases, which increases the depletion width. With increasing the negative gate voltage the depletion width between source and channel keeps on increasing due to accumulation of holes at the interface of PEDOT:PSS (source) and PVP (gate dielectric) and depletion of holes at the interface of PEDOT:PSS (source) and MEH-PPV (channel) thus reducing the drain current.

Figure 5.50 shows the I_{dsat} - V_g characteristics of vertical channel FET. The threshold voltage V_T, defined as the minimum gate voltage required to induce the channel in a FET, is extracted from the intercept of a line drawn through the linear region of the $I_{dsat}^{1/2}$ vs. V_g plot shown in the inset of Figure 5.49. The values were calculated at drain voltage of -10 V as the device shows saturation in this region. The point of intersection gives the threshold voltage V_T of -7 V.

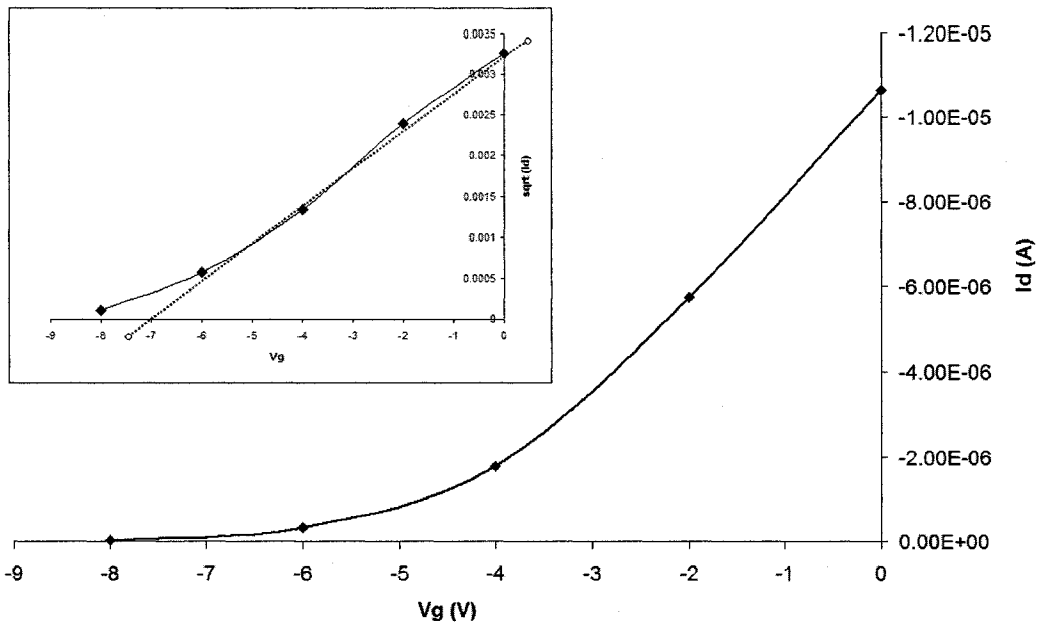

Figure 5.50 $I_{dsat} - V_g$ characteristics of vertical channel FET (inset: $I_{dsat}^{1/2} - V_g$)

The mobility value was extracted from equation 5.2 where Z/L ratio is 5000, C_i is 1.77×10^{-8} F/cm^2 for 150 nm gate-dielectric, gate voltage of 0V and threshold voltage of -7V. The extracted value of mobility is 4.6×10^{-3} cm^2/Vs. The I_{on} / I_{off} current ratio for the device is of the order of 10^3.

Thus, we have demonstrated vertical channel FETs using inkjet printed micro-rings as source and the inner part of these overlapping micro-rings as channel. These devices can be further optimized in future for integrated vertical FET with polymer LEDs, where the electroluminescent channel material can act as inner layer between anode and cathode. Thus gate can have control of the LED.

CHAPTER 6

CONCLUSION AND FUTURE WORK

6.1 Conclusion

A novel technique for fabricating micro-rings using drop-on-demand inkjet printing has been developed by exploiting the coffee drop effect. The drop dispensing parameters and substrate temperatures were modified to influence the drop dynamics in such a way that using a same nozzle size both diameter and height of the micro-rings can be varied. Micro-rings of diameter varying from 100 μm – 700 μm, and heights varying from 100 nm - 10 μm have been realized.

Factors affecting the transport phenomena of the solute particles moving towards the periphery of the micro-ring after being dispensed from the piezoelectric based drop-on-demand inkjet printing system have been considered for the fabrication of the micro-rings. Two dispensing techniques used for varying the diameter of height of micro-rings are named as "instant dispensing" and "dispense and dry." A model has been developed in the form of flow chart and by varying the parameters such as frequency of drops dispensed, substrate temperature and number of drops, desired micro-ring structures of varying diameter and height can be fabricated.

These micro-rings found potential application in polymer light emitting diodes, humidity sensor and vertical field effect transistors. The use of micro-rings as a single

pixel micro-rings were used for improving the resolution of the polymer light emitting diodes to more than 200 pixels/inch.

These micro-rings found potential application in polymer light emitting diodes, humidity sensor and vertical field effect transistors. The single pixel micro-rings were used for improving the resolution of the polymer light emitting diodes to more than 200 pixels/inch. Sensitivity enhancement and lower degradation was reported for PEDOT:PSS based humidity sensor were micro-rings were used as a platform for layer-by-layer self assembled nano films. These devices were compared to devices fabricated by other techniques such as spin coating, inkjet printing and layer-by-layer assembly. Micro-rings were also used during the fabrication of vertical channel field effect transistors where outer periphery of the micro-rings was used as source and the inner etched surface between the adjacent drops was used for channel material. The extracted value of mobility was 4.6×10^{-3} cm^2/Vs and the I_{on} / I_{off} current ratio for the device is of the order of 10^3.

MEH-PPV is an electroluminescent polymer which was used for both polymer light emitting diodes and vertical channel field effect transistors. The degradation of this polymer affects the device efficiency to a great extent. Thus degradation of this polymer was studied using capacitance – voltage and ATR-IR spectroscopy.

6.2 Future Work

Besides further improving the performances of the devices such as, polymer light emitting diodes, humidity sensors and polymer vertical channel field effect transistors, micro-rings can be applied for various other applications in diverse fields.

1. **Micro-rings For Cantilever Sensor Arrays**

Micro-rings can be inkjet printed on top of cantilever and then made empty using RIE. Each micro-ring (Figure 6.1) can then be filled with different sensing material. So instead of using the fabricated device for the detection of single or few gases, many gases or biomaterials can be detected simultaneously.

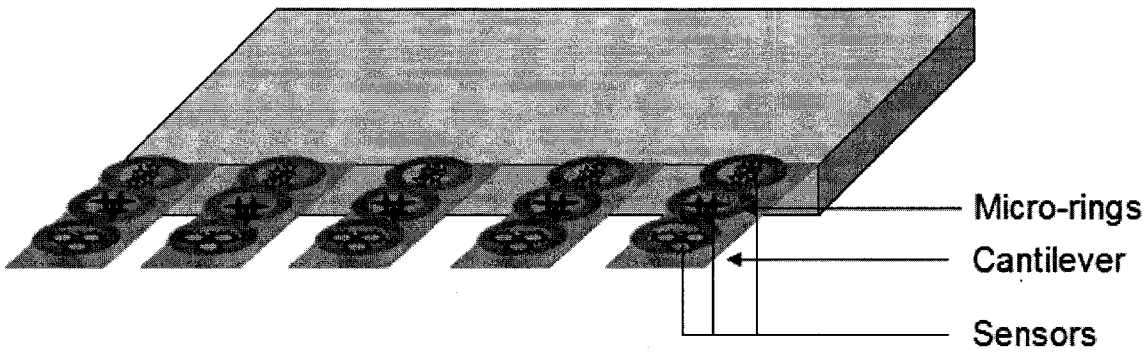

Figure 6.1 Micro-ring array for detection of various gases/biomaterials using cantilever sensor

2. **Concentric Micro-rings For Polymer Field Effect Transistors**

Concentric micro-rings as shown in Figure 6.2 can be inkjet printed using both techniques i.e. "instant dispensing" for the outer ring and "dispense and dry" for the inner ring. Metal can be thermally evaporated to act as source and drain material, whereas inkjet printed ring can act as channel. The width of the channel can be varied from 5 μm to 50 μm.

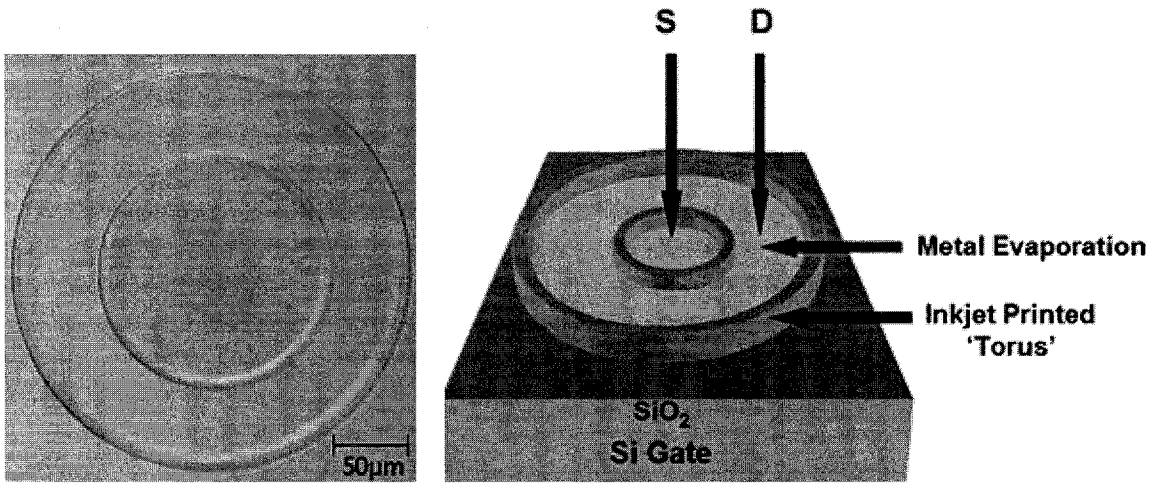

Figure 6.2 Concentric micro-ring for polymer field effect transistors

3. Micro-ring Wells for Cell Culture Plates

Micro-ring array can be inkjet printed to form different cell culture plates as shown in Figure 6.3. The cell culture plates available in the market are quite big and expensive. They require a lot of media and cells and thus leads to wastage of cells and media. Using the micro-ring plates, very less media and cells will be required. Moreover, cells can be inkjet printed inside these micro-rings thus proving to be an inexpensive technique.

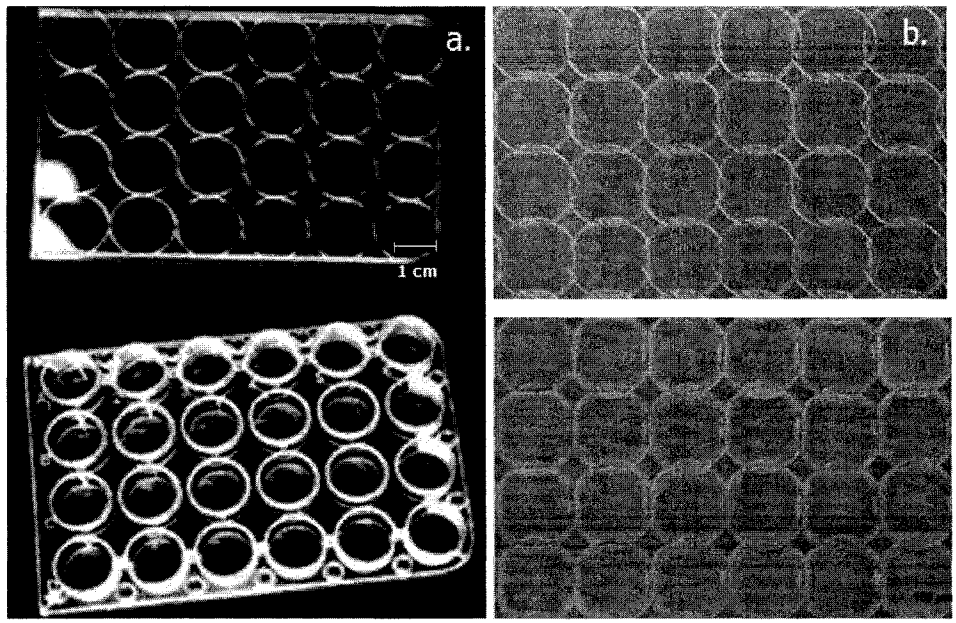

Figure 6.3 Cell culture plates a) commercially available b) inkjet printed in lab

4. Micro-ring Scaffolds For Tissue Culture

Figure 6.4 shows the micro-ring arrays fabricated one on top of the other in the form of scaffolds. These scaffolds can be used for the growth of tissues. The desired cells can be cultured in these scaffolds and thus their growth can be controlled by the shape of the scaffolds.

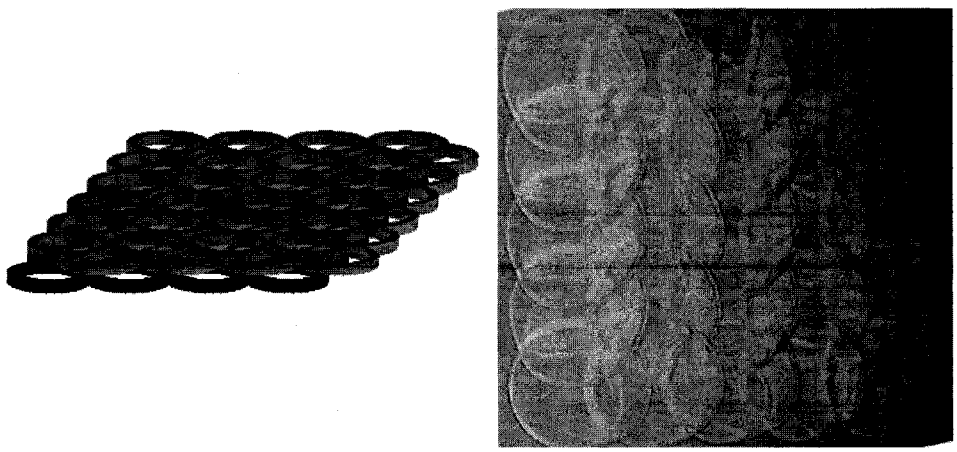

Figure 6.4 Inkjet printed micro-ring scaffolds for tissue culture

REFERENCES

[1] W. M. Moreau, *Semiconductor Lithography*, Plenum Publishing Co., New York, (1988).

[2] T. Theis, "The Future of Interconnection Technology," *IBM Journal of Research. & Development.* 44, no. 3, p 379 (May 2000).

[3] T. Ueki, "Requirements for large-sized high-resolution TFT-LCDs," *Journal of the Society for Information Display* 9, no. 3, p 151-154 (2001).

[4] F. Garnier, R. Hajlaoui, A. Yasser, and P. Srivastava, "All Polymer Field-Effect Transistors Realized by Printing Techniques," *Science* 265, p 1684-1686 (1994).

[5] J. H. Burroughes, C. A. Jones, and R. H. Friend, "New Semiconductor Device Physics in Polymer Diodes and Transistors," *Nature* 335, p 131-137 (1988).

[6] Z. Bao, A. Dodabalapur, and A. Lovinger, "Soluble and Processable Regioregular Poly(3-hexylthiophene) for Thin Film Transistor Applications with High Mobility," *Applied Physics Letters* 69, p 4108 (1996).

[7] A. Dodabalapur, L. Torsi, and H. E. Katz, "OrganicTransistors: Two-Dimensional Transport and Improved Electrical Characteristics," *Science* 268, p 270-271 (1995).

[8] J. M. Shaw and P. F. Seidler, "Organic Electronics: Introduction," *IBM Journal of Research & Development* 45, (2001).

[9] K. F. Teng and R. W. Vest, "Application of ink jet technology on photovoltaic metallization," *IEEE Electron Device Letters* 9, p 591-595 (1998).

[10] M. Ghannam, S. Sivoththaman, J. Poortmans, J. Szlufcik, J. Nijs, R. Mertens, and R. V. Overstraeten, "Trends in industrial silicon solar cell processes," *Solar Energy* 59, p 101-110 (1997).

[11] B. J. De Gans, E. Kazancioglu, W. Meyer, U. S. Schubert, "Ink-jet Printing Polymers and Polymer Libraries Using Micropipettes," *Macromolecular Rapid Communications* 25, no. 1, p 292-296 (Jan 2, 2004).

[12] R. D. Deegan, O. Bakajin, T. F. Dupont, G. Huber, S. R. Nagel, and T. A. Witten, "Capillary flow as the cause of ring stains from dried liquid drops," *Nature 389*, p 827-829 (1997).

[13] R. D. Deegan, O. Bakajin, T. F. Dupont, G. Huber, S. R. Nagel, and T. A. Witten, "Contact line deposits in an evaporating drop," *Physical Review E 62*, p 756-765 (2000).

[14] R. D. Deegan, "Pattern formation in drying drops," *Physical Review E 61*, p 475-485 (2000).

[15] B. J. Gans and U. S. Schubert, "Inkjet printing of well defined polymer dots and arrays," *Langmuir* 20, p 7789-7793 (2004).

[16] C. K. Chiang, C. R. Fincher, Y. W. Park, A. J. Heeger, H. Shirakawa, E. J. Louis, S. C. Gau and A. G. MacDiarmid, "Electrical Conductivity in Doped Polyacetylene," *Physical Review Lett*ers 39, p 1098–101 (1977).

[17] G. Konig and G. Stollhoff, "Why polyacetylene dimerizes: Results of ab initio computations," *Physical Review Lett*ers 65, p 1239–42 (1990).

[18] A. B. Kaiser, "Electronic transport properties of conducting polymers and carbon nanotubes," *Reports on. Progress in Physics* 64, p 1-49 (2001).

[19] S. K. M. Jönsson, W. R. Salaneck, and M. Fahlman, "Spectroscopy of ethylenedioxy-thiophene-derived systems: from gasphase to surfaces and interfaces found in organic electronics," *Journal of Electron Spectroscopy and Related Phenomena* 137–140, p 805–809 (2004).

[20] S. Timpanaro, M. Kemerink, F. J. Touwslager, M. M. Kok, and S.Schrader, "Morphology and conductivity of PEDOT/PSS films studied by scanning–tunneling microscopy," *Chemical Physics Letters* 394, p 339–343 (2004).

[21] J. Y. Kim, J. H. Jung, D. E. Lee, and J. Joo, "Enhancement of electrical conductivity of poly(3,4-ethylenedioxythiophene)/poly(4-styrenesulfonate) by a change of solvents," *Synthetic Metals* 126, p 311–316 (2002).

[22] A. Aleshin, R. Kiebooms, R. Menon, A. J. Heeger, "Electronic transport in doped poly(3,4-ethylenedioxythiophene) near the metal-insulator transition," *Synthetic Metals*, 90, p 61-68 (1997).

[23] A. F. Mott, E. Davis, "Electronic processes in non-crystalline materials," Oxford: Clarendon Press, (1979).

[24] P. J. Phillips, "Polymer crystals," *Reports on Progress in Physics* 53, p 549–604 (1990).

[25] M. P. Stevens, Polymer Chemistry: an Introduction 2nd edn (Oxford: Oxford University Press), p 91 (1990).

[26] F. W. Billmeyer, Textbook of Polymer Science 3rd edn (New York: Wiley) p 277 (1984).

[27] J. P. Pouget , Z. Oblakowski, Y. Nogami, P. A. Albouy, M. Laridjani, E. J. Oh, Y. Min, A. G. MacDiarmid, J. Tsukamoto, T. Ishiguro, and A. J. Epstein, "Recent structural investigations of metallic polymers," *Synthetic Metals* 65, p 131–40 (1994).

[28] D. Bloor, "Developments in Crystalline Polymers" *Applied Science*, p 151–93 (1882).

[29] K. Ehinger and S. Roth, "Non-Solitonic Conductivity in Polyacetylene," *Philosophical Magazine* B 53, p 301–20 (1986).

[30] S. Roth and H. Bleier, "Solitons in polyacetylene ," *Advances in Physics* 36, p 385–462 (1987).

[31] A. J. Heeger, S. Kivelson, J. R. Schrieffer, and W. P. Su, "Solitons in conducting polymers," *Reviews of Modern Physics* 60, p 781–850 (1988).

[32] S. Kivelson, "Electron Hopping Conduction in the Soliton Model of Polyacetylene," *Physical Review Letters* 46, p 1344–8 (1981).

[33] A. J. Epstein, H. Rommelman, R. Bigelow, H. W. Gibson, D. M. Hoffmann, and D. B. Tanner, "Role of Solitons in Nearly Metallic Polyacetylene," *Physical Review Letters* 50, p 1866–9 (1983).

[34] S. Stafstrom and J. L Bredas, "Evolution of the electronic structure of polyacetylene and polythiophene as a function of doping level and lattice conformation," *Physical Review B* 38, p 4180–91 (1988).

[35] Collin Pratt, Report on Conducting Polymers, 22nd Feb, 1996.

[36] J. Y. Kim, J. H. Jung D. E. Lee, J. Joo, "Enhancement of electrical conductivity of poly(3,4-ethylenedioxythiophene)/poly(4-styrenesulfonate) by a change of solvents," *Synthetic Metals* 126, p 311-316 (2002).

[37] W. H. Kim, A. J. Ma¨kinen, N. Nikolov, R. Shashidhar, H. Kim, Z. H. Kafafi, *Applied Physics Letters* 80, p 3844-3846 (2002).

[38] S. K. M. Jo¨nsson, J. Birgerson, X. Crispin, G. Greczynski, W. Osikowicz, A. W. D. van der Gon, W. R. Salaneck, M. Fahlman, "The effects of solvents on the

morphology and sheet resistance in poly(3,4-ethylenedioxythiophene)–polystyrenesulfonic acid (PEDOT–PSS) films ," *Synthetic Metals* 139, p 1-9 (2003).

[39] X. Crispin, S. Marciniak, W. Osikowicz, G. Zotti, A. W. D. van der Gon, F. Louwet, M. Fahlman, L. Groenendaal, F. de Schryver, W. R. Salaneck, "Conductivity, morphology, interfacial chemistry, and stability of poly(3,4-ethylene dioxythiophene)-poly(styrene sulfonate): A photoelectron spectroscopy study," *Journal of Polymer Science.*, 41, p 2561-2583 (2003).

[40] L. Groenendaal, F. Jonas, D. Freitag, H. Pielartzik, and J. R. Reynold, "Poly(3,4-ethylenedioxythiophene) and Its Derivatives: Past, Present, and Future," *Advanced Materials* 12, p 481-494 (2002).

[41] Y. Cao, Y. G, C. Zhang, .R. Menon, A. J. Heeger, "Polymer light-emitting diodes with polyethylene dioxythiophene–polystyrene sulfonate as the transparent anode," *Synthetic Metals* 87, p 171-174 (1997).

[42] H. W. Heuer, R. Wehrmann, S. Kirchmeyer, "Electrochromic Window Based on Conducting Poly(3,4-ethylenedioxythiophene)-Poly(styrene sulfonate)," *Advanced Functional Materials* 12, p 89-94 (2002).

[43] D. Nilsson, T. Kugler, P. O. Svensson, M. Berggren, "An all-organic sensor–transistor based on a novel electrochemical transducer concept printed electrochemical sensors on paper," *Sensors and Actuator, B* 86, p 193-197 (2002).

[44] M. Chen, D. Nilsson, T. Kugler, M. Berggren, T. Remonen, "Electric current rectification by an all-organic electrochemical device," *Applied Physics Letters* 81, p 2011-2013 (2002).

[45] F. Zhang, M. Johansson, M. R. Andersson, J. C. Hummelen, O. Inganas, "Polymer Photovoltaic Cells with Conducting Polymer Anodes," *Advanced Materials* 14, p 662-665 (2002).

[46] C. S. Lee, J. Y. Kim, D. E. Lee, Y. K. Koo, J. Joo, S. Han, Y. W. Beag, S. K. Koh, *Synthetic Metals*135-136, p 13–14 (2003).

[47] W. H. Kim, A. J. Ma¨kinen, N. Nikolov, N. Shashidhar, H. Kim. Z. H. Kafafi, "Molecular organic light-emitting diodes using highly conductive and transparent polymeric anodes," *Proceedings of SPIE* 4464, p 85-92 (2002).

[48] A. J. Ma¨kinen, W. H. Kim, I. G. Hill, R. Shashidhar, N. Nikolov, Z. H. Kafafi, "Hole injection energetics at highly conducting polymer anode: small molecule interfaces studied with photoemission spectroscopy," *Proceedings of SPIE* 4464, p 172-177 (2002).

[49] A. A. Argun, A. Cirpan, J. R. Reynolds, "The first truly all-polymer electrochromic devices" *Advanced Materials* 15, p 1338-1341 (2003).

[50] Y. M. Lvov, "Thin film nanofabrication by alternate adsorption of polyions, nanoparticles and proteins," Lecture notes, Louisiana Tech University.

[51] M. P. Stevens, Polymer Chemistry, 3rd Ed., Oxford University Press, New York, p 412 (1992).

[52] D. Walton and P. Lorimer, *Oxford Chemistry Primers* 85, Polymers, p 135 (2000).

[53] M. R. Nateghi, A. Bagheri, A. Massoumi and M. H. Kazemeini, "Pyrocatechol violet loaded polypyrrole modified glassy carbon electrode for the determination of copper species by anodic stripping differential pulse voltammetry. Investigation of effects of film morphology and counter ions on modified electrode characteristics," *Synthetic Metals* 96, p 209-212 (1998).

[54] T. Nagaoka, H. Nakao, T. Suyama, K. Ogura, M. Oyama and S. Okazaki, "Electrochemical Characterization of Soluble Conducting Polymers as Ion Exchangers," *Analytical Chemistry* 69, p 1030-1037 (1997).

[55] T. Shimidzu, A. Ohtani, T. Iyoda and K. Honda, "Charge-controllable polypyrrole/polyelectrolyte composite membranes: Part II. Effect of incorporated anion size on the electrochemical oxidation-reduction process," *Journal of Electroanalytical Chemistry* 224, p 123-135 (1987).

[56] J. H. Buroughes, D. D. C. Bradley, A. R. Brown, R. N. Marks, K. Mackey, R. H. Friend, R. L. Burn, and A. B. Holmes, "Light-emitting diodes based on conjugated polymers," *Nature* 347, p 539-541 (1990).

[57] R. H. Friend, R. W. Gymer, A. B. Holmes, J. H. Burroughes, R. N. Marks, C. Taliani, D. D. C. Bradley, D. A. DosSantos, J. L. Bredas, M. Logdlung, and W. R. Salaneck, "Electroluminescence in conjugated polymers," *Nature* 397, p 121 (1999).

[58] S. Forero, P. H. Nguyen, W. Brutting, and M. Schwoerer, "Charge carrier transport in poly(p-phenylenevinylene) light-emitting devices," *Phys. Chem. Chem. Phys. 1*, p 1769-1776 (1999).

[59] L. Dai, B. Winkler, L. Dong, and A. W. H. Mau, "Conjugated Polymers for Light-Emitting Applications," *Advanced Materials* 13, p 915-925 (2001).

[60] C. H. Tan, A. R. Inigo, W. S. Fann, P. K. Wei, Y. S. Huang, G. Y. Perng, and S. A. Chen, *Org. Electron.* 3, p 85 (2002).

[61] A. R. Inigo, C. H. Tan, W. S. Fann, Y. S. Huang, G. Y. Perng, and S. A. Chen, "Non-dispersive Hole Transport in a Soluble Poly(p-phenylene vinylene)," *Advanced Materials*13, p 504-508 (2001).

[62] H. Müller, F. Salhi and B. Blohorn, "Bis(arylidene)tetrathiapentalenes - Novel building blocks for extended tetrathiafulvalenes and conducting polymers," *Synthetic Metals* 84, p 455-446 (1997).

[63] S. Shaked, S. Tal, Y. Roichman, A. Razin, S. Xiao, Y. Eichen, and N. Tessler, "Charge Density and Film Morphology Dependence of Charge Mobility in Polymer Field-Effect Transistors," *Advanced Materials*15, p 913-916 (2003).

[64] Y. Shi, J. Liu, and Y. Yang, "Device performance and polymer morphology in polymer light emitting diodes: The control of thin film morphology and device quantum efficiency," *Journal of Applied Physics*87, p 4254-4263 (2000).

[65] J. Liu, Y. Shi, L. Ma, and Y. Yang, " Device performance and polymer morphology in polymer light emitting diodes: The control of device electrical properties and metal/polymer contact," *Journal of Applied Physics* 88, p 605-609 (2000).

[66] T. Q. Nguyen, R. C. Kwong, M. E. Thompson, and B. J. Schwartz, "Improving the performance of conjugated polymer-based devices by control of interchain interactions and polymer film morphology," *Applied Physics Letters* 76, p 2454-56 (2000).

[67] T. Q. Nguyen, I. B. Martini, J. Liu, and B. J. Schwartz, "Controlling Interchain Interactions in Conjugated Polymers: The Effects of Chain Morphology on Exciton-Exciton Annihilation and Aggregation in MEH-PPV Films," *Journal of Physical ChemistryB* 104, p 237-255 (2000).

[68] R. F. Service, "Printable Electronics That Stick Around," *Science* 304, p 675-678 (2004).

[69] E. I. Haskal, M. Bu¨ chel, P. C. Duineveld, A. Sempel and P. van de Weijer, "Passive-Matrix Polymer Light-Emitting Displays," *MRS Bulletin* 27, p 864-868 (2002).

[70] R. K. Holman, S. A. Uhland, M. J. Cima and E. Sachs, "Surface Adsorption Effects in the Inkjet Printing of an Aqueous Polymer Solution on a Porous Oxide Ceramic Substrate," *Journal of Colloid and Interface Science* 247, p 266-274 (2002).

[71] P. Calvert, "Inkjet Printing for Materials and Devices," *Chem. Mater.* 13, p 3299 (2001).

[72] L. T. Creagh and M. Mc Donald, "Design and Performance of Inkjet Print Heads for Non-Graphic-Arts Applications," *MRS Bulletin* 28, p 807 (2003).

[73] V. G. Shah and D. B. Wallace, "Low-cost Solar Cell Fabrication by Drop-on-Demand Ink-jet Printing," *Proc. IMAPS*, 37th Annual International Symposium on Microelectronics Long Beach, CA, November 14-18, (2004).

[74] http://www.microdrop.de/

[75] Operation Manual, Microdrop-AutoDrop Sytem Version 5.50

[76] G. Decher, "Fuzzy Nanoassemblies: Toward Layered Polymeric Multicomposites," *Science* 277, p 1232-1237 (1997).

[77] Y. Lvov, G. Decher, H. Möhwald, "Assembly, structural characterization and thermal behavior of layer-by-layer deposited ultrathin films of polyvinylsulfonate and polyallylamine," *Langmuir* 9, p 481-486 (1993).

[78] R.K. Iler, "Multilayers of colloidal particles," *Journal of Colloid and Interface Science* 21, p 569-594 (1966).

[79] K. Ariga, Y. Lvov, T. Kunitake, "Assembling alternate dye-polyion molecular films by electrostatic layer-by-layer adsorption," *Journal of American Chemical Society* 119, p 2224-2231 (1997).

[80] Y. Lvov, K. Ariga, I. Ichinose, T. Kunitake, "Alternate assembly of ordered multilayers of SiO_2 and other nanoparticles," *Langmuir* 13, p 6195-6203 (1997).

[81] F. Hua, J. Shi, Y. Lvov, T. Cui, "Fabrication and Characterization of Capacitor Based on Layer-by-Layer Self-Assembled Thin Films," *Nanotechnology* 14, p 453-457 (2003).

[82] M. Onoda, K. Yoshino, "Heterostructure electroluminescent diodes prepared from selfassembled multilayers of poly(p-phenylene vinylene) and sulfonate polyaniline," *Japanese Journal of Applied Physics* 34, p L260-263 (1995).

[83] T. Cassagneau, J. Fendler, T. Mallouk, "Optical and electrical characterizations of ultrathin films selfassembled from 11-Aminoundecanoic acid capped TiO_2 nanoparticles and polyallylamine hydrochloride," *Langmuir* 16, p 241-246 (2002).

[84] T. Cui, F. Hua, Y. Lvov, "Field Effect Transistor Fabricated via Electrostatic Layer-by-Layer Nanoassembly," *IEEE Transactions on Electron Devices* 51, p 503-507 (2004).

[85] J. H. Cheung, A. C. Fou and M. F. Rubner, "Molecular self-assembly of conducting polymers," *Thin Solid Films* 244, no1-2 Part 3, p 985–989 (1993).

[86] A.C. Fou, O. Onitsuka, M. Ferreira, M.F. Rubner and B.R. Hsieh, "Fabrication and properties of lightemitting diodes based on self-assembled multilayers of

poly(phenylene vinylene)," *Journal of Applied Physics* 79, no10, p 7501-7509 (1996).

[87] M. Ferreira, J. H. Cheung and M. F. Rubner, "Molecular self-assembly of conjugated polyions: a new process for fabricating multilayer thin film heterostructures," *Thin Solid Films* 244, p 806–809 (1994).

[88] M. Ferreira and M. F. Rubner, "Molecular-level processing of conjugated polymers. 1. Layer-by-layer manipulation of conjugated polyions," *Macromolecules* 28, no21, p 7107–7114 (1995).

[89] A. C. Fou and M. F. Rubner, "Molecular-level processing of conjugated polymers-Layer-by-layer manipulation of in-situ polymerized p-type doped conducting polymers," *Macromolecules* 28, no. 21, p 7115–7120 (1995).

[90] W. B. Stockton and M. F. Rubner, "Molecular-Level Processing of Conjugated Polymers-Layer-by-Layer Manipulation of Polyaniline via Hydrogen-Bonding Interactions," *Macromolecules* 30, p 2717–2725 (1997).

[91] H. Hong, D. Davidov, Y. Avany, H. Chayet, E.Z. Faraggi and R. Neumann, "Electroluminescence, photoluminescence and X-ray reflectivity studies of self-assembled ultra-thin films," *Advanced Materials* 7, no.10, p 846–849 (1995).

[92] J. H. Burroughes, C. A. Jones, and R. H. Friend, "New semiconductor device physics in polymer diodes and transistors," *Nature* 335, no. 6186, p 137–141 (1988).

[93] M. K.Ram, M. Adami, P .Faraci, C. Nicolini, "Physical Insight In The In-Situ Self Assembled Films of Polypyrrole," *Polymer* 41, p 7499-7509 (2000).

[94] Dean M. Delongchamp, M. Kastantin, P. T. Hammond, "High-Contrast Electrochromism from Layer-By- Layer Polymer Films," *Advanced Materials* 15, p 1575-86 (2003).

[95] J. Stepp, J. B. Schlenoff, "Electrochromism and electrocatalysis in viologen polyelectrolyte multilayers," *Journal of Electrochemical Society* 144, p L155-L157 (1997).

[96] D. DeLongchamp, P. T.Hammond, "Layer-by-Layer Assembly of PEDOT/Polyaniline Electrochromic Devices," *Advanced Materials* 13, p 1455-1459 (2001).

[97] C. A. Cutler, M. Bouguettaya, J. R. Reynolds, "PEDOT Polyelectrolyte Based Electrochromic Films via Electrostatic Adsorption," *Advanced Materials.* 14, p 684-688 (2002).

[98] G. Zotti, S. Zecchin, A. Berlin, G. Schiavon, G. Giro, "Multiple Adsorption of Polythiophene Layers on ITO/Glass Electrodes and Their Optical, Electrochemical, and Conductive Properties," *Chemistry of Materials* 13, p 43-52 (2001).

[99] B. L. Groenendaal, F. Jonas, D. Freitag, H. Pielartzik, J. R.Reynolds, "Poly(3,4-ethylenedioxythiophene) and Its Derivatives: Past, Present, and Future," *Advanced Materials* 12, p 481- 494 (2000).

[100] G. Xu, Z. Bao, and J.T. Groves, "Langmuir-Blodgett Films of Regioregular poly (3-hexylthiophene) as field-effect transistors," *Langmuir*, 16, p 1834-1841 (2000).

[101] S. A. Carter, M. Angelopoulos, S. Karg, P. J. Brock, J. C. Scott, "Polymeric anodes for improved polymer light-emitting diode performance," *Applied Physics Letters* 70, p 2067-2069 (1997).

[102] T. Cui, G. Liang, and K. Varahramyan. "An Organic Poly(3,4-Ethylenedioxythiophene) Field-Effect Transistor Fabricated by Spin Coating and Reactive Ion Etching," *IEEE Transactions on Electron Devices* 50, no.5, p 1419-1422 (2003).

[103] K. H. Peter, K. Ji-Seon, H. Jeremy, F. Y. Sam, M. Thomas M, H. Richard, "Molecular scale Interface Engineering for Polymer Light- Emitting Diodes," *Nature* 404, p 481-484 (2000).

[104] D. Orata and D.A. Buttry, "Determination of Ion Populations and Solvent Content as Functions of Redox State and pH in Polyaniline," *J. Amer. Chem. Soc* 109, no. 12, p 3574 (1987).

[105] The University of Chicago Chronicle, "Coffee stains," 17, no. 3, (Oct. 23, 1997).

[106] R. D. Deegan, O. Bakajin, T. F. Dupont, G. Huber, S. R. Nagel, and T. A. Witten, "Capillary flow as the cause of ring stains from dried liquid drops" *Nature* 389, p 827-829 (1997).

[107] R. D. Deegan, "Pattern formation in drying drops," *Physical Review E* 61, p 475-485 (2000).

[108] R. D. Deegan, O. Bakajin, T. F. Dupont, G. Huber, S. R. Nagel, and T. A. Witten, "Contact line deposits in an evaporating drop" *Physical Review E* 62, p 756-765 (2000).

[109] M. Toivakka "Numerical Investigation of Droplet Impact Spreading in Spray Coating of Paper," *Spring Advanced Coating Fundamentals Symposium* 2003.

[110] P.C. Duineveld, M. M. de Kok, M. Buechel, A. H. Sempel, K.A.H. Mutsaers, P. Weijer, I.G.J. Camps, E.I. Haskai, "Ink-Jet Printing of Polymer Light-Emitting Devices," *Proceedings of SPIE*, 4464, p 59-67 (2002).

[111] P. Chandrasekhar, *Conducting Polymers, Fundamentals and Applications*. Kluwer Academic Publishers, 1999.

[112] C. W. Tang, S. A. VanSlyke, "Organic electroluminescent diodes," *Applied Physics Letters* 51, p 913-915 (1987).

[113] V. Bulovic, P. E. Burrows, S. R. Forrest, "Polymeric and Molecular Organic Light Emitting Devices" *Semiconductors and Semimetals* 64, p 255 (2000).

[114] J. Kido,Y. Iizumi, "Fabrication of highly efficient organic electroluminescent devices," *Applied Physics Letters* 73, p 2721-2723 (1998).

[115] A. J. Campbell, D. D. C. Bradley, E. Werner, W. Brutting, "Deep level transient spectroscopy (DLTS) of a poly(p-phenylene vinylene) Schottky diode," *Synthetic Metals*111, p 273-276 (2000).

[116] H. Tseng, K. Peng, S. Chen, "Molecular oxygen and moisture as traps in poly[2-methoxy-5-(2-ethylhexyloxy)-1,4-phenylene vinylene]: locations and detrapping by chain relaxation," *Applied Physics Letters* 82, p 4086-4088 (2003).

[117] J. C. Scott, J. H. Kaufman, P. J. Brock, R. DiPietro, J. Salem, J. A. Goitia, "Impurity-controlled dopant activation: Hydrogen-determined site selection of boron in silicon carbide," *Journal of Applied Physics*79, p 2746-2748 (1995).

[118] B. G. Streetman and S. Banerjee, "Solid State Electronic Devices", 5th edition, Pearson Education, 2002.